Integrated Terahertz Quantum Cascade Laser System for Space Research

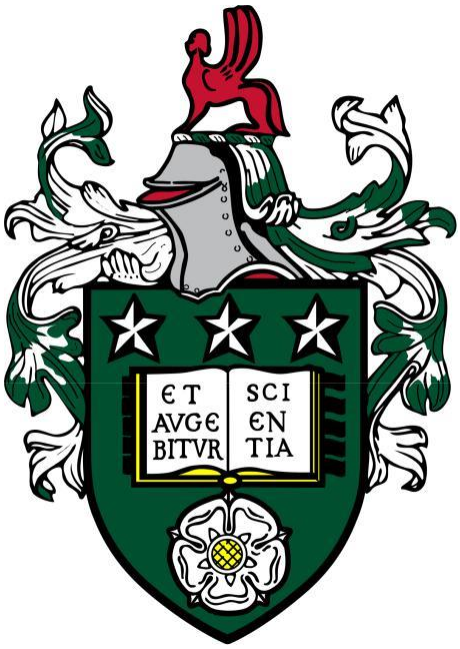

Sanchit Subhash Kondawar

Submitted in accordance with the requirements for the degree of Doctor of Philosophy

University of Leeds
School of Electronic and Electrical Engineering
November 2023

Declaration

The candidate confirms that the work submitted is his own and that appropriate credit has been given where reference has been made to the work of others. This copy has been supplied on the understanding that it is copyright material and that no quotation from this work may be published without proper acknowledgement. The University of Leeds and Sanchit Subhash Kondawar.

Some figures presented in the thesis do not include THz power measurement calculations and are thus plotted in normalized arbitrary units. The quantum cascade lasers described in Chapters 3, 4 and 5 were designed and fabricated by Mohammed Salih, Yingjun Han, and Iman Kundu with the valuable contributions of Lianhe Li in the Nanotechnology cleanroom laboratory, at the University of Leeds.

The implementation of the power-locked quantum cascade laser described in section 3.3.4 and section 3.4 was a collaboration between myself and Nicholas North. The work presented in section 3.3.4 was carried out under the supervision of Yinjun Han.

The integration of the quantum-cascade lasers into the metallic waveguide blocks was carried out by Rutherford Appleton Laboratory (RAL) Space Department. The investigation of waveguide integrated 2 THz QCL discussed in section 4.5 was a collaboration between myself and Mohammed Salih, under the supervision of Alexander Valavanis. Also, waveguide integrated 4.7 THz QCL in section 4.4 was collaboration with Eleanor Nuttall.

The TeraFET detector investigation presented in section 5.3 was an international collaboration with Goethe University Frankfurt. The detector designing and manufacturing were carried out by the Frankfurt team, and the characterisation of the detector was done by myself and Anastasiya Kyrsl at Leeds. This work was done with

guidance from Michael Horbury. Additionally, the work presented in section 5.4 was a joint effort involving both myself and Nicholas North.

Peace cannot be kept by force; it can only be achieved by understanding.

— Albert Einstein

To the three lifelines that anchor my existence –
Papa, Mummy, and Rugvedi, you are my everything. I am truly grateful.

And,

To my late brother –
Sonu Dada, your absence is a daily void. Thank you for watching over me.

Acknowledgment

First and foremost, I extend my heartfelt gratitude to my supervisor, Dr. Alexander Valavanis, for his support and guidance throughout my doctoral studies. Your expertise, mentorship and valuable insights have played a role in shaping the direction and enhancing the quality of my research. I would also like to extend my gratitude to Dr. Paul Dean, my co-supervisor for his support during my PhD.

I would like to acknowledge the School of Electronics and Electrical Engineering, University of Leeds for their support throughout this endeavour. Additionally, I am grateful for the funding body supported by UK Research and Innovation (Future Leaders Fellowship MR/S016929/1), European Space Agency (General Support Technology Programme contract 4000114487/15/NL/AF), UK Space Agency's National Space Technology Programme (contract NSTP3- FT2-002), Centre for Earth Observation Instrumentation (Fast Track contract RP10G0435A03 for 3.5, 4.7 THz QCL & contract RP10G0435A504 for 2.0 THz QCL), Engineering and Physical Sciences Research Council (Programme grant EP/P021859/1), and special thanks to the project collaborators — STFC Rutherford Appleton Laboratory and Goethe University Frankfurt.

A heartfelt appreciation to Dr. Dragan Indjin for introducing me to the fascinating world of terahertz research. I am truly grateful to you and all the teachers who have crossed my path, guiding and enabling me to fulfil my dream of obtaining a PhD. I am particularly grateful to Prof. Edmund H. Linfield, Prof. A. Giles Davies, Prof. John E. Cunningham and Dr. Joshua Freeman for their insightful discussions and significant contributions to the development of this project.

Big thanks to Dr. Mohammed Salih, Dr. Yingjun Han, Dr Michael Horbury and others who offered invaluable assistance and support when I needed it the most. To all my colleagues — Nik, Elly, JP, Nic, Imran, and Dan, thank you for your collaboration

and strong team spirit. I also extend my sincere gratitude to all the members of the Nanotechnology Cleanroom Lab and Terahertz Photonic Lab for their valuable training and support, with special thanks to Emma Wright, Sue Hobson and Clair Atkinson for their tremendous administrative support.

I am profoundly grateful for the encouragement from my friends throughout this PhD journey. With special thanks to Dr. Joyjit and my Vishay group—your guidance has been a key part of this achievement, and I truly appreciate it.

Last, but not the least, I would like to express my gratitude and appreciation to my parents, my life partner, my late big brother and my family.

Papa, your wisdom has been my guiding light. Thank you for being my role model, my confidence, and my source of strength. Mummy, your boundless love and nurturing spirit have shaped me into the person I am today. Thank you for being the foundation upon which my dreams are built. Rugvedi, your presence in my life has been a gift beyond measure. Your love, support, kindness and sacrifices have been instrumental in shaping my journey towards obtaining my doctorate. In this dynamic and ever-changing world, I thank you for always being my constant. Sonu Dada, your impact as big brother will always be cherished. Thank you for being with me, even in your absence.

This achievement is dedicated wholeheartedly to all of you.

Abstract

The terahertz frequency range, which falls between microwaves and infrared waves in the electromagnetic spectrum offers advantages in various scientific fields. It enables the analysis of crystal structures, exploration of quantum states in semiconductors and detection of gases based on their spectral signatures. This region overcomes the limitations of infrared and UV/visible techniques when it comes to identifying gases found in Earth's upper atmosphere or star-forming nebulas.

However using THz sensors for satellite applications has challenges due to their size, complex design and high power requirements. Nevertheless, a recent breakthrough involving the use of THz quantum cascade lasers (QCLs) has provided a solution to these challenges. These tunable lasers are compact yet powerful enough, within the THz frequency range making them perfectly suited for satellite applications.

The main objective of this project is to make advancements in the development of the "front-end" component of an integrated THz receiver that will be used in the KEYSTONE satellite mission. This be was approached using waveguide integrated THz QCLs as a local oscillator. This project involved thorough research on fabricating and characterizing QCL devices that are essential for the KEYSTONE satellite receiver. Additionally, the project also focuses on integrating these devices into waveguides, and stabilisation of their output power.

The main findings of this study involve the implementation of THz QCL power locking by utilizing a photonic integrated circuit (PIC). This PIC is formed by combining a racetrack resonator (RTR), with a QCL ridge waveguide. The output power of THz QCL can be affected by temperature changes, mechanical vibrations and atmospheric absorption. Therefore it is essential to stabilize the output power in space research applications where stability plays a vital role in determining the instrument's sensitivity. Moreover, this project showcases a method for manufacturing

rectangular terahertz waveguides with integrated diagonal feedhorns through precision micromachining. Lastly, the study focuses on exploring the capabilities of fast THz detectors for scanning and THz gas spectroscopy applications, in atmospheric chemistry and satellite communication systems.

Future work will focus on advancement towards faster power-locking techniques. Researchers may also look at the possibility of high bandwidth power and frequency locking. Improved thermal and optical integration will further enhance this dual-lock approach, which has potential applications in the medical, communications, and space exploration industries. Additionally, by using QCL grating methods, it is possible to improve the accuracy of QCL frequency to accurately target certain gas emission lines. This study could also extend its scope to include terahertz gas spectroscopy for atmospheric chemistry and the dynamic processes causing changes in the Earth's climate. This development could involve determining branching ratios for atmospheric reactions involving volatile organic compounds, and an exploration of their environmental consequences.

Publications

The work in this thesis has been presented in the following journal paper and conference proceedings:

Journal papers:

- **S. S. Kondawar**, N. North, Y. Han, D. Pardo, N. Brewster, M. D. Horbury, M. Salih, L. H. Li, P. Dean, J. R. Freeman, B. N. Ellison, M. Rosamond, I. Kundu, and A. Valavanis. 'Power-locked terahertz quantum cascade laser with an integrated power controller', (paper in preparation - aim to publish in Optics Express)

- E. Nuttall, Y. Han, D. Pardo, **S.S. Kondawar**, N. Brewster, M. Salih, L.H. Li, M.D. Horbury, A.G. Davies, E.H. Linfield, H. Wang, P. Dean, B.N. Ellison and A. Valavanis. 'Waveguide integration of a >4.7-THz quantum-cascade laser,' in Electronic Letters, vol.59, no.2, p.12703, 2023, doi.org/10.1049/ell2.12703

- M. Salih, **S. S. Kondawar**, N. Brewster, L. H. Li, E. H. Linfield, H. Wang, P. G. Huggard, J. R. Freeman, D. Gerber, and A. Valavanis. 'Integration of 2-THz Local Oscillator of Quantum Cascade Laser within an IEEE Metallic Waveguide', (paper in preparation - aim to publish in IEEE)

- M. D. Horbury, N. North, J. Holstein, L. Li, **S. S. Kondawar**, J. R. Freeman, A. Lisauskas, H. Roskos and A. Valavanis. '3.5 THz QCL-Enabled Gas Spectroscopy with TeraFET Detector', (paper in preparation - aim to publish in Nature Communications)

Conference Proceedings:

- **S. S. Kondawar**, N. K. North, Y. Han, D. Pardo, N. Brewster, M. Salih, M. D. Horbury, L. H. Li, P. Dean, B. N. Ellison, I. Kundu, and A. Valavanis. 'Amplitude Stabilization of a THz Quantum-Cascade Laser Using a Photonic Integrated Circuit', in 48th International Conference on Infrared, Millimeter and Terahertz Waves (IRMMW-THz), 2023, doi: 10.1109/IRMMW-THz57677.2023.10299009

- E. Nuttall, Y.J. Han, D. Pardo, M.D. Horbury, **S.S. Kondawar**, N.K. North, I. Kundu, O. Auriacombe, T. Rawlings, N. Brewster, M. Oldfield, M. Salih, L.H. Li, vi Chapter 0 E. Zafar, A.G. Davies, E.H. Linfield, E. Saenz, H. Wang, B.N. Ellison, A. Valavanis, 'Waveguide integrated terahertz quantum-cascade laser systems,' in 46th International Conference on Infrared, Millimeter and Terahertz Waves (IRMMW-THz), 2021, doi**:** 10.1109/IRMMW-THz50926.2021.9567247

- M. Salih, **S. S. Kondawar**, N. Brewster, L. H. Li, E. H. Linfield, H. Wang, P. G. Huggard, J. R. Freeman, D. Gerber, and A. Valavanis. 'Integration of a 2.1-THz Quantum Cascade Laser within an IEEE WM-130 Rectangular Metallic Waveguide', in 48th International Conference on Infrared, Millimeter and Terahertz Waves (IRMMW-THz), 2023, doi: 10.1109/IRMMW-THz57677.2023.10299333

List of Figures

List of Tables

List of Abbreviations

AR	Active Region
CSL	Chirped Superlattice
CW	Continuous-Wave
CEOI	Centre for Earth Observation Instrumentation
DAC	Digital to Analog Converter
DM	Double Metal
EAM	Electroabsorption Modulator
ESA	European Space Agency
FDS	Frequency Domain Spectroscopy
FEL	Free Electron Laser
FFT	Fast Fourier Transform
FIB	Focused Ion Beam
FPGA	Field Programmable Gate Array
FSR	Free Spectral Range
FTIR	Fourier Transform Infrared
GREAT	German REceiver for Astronomy at Terahertz frequencies
HEB	Hot Electron Bolometer
HF	Hydrofluoric acid
IF	Intermediate Frequency
LI	Light-Current
LIV	Light-Current-Voltage
LNA	Low Noise Amplifier
LO	Local Oscillator
MBE	Molecular Beam Epitaxy
MLT	Mesosphere Lower Thermosphere
MOSFET	Metal-Oxide-Semiconductor Field-Effect Transistor

MZI	Mach-Zehnder Interferometer
NASA	National Aeronautics and Space Administration
NEP	Noise Equivalent Power
NIR	Near Infrared
QCL	Quantum-Cascade Laser
QW	Quantum Well
PI	Proportional-Integral
PID	Proportional-Integral-Derivative
RAL	Rutherford Appleton Laboratory
RF	Radio Frequency
RP	Resonant Phonon
RTD	Resonant Tunnelling Diode
RTR	Racetrack Resonator
SI-SP	Semi-Insulating Surface Plasmon
SMA	Subminiature-A
SNR	Signal to Noise Ratio
SOFIA	Stratospheric Observatory For Infrared Astronomy
SRR	Split Ring Resonator
TDS	Time Domain Spectroscopy
TeraFET	Terahertz Field Effect Transistor
THz	Terahertz
UKSA	United Kingdom Space Agency

Contents

Chapter 1
Introduction to terahertz sensing

1.1 Background

In the electromagnetic spectrum, the frequency range between 0.3 – 10 THz is known as the terahertz frequency region, shown in Figure 1.1. This region has a wavelength from 1 – 0.1 mm and is positioned uniquely between two well-known regions; microwave and infrared bands [1]. Unlike these bands, the terahertz region, also known as the far-infrared region, is less exploited, as it is difficult for the optical device to detect or generate frequencies at that range, and thus this region is referred as the "Terahertz Gap" [2], [3].

However, THz sensing provides unique opportunities as many materials have spectral signatures in the THz range [4], [5].

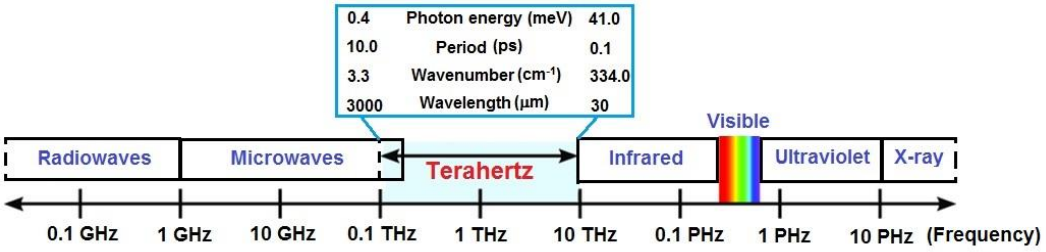

Figure 1.1: Highlighting the position of Terahertz region in electromagnetic Spectrum

THz radiation typically interacts with intermolecular vibrational modes and hence provides information on structural dynamics of crystalline solids [6]. Having a large bandwidth, THz radiation can be used in high speed wireless communication for which THz waves are the free space carrier of data [7], [8]. THz region is also applicable in different fields having some notable properties. Due to its low photon energy, THz

radiation is non-ionizing and thus through non - metallic materials (opaque) such as papers, clothes, ceramics and plastics. This can be useful in security application like airport vigilance to detect weaponries and explosive materials [9], [10]. Moreover, THz radiation can penetrate few millimetres of the biological tissue, although it gets absorbed by the water molecules, this property make THz radiation a harmless technology compared to X-ray and can be used in biomedical imaging applications [11], such as pharmaceutical testing [11], genetic sequencing [12], ex-vivo and in-vivo of basal cell carcinoma [12],[13], human breast tumour [14], and dental caries [15].

In space application, astronomers are very keen to explore the THz frequency region, as $>$ 50 % of the spectral intensity in the galaxy lies in the THz radiation [16], [17]. Numerous gas molecules exhibits strong spectral signatures in the THz region [18]. For example, OH radicals and atomic oxygen [O] are key species in upper atmospheric chemistry with spectral line at 3.5 THz and 4.7 THz respectively.

1.2 Terahertz sources

The evolution of THz sources started in 1975 when the first photoconductive antenna was manufactured based on THz technology [19]. Further modifications were made in THz devices by varying the doping impurities concentration in a semiconductor material.

Various naturally occurring THz sources are found, including solar, and black-body radiation. However, these sources are broadband, have low power, and are incoherent, which can make it difficult to isolate and study specific molecular spectral lines. As a result, the development of THz sources is important for research and industrial applications. The power from semiconductor electronic devices falls dramatically when the frequency is raised above a few hundred gigahertz, primarily due to the requirement for extremely short carrier transit times in the active region (AR). Hence these cannot operate at THz frequencies [2], [3]. Frequency up-conversion from the gigahertz to terahertz results in a significant roll-off in output power [2], [3]. For instance, the operation of resonant tunnelling diodes (RTDs) at room temperature works around 1.46 THz but significantly drops the output power to 0.36 μW [20], and

planar Gunn diodes give output power of 28 μW when operating at around 300 GHz [21]. Similarly, terahertz frequency emission from optical devices is challenging because of the lack of semiconductor materials with a sufficiently narrow band gap. In the early 1980s, PbSnTeSe-based semiconductor heterojunction lasers were demonstrated to lase up to 6.5 THz [22], but these are toxic, and challenging materials to process.

THz radiation generation has also been investigated using alternative optical methods. For example, photomixers [23], [24], photoconductive antennas [25],[26], THz parametric oscillators [27], and optical rectifiers [28], [29] have all been used to produce THz radiation. There are some high power sources, such as free electron lasers (FEL) [30] and optically pumped gas laser [31], [32] which operate at terahertz frequency. However, these lasers are often expensive, bulky, and have high power consumption or long term stability issues [33]. Additionally, p-doped germanium lasers [34] and THz quantum cascade lasers (QCLs) [35] are also categorised as THz sources, as shown in Figure 1.2 [36]. However, despite their compact size, they still need liquid helium temperatures to operate in THz frequency [37].

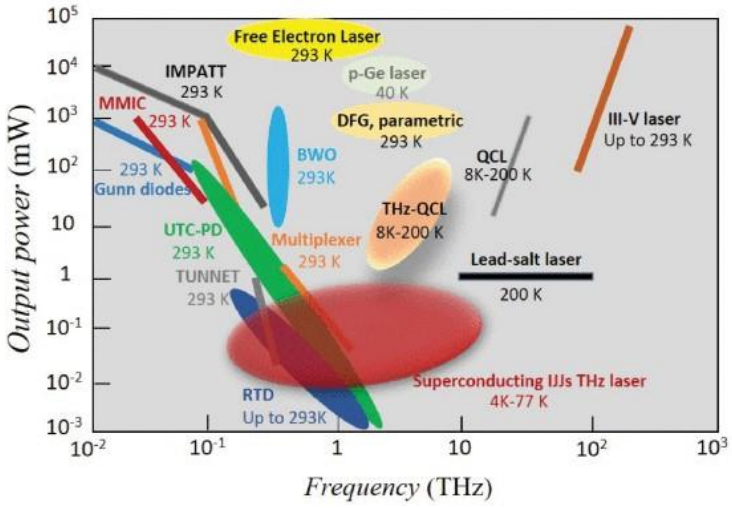

Figure 1.2: Typical output powers and emission frequency ranges of a variety of terahertz radiation sources. (Adapted from [36])

As such, there are numerous approaches to develop both broadband and narrowband THz sources [38], as outlined in the following section.

1.2.1 Broadband THz sources

Broadband sources offer wide frequency coverage, but are unsuitable for high spectral resolution measurement or coherent sensing. The majority of the broadband pulse terahertz sources use ultrashort laser pulses to excite different materials. Various techniques have been demonstrated to generate THz radiation, including photocarrier acceleration in photoconductive antennas, plasma oscillations, and electronic non-linear transmission lines; as stated earlier, these terahertz sources generate very low output power in the range of nano- to microwatt. However, a femtosecond optical source generates an average output power of up to 1W [39]. Two popular methods for producing broadband pulsed THz beams are photoconduction and optical rectification. In photoconduction, High-speed photoconductors are used as transient current sources for radiating antennas. High-resistivity GaAs, InP, and radiation-damaged silicon wafers are typical examples of photoconductors. The building of an antenna and biasing of the photoconductive gap is done by using metallic electrodes. Ultrafast laser pulses are used for photoconductive antenna to generate a THz beam (where photon energy is larger than the bandgap of the material). A very fast photocurrent is produced due to the carrier acceleration and deceleration in the semiconductor material. The high mobility and short recombination lifetime in the device yields broadband THz emission [37], [38].

An alternate technique for producing pulsed THz waves is optical rectification; based inversely on the electro-optic effect. Femtosecond laser pulses are necessary, but unlike photoconducting components where the optical beam acts as a trigger, optical rectification produces THz radiation energy directly from the exciting laser pulse. The nonlinear coefficient of the material and the phase-matching circumstances significantly impact the conversion efficiency in optical rectification. However, the output power produced by this method is less compared to photoconduction method, but has a higher bandwidth, up to 50 THz. These broadband THz sources are used for chemical detection and in medical imaging [37], [38].

1.2.2 Narrowband THz sources

Significant growth in the development of the narrowband THz sources has been carried out over the past few years, as narrowband THz sources are vital for high-resolution spectroscopy and used for many possible applications in telecommunication for inter-satellite links.

Numerous techniques, including a chain of planar GaAs Schottky-diode multipliers, free-electron lasers, semiconductor lasers, are used in narrowband THz sources. For semiconductor lasers population inversion must be achieved i.e. a large number of electron in an upper energy state than in lower state [37], [38]. The gaps between the energy states define the wavelength of the photon emission [40].

Chapter 2 discusses Quantum Cascade Lasers (QCLs), which were first demonstrated in 1994 based on multiple quantum wells structure using molecular beam epitaxy [41]. This work focuses on application of THz QCLs in atmospheric systems.

1.3 THz Spectroscopy systems

THz spectroscopy is a highly effective technique used in a wide range of fields for studying the properties of matter. THz spectroscopy systems are used for the detection of the physical, optical or electronic structure, its alignment or the phonon vibration of any sample when passed through the THz radiation. The application of THz spectroscopy systems is widespread, with potential uses in imaging, security, medical sciences, and astronomy and earth observation. The THz spectroscopy system is categorised into two types, time domain spectroscopy (TDS) and frequency domain spectroscopy (FDS) [37], [38].

1.3.1 THz time-domain spectroscopy (TDS)

THz Time domain spectroscopy operates by using short pulses of broadband THz radiation [37]. Femtosecond pulses are generated by an ultrafast laser as illustrated in Figure 1.3, This laser beam is divided into two halves using a beam splitter, one half of the laser beam pumps into the THz emitter, where THz pulses are generated. These THz pulses are then focused by parabolic mirrors and then the THz pulses are passed through the sample. A THz detector is used to collimate the THz pulses coming from the sample. The second half of the laser beam is passed to the THz detector. Both the THz and pump beams merge together in the THz detector where THz electric field is measured instantaneously in the time domain. A Fourier transform of the THz field is then used to obtain the spectrum. TDS has the property of resisting noise which makes the measurement of THz radiation more precise for different samples, though, it needs some signal conditioning to improve the measurement [37].

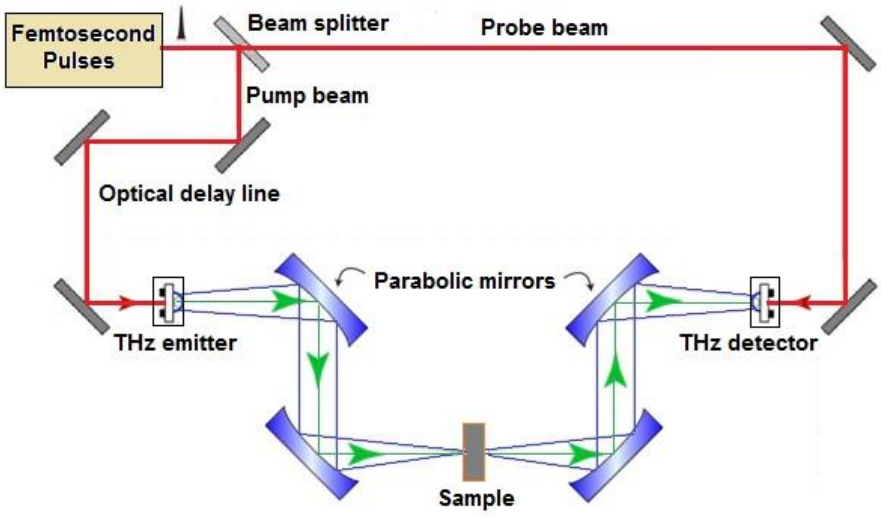

Figure 1.3: THz TDS pump probe system (reproduced from [37])

1.3.2 THz frequency domain spectroscopy (FDS)

In astronomy research, THz-FDS is commonly used for analysing the thermal emission lines of molecules. Heterodyne spectroscopy is used to achieve high spectral resolution in the THz frequency band. This method involves the generation of an

intermediate frequency (IF), which is obtained by passing two different frequencies through a non-linear element. The intermediate frequency range is generally in the GHz. The electronic components in the super heterodyne receiver like filters, amplifiers, signal conditioner work on the intermediate frequency [42].

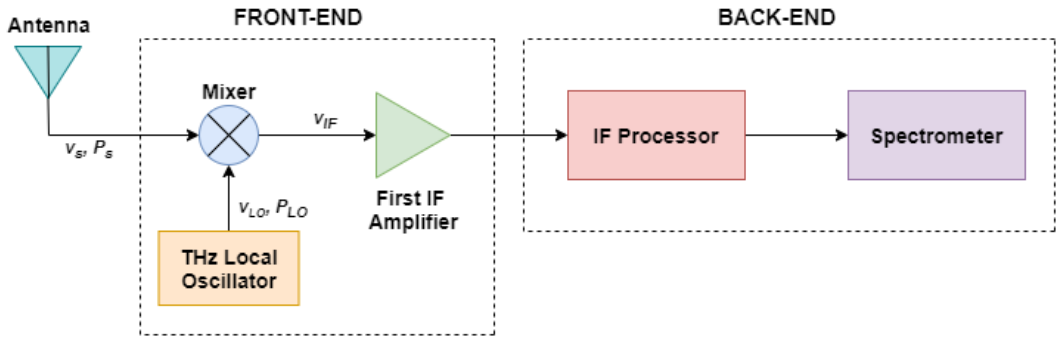

Figure 1.4: THz heterodyne receiver (reproduced from [43])

Figure 1.4 illustrates that the design of a THz heterodyne receiver is composed of two subsystems, namely the front-end and back-end subsystems. The mixer in the front-end subsystem receives the THz signal as its input from the antenna, with a frequency $v(s)$ and power $p(s)$. The intermediate frequency is obtained at the output of the mixer, which is the subtraction of the antenna signal and local oscillator signal ($v_{IF} = v_S - v_{LO}$) [42]. This has the advantage of high spectral resolution, and can be used for analysis of narrow spectral features.

1.4 Terahertz Applications

Sensing and communications are the two main divisions of THz applications. THz technologies offer potential sensing capabilities for several research domains, including biology, pharmacy, medical science, industrial non-destructive assessment, material science, environment monitoring, security, astronomy, and fundamental science. Similarly, THz technology benefits in various information and communications technology applications; including satellite communication, high-speed data processing, and wireless communication [44], [38].

1.4.1 Biological, Medical and Pharmaceutical Sciences

A significant numbers of studies on cancer diagnosis using THz spectroscopy and imaging has been conducted. THz waves are susceptible to absorption by polar molecules like water, making it possible to detect anomalous reflections from cancer tissue because it has a different amount of hydration than normal tissue. The reflection of THz-TDS is used to detect skin cancer, with a penetration depth of approximately a millimetre and resolutions of around 350 μm and 40 μm. Its non-ionizing nature also allows safe in vivo imaging. In addition, ice has a significantly higher THz transmittance than water; cancer cells can also be spotted in frozen tissue [37].

1.4.2 Semiconductor and Other Industrial Applications

Terahertz technology has the potential to revolutionize various materials, such as examining silicon solar cells, nanocomposites, polymer films, and dielectric films, leading to new industrial applications. Terahertz TDS can assess several semiconductor wafer characteristics (shown in Figure 1.5), including mobility, conductivity, carrier density, and plasma oscillations [45], [46].

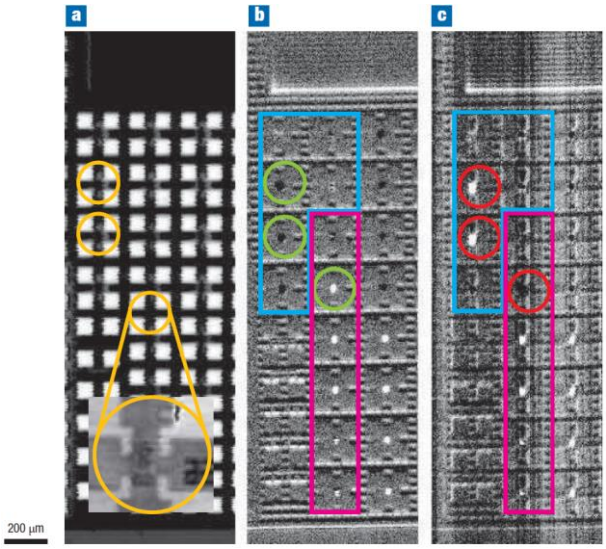

Figure 1.5: (a) MOSFETs inspection demonstrated. Examination of three intentionally damaged circles, which were then contrasted with an undamaged MOSFET (b), as depicted in a THz emission image (c). The difference observed within the image highlight the defects present in these MOSFETs. (Adapted from [37])

Terahertz imaging has been utilized to inspect the foam insulation on the space shuttle, which is considered the most effective non-destructive testing technique. This method is useful for inspecting space shuttles as it can detect voids and other heat-insulation panel problems [47].

1.4.3 Security

The THz spectra of explosives and drugs commonly have a distinctive signature, making THz spectroscopy useful for security applications. Through their transmission spectra, these marks allow the identification of several substances. THz radiation also penetrates through dry dielectric packaging and clothing materials. It is feasible to discriminate between harmful substances and explosives in particular [9].

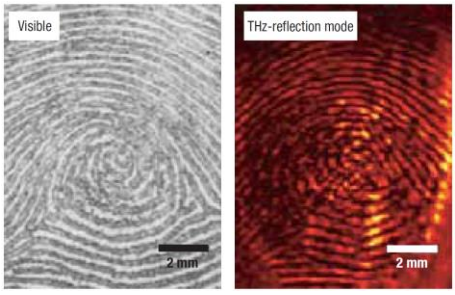

Figure 1.6: Comparison between a visible thumbprint and a real-time THz reflection mode image of the identical thumbprint. (Adapted from [37])

Additionally, terahertz QCLs can offer a real-time THz-imaging tool. An example of fingerprint imaging using a polyethylene wedge is shown in Figure1.6. The print has grooves spaced around 500 μm apart [48].

1.5 Terahertz space missions

Less than 50% light can be observed with infrared, radio, and microwave sensors. The far-infrared, or terahertz region of the spectrum (1-10 THz, 30-300 micron wavelength) covers the majority of the missing light. The invisible gases in the Earth's atmosphere and the gas clouds that exist between stars, all glow

with distinctive THz signatures. Despite this enormous potential, most applications outside of the laboratory need fragile and sophisticated THz sensor systems, which lack the sensitivity needed to investigate reactive gases. Moreover, this lack of technological capabilities limits the possibility of THz devices being deployed in space [49],[50], [51].

Nevertheless, there have been several THz space/atmospheric missions, which are described in the following section.

1.5.1 Aura satellite (EOS-MLS)

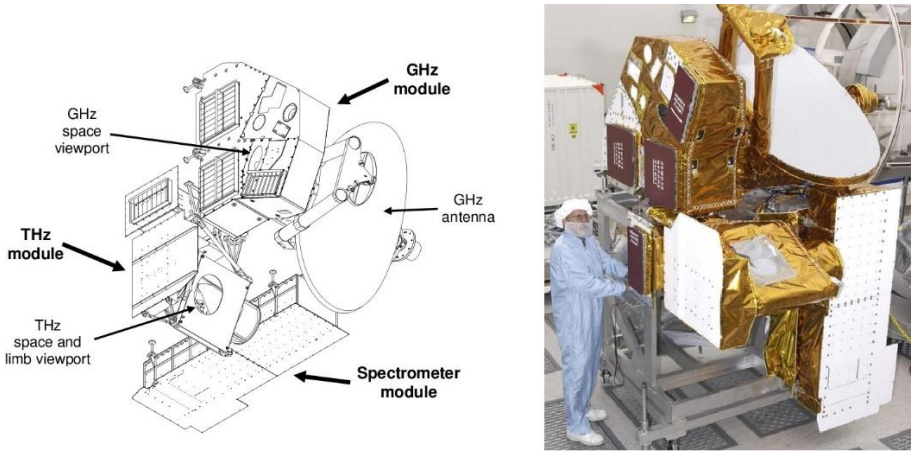

Figure 1.7: Drawing (left) and photograph (right) of Aura satellite (Adapted from [52]).

THz technology is currently crucial for Earth's environmental monitoring. On-board NASA's Aura spacecraft, the Earth Observing System Microwave Limb Sounder (EOS-MLS), was placed into orbit in July 2004. It is the first satellite using MLS to study the upper atmosphere, as shown in Figure 1.7 (right). MLS remotely measures atmospheric parameters by observing thermal emission at millimeter and submillimeter wavelengths.

It has measured temperature, air chemical species (OH, HO_2, H_2O, O_3, HCl, HOCl, BrO, HNO_3, N_2O, CO, HCN, CH_3CN, and volcanic SO_2), clouds, and ice, as shown in Figure 1.8 [52]. Around 118, 190, 240, 640 GHz, and 2.5 THz are the thermal emission frequencies that its heterodyne radiometer monitors. The main goals are to quantify

elements of how the atmospheric composition influences climate, examine aspects of pollution in the upper troposphere and gather information on ozone chemistry to understand global warming better.

The MLS comprises the THz, GHz, and spectrometer modules, as shown in Figure 1.7 (left). The THz module is implemented specifically for measuring the OH radical and O_3 species, in the stratosphere and mesosphere by employing heterodyne detection of thermal emission.

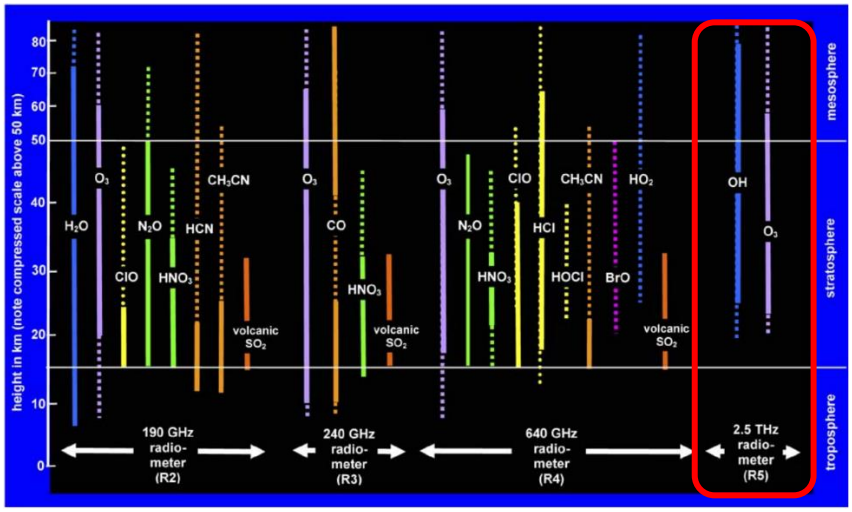

Figure 1.8: Chemical species observed by individual EOS MLS radiometers. The 2.5 THz radiometer observes OH and O3 in the stratosphere region (Adapted from [52]).

The THz module includes essential components such as the THz scan and switching mirror, calibration target, telescope, and 2.5-THz radiometers at both polarizations. It operates by detecting limb emission through heterodyne radiometry. This method involves a methanol gas laser local oscillator (GLLO) and waveguide diode mixers for precise detection and measurement purposes [52], [53]. A drawback of using such THz module is that LO based methanol gas lasers are bulky and prone to leak in space conditions.

1.5.2 Planck satellite

The Planck mission is Europe's first attempt to study the Cosmic Microwave Background (CMB), which is the leftover radiation from the Big Bang about 14 billion years ago, as shown in Figure 1.9 (left).

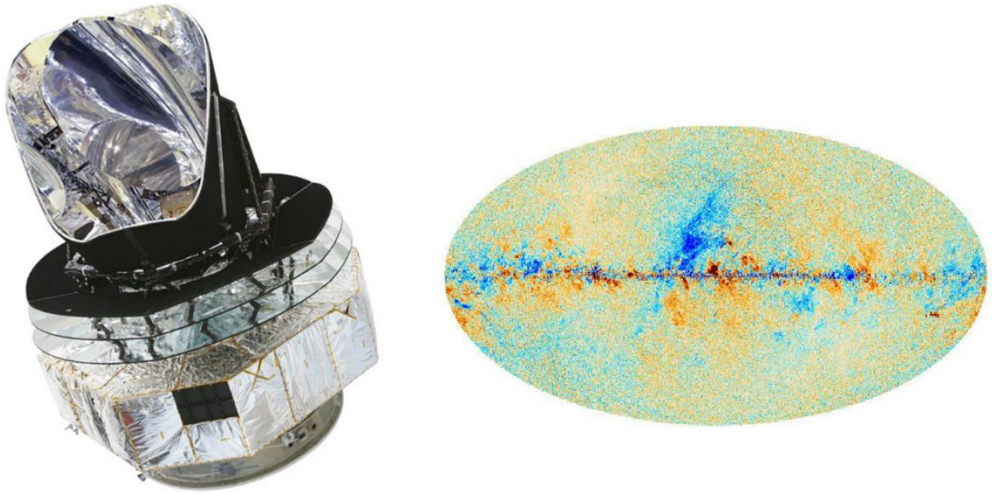

Figure 1.9: (Left) Photograph of Planck satellite (Adapted from [54]). (Right) Planck-HFI map of CMB (Adapted from [55])

The mission uses two specific payloads called the Low-Frequency Instrument (LFI) and the High-Frequency Instrument (HFI). These payloads have sensitive radio receivers that work at cryogenic temperatures. The LFI consists of three frequency bands, which span from 30 to 70 GHz. This range covers both the microwave and infrared portions of the electromagnetic spectrum. The detectors within the LFI utilize high-electron-mobility transistors to capture and process the incoming radiation [54].

On the other hand, the HFI operates at frequencies ranging from 100 to 857 GHz. It comprises 52 bolometric detectors, which were developed by JPL/Caltech. These detectors are optically linked to the telescope via cold optics, which were developed by the School of Physics and Astronomy at Cardiff University [54].

These instruments measure the temperature of the CMB radiation precisely having a sensitivity of 1 Kelvin. With these measurements, the Planck mission creates detailed maps showing variations in the CMB radiation in space, as shown in Figure 1.9 (right). These maps are crucial to get a better understanding of the beginning of the

universe [54]. Bolometric detectors have drawbacks, including their heavy reliance on liquid helium, which restricts their operational lifetime for measurements. Additionally, they have a limited spectral resolution as these detectors are broadband.

1.5.3 Herschel Space Observatory

The Herschel Space Observatory was the biggest infrared space telescope ever sent into space until the James Webb telescope, as shown in Figure 1.10 (left). Herschel specializes in observing the far-infrared and submillimeter parts of the light spectrum (55–671 μm). This unique capability of the Herschel telescope allows it to detect cold objects in outer space including hidden dust [56].

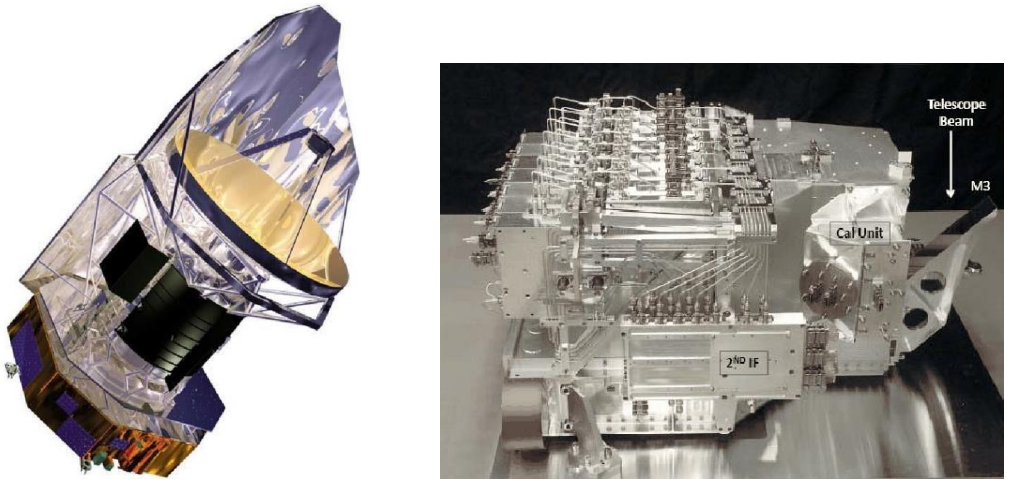

Figure 1.10: (Left) Photograph of Herschel satellite (Adapted from [57]). (Right) Photograph of Heterodyne Instrument for the Far Infrared (HIFI) (Adapted from [58])

The telescope comprises three payloads, two of which are direct detection cameras having medium-resolution spectrometers. These payloads are the Photodetector Array Camera and Spectrometer (PACS), and Spectral and Photometric Imaging REceiver (SPIRE). The other payload comprises a very high-resolution heterodyne spectrometer, which is a Heterodyne Instrument for the Far Infrared (HIFI), as shown in Figure 1.10 (right).

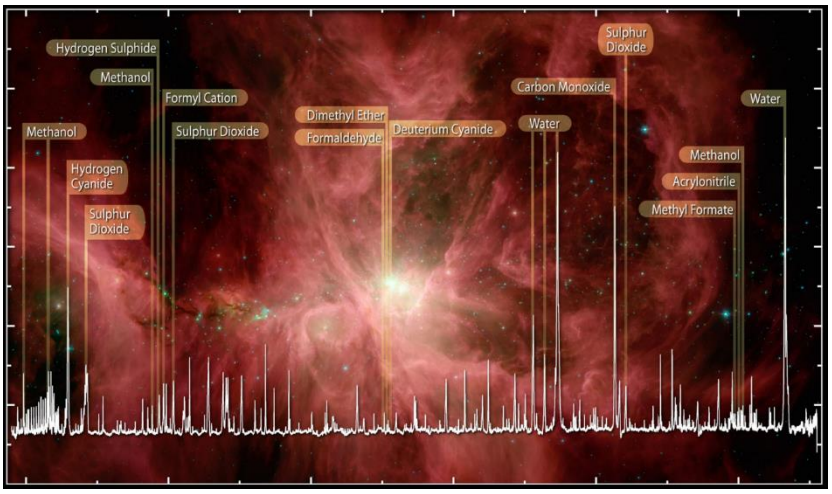

Figure 1.11: Heterodyne Instrument for the Far Infrared (HIFI) spectrum of water and organics in the Orion Nebula (Adapted from [59]).

The HIFI consists of seven electronically tunable heterodyne receivers. Coverage of 0.48 to 1.250 THz using superconductor-insulator-superconductor (SIS) mixers, and frequency span covering from 1.41 to 1.91 THz by using hot electron bolometer (HEB) mixers. The local oscillator (LO) subsystem for these heterodyne receivers consists of a Ka-band synthesizer, followed by 14 chains of frequency multipliers [58], [59]. This frequency span was designated typically to hit the spectrum of water and organics in different galaxies, as shown in Figure 1.11. Each of these instruments helps Herschel capture different aspects of the far-infrared and submillimeter light [54], [56].

The three instruments on Herschel work together, each contributing unique capabilities to enhance the understanding of the universe. With their combined power, Herschel offers broad-band photometric imaging across six different bands, with center frequencies of 4.2, 3, 1.87, 1.2, 0.85, and 0.6 THz; capturing images across various frequency ranges [54], [56].

The main drawback of using frequency chain multiplier as a LO is that, the THz output power is significantly low, typically ranging from a few nanowatts to microwatts.

1.5.4 SOPHIA/GREAT

The Stratospheric Observatory for Infrared Astronomy (SOFIA) is an airborne observatory which was designated to operate in lower stratosphere (45000 feet above sea level). This altitude was specifically chosen to surpass 99.8 % atmospheric water vapour. The instrument suite on SOFIA comprises of broadband imagers, high-resolution spectrometers suitable for studying molecular and atomic gas lines. SOPHIA have numerous payloads operating at various frequency. The one notable instrument was the GREAT (German REceiver for Astronomy at Terahertz Frequencies) which was a THz module, as shown in Figure 1.12 (left).[60], [61], [62].

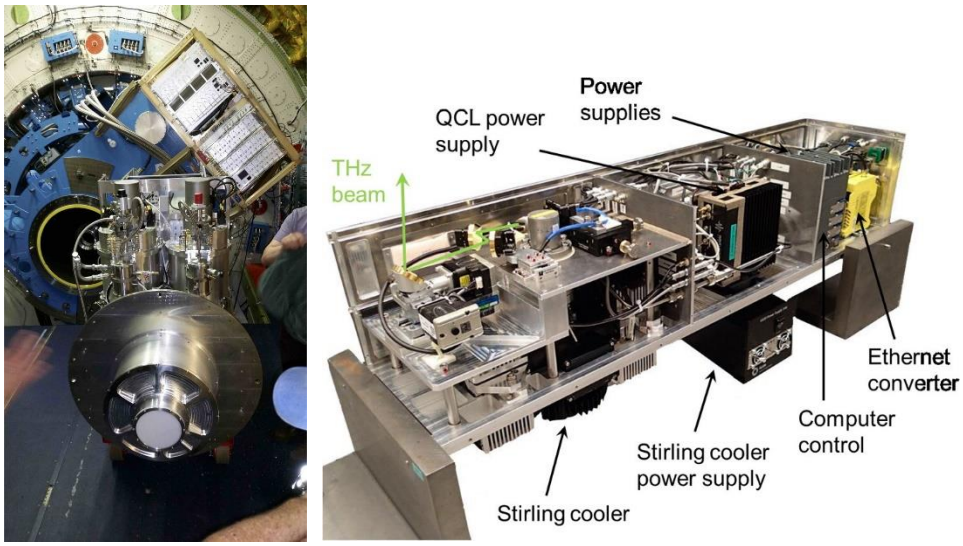

Figure 1.12: (Left) Photograph of the GREAT instrument sitting inside the SOPHIA airborne observatory. (Right) Photograph of the GREAT LO box (Adapted from [62]).

The GREAT was a heterodyne instrument with various configurations designed for high-resolution spectra across multiple frequency ranges between 0.4900–4.7448 THz. Its front-end unit included different channels, including the upGREAT Low-Frequency Array (LFA) using a 14-pixel array operating at the frequency range of 1.835-2.007 THz. Second channel consist of the upGREAT High-Frequency Array (HFA) comprised a 7-pixel array. The LO was based on QCL, which had a

narrow tuning range focused on the [OI] species of frequency at 4.74477749 THz, as shown in Figure 1.12 (right). The last channel consist of 4GREAT, which was the four co-aligned pixels operating at four distinct frequencies: 491-635 GHz, 890-1092 GHz, 1240-1525 GHz, and 2490-2590 GHz [60], [61], [62].

For data processing, the GREAT instrument used eXtended Bandwidth Fast Fourier Transform Spectrometers (XFFTS) as backends. Each XFFTS boasted a bandwidth of 4 GHz and 16,384 channels, achieving a resolution of 244 kHz [60], [61], [62].

The main drawback of using such an airborne observatory is that it relies on the flight capacity of fuel. Each time the observatory has to land whenever the fuel runs low, disrupting its constant presence in the stratosphere.

1.5.5 STO-2/GUSTO

The STO-2 was a NASA-based telescope, launched as a balloon observatory in 2016. It conducted the mission at the South Pole circulating the southern region near Antarctica to study gas clouds between stars, as shown in Figure 1.13. Operating at an altitude of 39 kilometers, the telescope orbited within the polar vortex for 14 days. During this period, STO2 detected ionized nitrogen (NII) at 1.4 THz and ionized carbon (CII) at 1.9 THz in a segment of the Milky Way, indicating star formation processes from dust and gas [63].

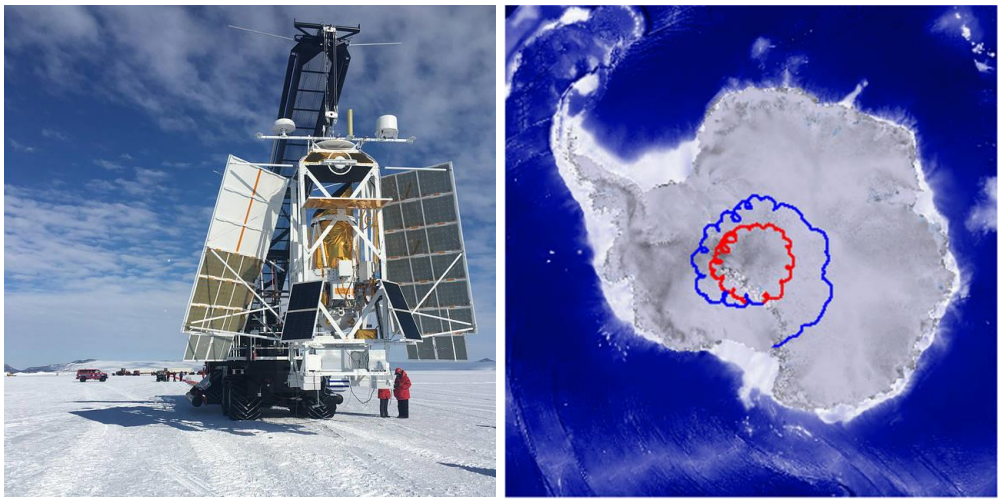

Figure 1.13: (Left) Photograph of theSTO-2. (Right) Photograph of the Flight path of the STO-2 balloon flight around Antarctica (Adapted from [64]).

The THz module used in the telescope was based on a 4.7 THz heterodyne receiver. This receiver used a single-pixel hot electron bolometer mixer pumped by a 4.7 THz 3rd order distributed feedback (DFB) QCL as an LO. The significance of designing a DFB QCL was to specifically emit a single mode frequency at 4.745 THz, which hits the precise absorption line of neutral oxygen (OI), giving a high-resolution spectroscopy for that species [63], [64].

However, a technical malfunction occurred in the QCL-based LO system where an electrical component essential for communication between the LO and ground control overheated due to exposure to excessive solar radiation.

A similar mission named GUSTO, launched in 2021 was also a NASA balloon-borne terahertz observatory aiming to study the interstellar medium life cycle of our galaxy. This mission was planned to orbit for 160-170 days. GUSTO mapped the three brightest interstellar cooling lines including, [OI] at 4.7 THz, [CII] at 1.9 THz, and [NII] at 1.4 THz, across the galactic plane and a part of the Large Magellanic Cloud. It used three arrays of 4x2 mixers based on NbN hot electron bolometers (HEBs) for high-resolution spectroscopic astronomy at these frequencies. A novel 4.7 THz receiver for GUSTO consists of a 4×2 HEB quasi-optical mixer array and a 4.7 THz multi-beam local oscillator (LO), designed to generate eight sub-LO beams for improved observation efficiency [65].

1.5.6 OSAS-B

The Oxygen Spectrometer for Atmospheric Science on a Balloon (OSAS-B), launched in 7th September 2022, was designed for remote sensing of atomic oxygen in the mesosphere and lower thermosphere (MLT) region (The information on MLT region is provided in the following section). The atomic oxygen line which is 4.7448 THz is the dominant species at that region. The previous radiometry approach of atomic oxygen using visible and near-infrared transitions has been challenging due to complex excitation physics. OSAS-B functions as a heterodyne spectrometer targeting the thermally excited ground state transition of atomic oxygen at 4.75 THz [66], [67], [68]. This enables spectrally resolved measurements of the line shape, providing a precise concentration of atomic oxygen in the MLT, as shown in Figure 1.14 (a).

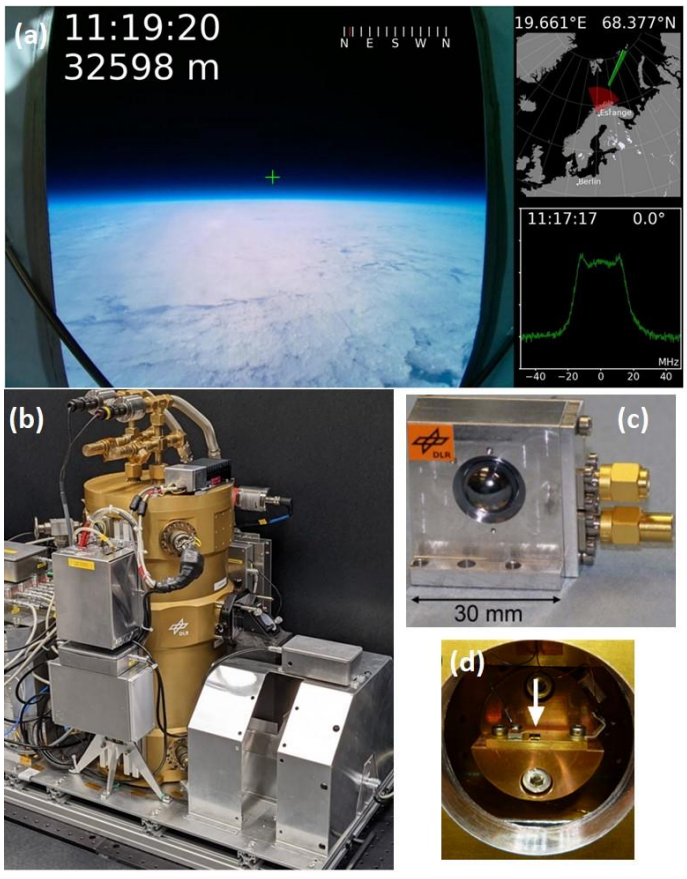

Figure 1.14: (a) OSAS-B onboard camera picture providing the local time, flight altitude, map with the actual position, and acquired atomic oxygen spectrum. (b) OSAS-B THz module (c) Photograph of the mixer block. (d) Photograph of QCL mounted in cryostat. (reproduced from [67])

OSAS-B have a THZ module (as shown in Figure 1.14 (b)), which includes a hot-electron bolometer mixer and a quantum-cascade laser as a local oscillator integrated with helium/nitrogen dewar, as shown in Figure 1.14 (c), (d). A turning mirror will enable sounding at various vertical inclinations.

The QCL ridge was developed as a semi insulating surface plasmon (SI-SP) waveguide (the SI-SP waveguide is discussed in chapter 2), which has a DFB grating and polished rear facet. This design was used to enhance single-mode emission which then will be directed towards the forward direction (from the front facet of QCL). The requirement of QCL operating temperature on OSAS-B was typically in the range of 58-64 K. The output THZ power generated by a QCL was in the range of 1-2 mW and the input electrical power consumed was 0.6-1 W [66], [67], [68].

Since water absorption interferes with observations, this line can only be detected from high-altitude platforms like high-flying airplanes, balloons, or satellites. Recently, the first spectrally resolved observation of the 4.75-THz line was achieved using a heterodyne spectrometer on SOFIA. Compared to SOFIA, a balloon-borne instrument like OSAS-B offers the advantage of not being affected by atmospheric water vapour absorption [66], [67], [68].

However, the primary disadvantage of using a balloon-based satellite is the significant challenge posed by weight and power constraints, particularly because the satellite is exposed to temperatures as low as -80°C and operates in low-pressure environments at higher altitudes. The other drawback is this satellite tended to operate for 6-12 hours which was a reasonably small period of time.

1.5.7 Keystone Terahertz Receiver satellite

THz-QCLs are a relatively new semiconductor device technology, based on intersubband transitions in quantum wells [3]. THz QCLs have been recognised as viable sources for THz radiometry in Space/EO applications, with prominent examples being their recent deployment as 4.7-THz LOs in the SOFIA/GREAT heterodyne spectrometer [62], [69] and the STO-2/GUSTO/OSAS-B balloon observatory [66], [67], [68], [70]. However, key challenges must be addressed before satellite

deployment can be realised. These include the mechanically robust integration of QCLs with other THz system components, the development of frequency tuning methodologies to enable precise targeting of gas emission lines, and the ability to stabilise the LO frequency to improve the receiver noise performance and spectroscopic resolution.

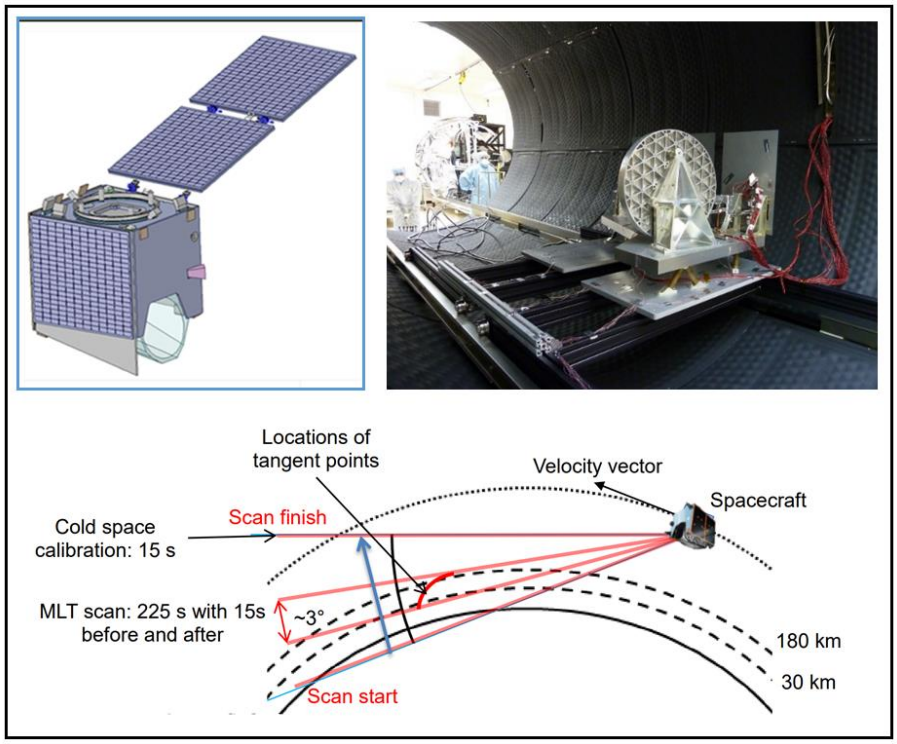

Figure 1.15: KEYSTONE mission concept. Payload is pointed along the velocity vector and the spacecraft scans vertically (Reproduced from [54]).

Keystone is a proposed satellite mission that aims to investigate the mesosphere and lower thermosphere (MLT) region of the Earth's atmosphere from a low Earth orbit. The infrared and supra-terahertz (0.8–4.7 THz) instruments installed in the satellite will be used for limb-sounding, revealing essential aspects of the atmospheric composition in this complex and poorly understood region that has a significant impact on the Earth's climate, as shown in Figure 1.10 [71]

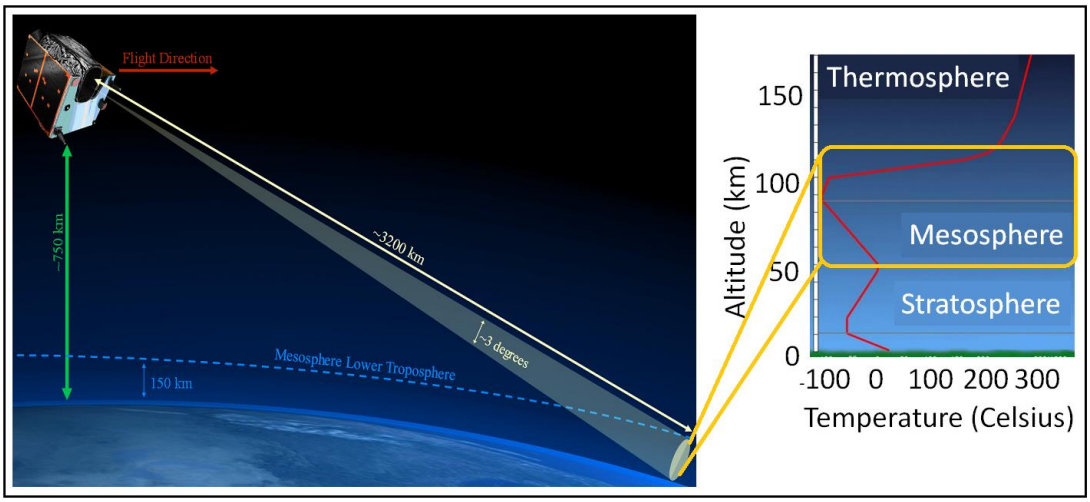

Figure 1.16: Mesosphere lower thermosphere region (Reproduced from [54])

The "gateway" between the Earth's atmosphere and the near-space environment is formed by the mesosphere and lower thermosphere (55–150 km altitude), shown in Figure 1.16. Both natural and man-made activity on Earth's surface, as well as solar and space-weather events from above, have a substantial influence on the MLT. The distinctive feature of the MLT is the intersection of two large energy flows—solar radiation and energetic space particles, balanced by the energy transfer upwards from gravity waves originating from the lower atmosphere [71].

Significant observations have indicated that the mesosphere is cooling 10 times faster than the troposphere due to increasing greenhouse gas concentrations and stratospheric ozone depletion, making it an important indicator of global climate change. Recently, progress in remote-sensing technology installed in satellites has contributed towards the understanding of MLT [71].

Several crucial atmospheric species have yet to be directly measured, despite prior satellite missions. The KEYSTONE mission aims to focus this gap by targeting atomic oxygen (O), which makes up the majority of the atmosphere above 90 km, atmospheric coolants like hydroxyl radical (OH) and carbon monoxide (CO), and nitrous oxide (NO), a species formed by the collision of solar particles [71].

While the abundance of these species may be inferred from infrared observations and detailed modelling up to around 110 km, direct observation of them is only achievable through their THz emission lines, which are between 1 and 5 THz in

frequency. Such direct observations can only be possible by using a sophisticated supra-THz receiver. The KEYSTONE mission will provide a scientific breakthrough by enabling direct observation of atomic oxygen, and other essential MLT species on a global base [71].

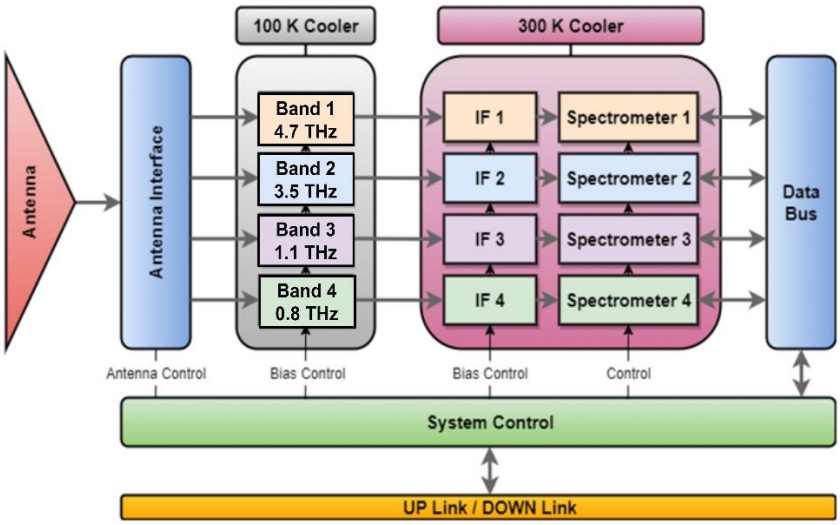

Figure 1.17: Keystone THz Receiver (reproduced from [58])

Table 1.1: Keystone THz receiver band designation

Band	Centre ν (THz)	Primary target Species	Secondary target species
1	4.7	O	O_3
2	3.5	OH	CO_2, HO_2
3	2.0	O	NO, O_3
4	1.15	NO	O_3
5	0.8	O_2	O_3

Table 1: Illustrates that, from five band designations, QCL frequencies will be needed for Band 1, Band 2 and Band 3 which are 4.7 THz, 3.5 THz and 2 THz respectively.

A multi-channel radiometer operating in the 0.8–4.7 THz range is part of the Keystone payload, enabling global high spectral resolution measurements of atomic oxygen and the hydroxyl radical, shown in Figure 1.17.

Ultra-compact QCLs, which are capable of producing high-powered continuous-wave (CW) coherent THz radiation (>10 mW) [35], are used as the LOs for the radiometry channels. Bands 1, 2 and 3 are driven by QCL-based LOs and will be cooled to < 100 K using a RAL Stirling-cycle cooler, as specified in Table 1.1. The first use of supra-THz instrumentation in satellite applications is made possible by this ground-breaking capability [71].

Every band of the THz receivers are a self-contained system which includes a front-end Schottky barrier diode mixer, local oscillator (LO), intermediate-frequency (IF) low-noise amplifier (LNA), and a subsequent chain of further IF amplification and signal-down conversion. Each band also has a fast Fourier transform (FFT) spectrometer in the baseline design, which digitally samples the IF output and outputs a power spectrum of the incident THz signal with a typical bandwidth of 2 GHz and spectral resolution of 1 MHz [71]. For mechanical robustness, QCL need to be integrated in waveguide block, having a single mode emission. For vibration and other noise fluctuation, QCL require to be have a stable frequency and output power. Ideally, the LO should efficiently dissipate heat to operate at temperatures below 100 K. To meet this criteria, the desired electrical power consumption of the QCL should be limited to 1 W. The LO requirements for the Keystone Terahertz receiver satellite are outlined in Table 1.2.

Table 1.2 : LO requirements for the Keystone satellite

Requirements	**Specification**
Cooling Temperature	< 100 K
THz Power Requirement	> 10 mW
LO Type	Waveguide Integrated
Emission	Single Mode
Operation Mode	Continuous Wave (CW)
QCL short-term frequency drift	50 ppm/K
QCL amplitude stability	1% of output power
QCL integrated linewidth	0.1 MHz
QCL Power dissipation	1 W

1.6 Project aims and thesis structure

QCLs are tunable lasers with exceptional power in the THz range. They are well suited for use in satellite applications due to their compact size. The main objective of the thesis is to demonstrate advancements in the development of waveguide-integrated THz QCLs, intended for use as an LO in the front-end of the KEYSTONE satellite receiver. The thesis aim to show a progress twards completing the LO requirement outlined in Table 1.2.

The work in this project was to provide a thorough discussion on the fabrication and characterisation of QCL devices required for the KEYSTONE satellite receiver, and also address the challenges encountered in fabricating QCL devices. The detailed discussions are covered in Chapter 2.

In Chapter 3, a detailed demonstration of QCL power locking is provided, focusing on its significance in stabilizing the optical output power of QCL. This stability is a critical factor in the context of space research applications.

The development of waveguide-integrated THz QCLs is covered in detail in Chapter 4, along with their fabrication process, working principles, characterisation, and the challenges encountered with the integration approach.

Chapter 5 outlines the demonstration of a rapid THz detection and modulation approach, with a focus on THz gas spectroscopy and the progress made towards frequency locking.

The results obtained in this research provide a solid foundation for future endeavours in the development of THz QCLs as Local Oscillators. Finally, chapter 6 provides concluding remarks and possible future work.

Bibliography

[1] A. G. Davies et al., ‘Terahertz quantum cascade lasers’, Philos. Trans. R. Soc. Lond. Ser. Math. Phys. Eng. Sci., vol. 362, no. 1815, pp. 215–231, Dec. 2003, doi: 10.1098/rsta.2003.1313.

[2] B. S. Williams, S. Kumar, H. Callebaut, Q. Hu, and J. L. Reno, ‘Terahertz quantum-cascade laser at $\lambda \approx 100\,\mu m$ using metal waveguide for mode confinement’, Appl. Phys. Lett., vol. 83, no. 11, pp. 2124–2126, Sep. 2003, doi: 10.1063/1.1611642.

[3] C. Sirtori, ‘Bridge for the terahertz gap’, Nature, vol. 417, no. 6885, Art. no. 6885, May 2002, doi: 10.1038/417132b.

[4] A. Y. Pawar, D. D. Sonawane, K. B. Erande, and D. V. Derle, ‘Terahertz technology and its applications’, Drug Invent. Today, vol. 5, no. 2, pp. 157–163, Jun. 2013, doi: 10.1016/j.dit.2013.03.009.

[5] S. Kumar, ‘Recent Progress in Terahertz Quantum Cascade Lasers’, IEEE J. Sel. Top. Quantum Electron., vol. 17, no. 1, pp. 38–47, Jan. 2011, doi: 10.1109/JSTQE.2010.2049735.

[6] A. G. Davies, A. D. Burnett, W. Fan, E. H. Linfield, and J. E. Cunningham, ‘Terahertz spectroscopy of explosives and drugs’, Mater. Today, vol. 11, no. 3, pp. 18–26, Mar. 2008, doi: 10.1016/S1369-7021(08)70016-6.

[7] H.-J. Song and T. Nagatsuma, ‘Present and Future of Terahertz Communications’, IEEE Trans. Terahertz Sci. Technol., vol. 1, no. 1, pp. 256–263, Sep. 2011, doi: 10.1109/TTHZ.2011.2159552.

[8] J. Federici and L. Moeller, ‘Review of terahertz and subterahertz wireless communications’, J. Appl. Phys., vol. 107, no. 11, p. 111101, Jun. 2010, doi: 10.1063/1.3386413.

[9] K. Kawase, Y. Ogawa, Y. Watanabe, and H. Inoue, ‘Non-destructive terahertz imaging of illicit drugs using spectral fingerprints’, Opt. Express, vol. 11, no. 20, pp. 2549–2554, Oct. 2003, doi: 10.1364/OE.11.002549.

[10] A. G. Davies, E. H. Linfield, M. Pepper, and P. F. Taday, ‘Applications of terahertz spectroscopy to pharmaceutical sciences’, Philos. Trans. R. Soc. Lond.

Ser. Math. Phys. Eng. Sci., vol. 362, no. 1815, pp. 351–364, Dec. 2003, doi: 10.1098/rsta.2003.1321.

[11] R. M. Woodward et al., ‘Terahertz Pulse Imaging of ex vivo Basal Cell Carcinoma’, J. Invest. Dermatol., vol. 120, no. 1, pp. 72–78, Jan. 2003, doi: 10.1046/j.1523-1747.2003.12013.x.

[12] A. G. Davies et al., ‘Label–free THz sensing of genetic sequences: towards “THz biochips”’, Philos. Trans. R. Soc. Lond. Ser. Math. Phys. Eng. Sci., vol. 362, no. 1815, pp. 323–335, Dec. 2003, doi: 10.1098/rsta.2003.1318.

[13] V. P. Wallace et al., ‘Terahertz pulsed imaging of basal cell carcinoma ex vivo and in vivo’, Br. J. Dermatol., vol. 151, no. 2, pp. 424–432, Aug. 2004, doi: 10.1111/j.1365-2133.2004.06129.x.

[14] A. J. Fitzgerald et al., ‘Terahertz Pulsed Imaging of Human Breast Tumors’, Radiology, vol. 239, no. 2, pp. 533–540, May 2006, doi: 10.1148/radiol.2392041315.

[15] B. Karagoz, H. Altan, and K. Kamburoglu, ‘Terahertz pulsed imaging study of dental caries’, in Medical Laser Applications and Laser-Tissue Interactions VII, SPIE, Jul. 2015, pp. 123–130. doi: 10.1117/12.2183673.

[16] A. G. Davies, E. H. Linfield, M. Pepper, and J. M. Chamberlain, ‘Where optics meets electronics: recent progress in decreasing the terahertz gap’, Philos. Trans. R. Soc. Lond. Ser. Math. Phys. Eng. Sci., vol. 362, no. 1815, pp. 199–213, Dec. 2003, doi: 10.1098/rsta.2003.1312.

[17] C. Kulesa, ‘Terahertz Spectroscopy for Astronomy: From Comets to Cosmology’, IEEE Trans. Terahertz Sci. Technol., vol. 1, no. 1, pp. 232–240, Sep. 2011, doi: 10.1109/TTHZ.2011.2159648.

[18] D. M. Mittleman, R. H. Jacobsen, R. Neelamani, R. G. Baraniuk, and M. C. Nuss, ‘Gas sensing using terahertz time-domain spectroscopy’, Appl. Phys. B, vol. 67, no. 3, pp. 379–390, Sep. 1998, doi: 10.1007/s003400050520.

[19] D. H. Auston, ‘Picosecond optoelectronic switching and gating in silicon’, Appl. Phys. Lett., vol. 26, no. 3, pp. 101–103, Feb. 1975, doi: 10.1063/1.88079.

[20] M. Feiginov, H. Kanaya, S. Suzuki, and M. Asada, ‘Operation of resonant-tunneling diodes with strong back injection from the collector at frequencies up to 1.46 THz’, Appl. Phys. Lett., vol. 104, no. 24, p. 243509, Jun. 2014, doi: 10.1063/1.4884602.

[21] A. Khalid et al., ‘Terahertz oscillations in an In0.53Ga0.47As submicron planar Gunn diode’, J. Appl. Phys., vol. 115, no. 11, p. 114502, Mar. 2014, doi: 10.1063/1.4868705.

[22] L. N. Kurbatov et al., ‘Far-IR heterojunction lasers tunable to 46.2 μm’, ZhETF Pisma Redaktsiiu, vol. 37, pp. 422–424, May 1983.

[23] E. R. Brown, K. A. McIntosh, K. B. Nichols, and C. L. Dennis, ‘Photomixing up to 3.8 THz in low-temperature-grown GaAs’, Appl. Phys. Lett., vol. 66, no. 3, pp. 285–287, Jan. 1995, doi: 10.1063/1.113519.

[24] M. Tani, O. Morikawa, S. Matsuura, and M. Hangyo, ‘Generation of terahertz radiation by photomixing with dual- and multiple-mode lasers’, Semicond. Sci. Technol., vol. 20, no. 7, p. S151, Jun. 2005, doi: 10.1088/0268-1242/20/7/005.

[25] M. Beck et al., ‘Impulsive terahertz radiation with high electric fields from an amplifier-driven large-area photoconductive antenna’, Opt. Express, vol. 18, no. 9, pp. 9251–9257, Apr. 2010, doi: 10.1364/OE.18.009251.

[26] J. Zhang, Y. Hong, S. L. Braunstein, and K. A. Shore, ‘Terahertz pulse generation and detection with LT-GaAs photoconductive antenna’, IEE Proc. - Optoelectron., vol. 151, no. 2, pp. 98–101, Apr. 2004.

[27] J. Shikata, K. Kawase, K. Karino, T. Taniuchi, and H. Ito, ‘Tunable terahertz-wave parametric oscillators using LiNbO/sub 3/ and MgO:LiNbO/sub 3/ crystals’, IEEE Trans. Microw. Theory Tech., vol. 48, no. 4, pp. 653–661, Apr. 2000, doi: 10.1109/22.841956.

[28] K. Radhanpura, S. Hargreaves, R. A. Lewis, L. Sirbu, and I. M. Tiginyanu, ‘Heavy noble gas (Kr, Xe) irradiated (111) InP nanoporous honeycomb membranes with enhanced ultrafast all-optical terahertz emission’, Appl. Phys. Lett., vol. 97, no. 18, p. 181921, Nov. 2010, doi: 10.1063/1.3509404.

[29] S. Hargreaves, K. Radhanpura, and R. A. Lewis, ‘Generation of terahertz radiation by bulk and surface optical rectification from crystal planes of arbitrary orientation’, Phys. Rev. B, vol. 80, no. 19, 2009, Accessed: Apr. 03, 2023.

[30] J. H. Booske et al., ‘Vacuum Electronic High Power Terahertz Sources’, IEEE Trans. Terahertz Sci. Technol., vol. 1, no. 1, pp. 54–75, Sep. 2011, doi: 10.1109/TTHZ.2011.2151610.

[31] T. Y. Chang, T. J. Bridges, and E. G. Burkhardt, ‘cw SUBMILLIMETER LASER ACTION IN OPTICALLY PUMPED METHYL FLUORIDE, METHYL

ALCOHOL, AND VINYL CHLORIDE GASES', Appl. Phys. Lett., vol. 17, no. 6, pp. 249–251, Sep. 1970, doi: 10.1063/1.1653386.

[32] T. Y. Chang, 'Optically Pumped Submillimeter-Wave Sources', IEEE Trans. Microw. Theory Tech., vol. 22, no. 12, pp. 983–988, Dec. 1974, doi: 10.1109/TMTT.1974.1128409.

[33] R. Haug, Advances in Solid State Physics 48. Springer Science & Business Media, 2008.

[34] A. Bergner et al., 'New p-Ge THz laser spectrometer for the study of solutions: THz absorption spectroscopy of water', Rev. Sci. Instrum., vol. 76, no. 6, p. 063110, Jun. 2005, doi: 10.1063/1.1928427.

[35] R. Köhler et al., 'Terahertz semiconductor-heterostructure laser', Nature, vol. 417, no. 6885, pp. 156–159, May 2002, doi: 10.1038/417156a.

[36] K. Delfanazari, R. A. Klemm, H. J. Joyce, D. A. Ritchie, and K. Kadowaki, 'Integrated, Portable, Tunable, and Coherent Terahertz Sources and Sensitive Detectors Based on Layered Superconductors', Proc. IEEE, vol. 108, no. 5, pp. 721–734, May 2020, doi: 10.1109/JPROC.2019.2958810.

[37] S. Fathololoumi et al., '199.5 K Operation of THz Quantum Cascade Lasers', in Conference on Lasers and Electro-Optics 2012 (2012), paper CTu2B.1, Optica Publishing Group, May 2012, p. CTu2B.1. doi: 10.1364/CLEO_SI.2012.CTu2B.1.

[38] M. Tonouchi, 'Cutting-edge terahertz technology', Nat. Photonics, vol. 1, pp. 97–105, Feb. 2007, doi: 10.1038/nphoton.2007.3.

[39] B. Ferguson and X.-C. Zhang, 'Materials for terahertz science and technology', Nat. Mater., vol. 1, no. 1, Art. no. 1, Sep. 2002, doi: 10.1038/nmat708.

[40] M. Razeghi, 'Semiconductor Lasers', in Technology of Quantum Devices, M. Razeghi, Ed., Boston, MA: Springer US, 2010, pp. 209–270. doi: 10.1007/978-1-4419-1056-1_6.

[41] J. Faist, F. Capasso, D. L. Sivco, C. Sirtori, A. L. Hutchinson, and A. Y. Cho, 'Quantum cascade laser', Science, vol. 264, no. 5158, pp. 553–556, Apr. 1994, doi: 10.1126/science.264.5158.553.

[42] H.-W. Hübers, R. Eichholz, S. G. Pavlov, and H. Richter, 'High Resolution Terahertz Spectroscopy with Quantum Cascade Lasers', J. Infrared Millim.

Terahertz Waves, vol. 34, no. 5, pp. 325–341, Jun. 2013, doi: 10.1007/s10762-013-9973-7.

[43] P. Y. Han, M. Tani, M. Usami, S. Kono, R. Kersting, and X.-C. Zhang, 'A direct comparison between terahertz time-domain spectroscopy and far-infrared Fourier transform spectroscopy', J. Appl. Phys., vol. 89, no. 4, pp. 2357–2359, Feb. 2001, doi: 10.1063/1.1343522.

[44] A. Rostami, H. Rasooli, and H. Baghban, Terahertz Technology: Fundamentals and Applications, vol. 77. in Lecture Notes in Electrical Engineering, vol. 77. Berlin, Heidelberg: Springer, 2011. doi: 10.1007/978-3-642-15793-6.

[45] S. Nashima, O. Morikawa, K. Takata, and M. Hangyo, 'Temperature dependence of optical and electronic properties of moderately doped silicon at terahertz frequencies', J. Appl. Phys., vol. 90, no. 2, pp. 837–842, Jul. 2001, doi: 10.1063/1.1376673.

[46] D. M. Mittleman, J. Cunningham, M. C. Nuss, and M. Geva, 'Noncontact semiconductor wafer characterization with the terahertz Hall effect', Appl. Phys. Lett., vol. 71, no. 1, pp. 16–18, Jul. 1997, doi: 10.1063/1.119456.

[47] H. Zhong et al., 'Nondestructive defect identification with terahertz time-of-flight tomography', IEEE Sens. J., vol. 5, no. 2, pp. 203–208, Apr. 2005, doi: 10.1109/JSEN.2004.841341.

[48] A. W. M. Lee, B. S. Williams, S. Kumar, Q. Hu, and J. L. Reno, 'Real-time imaging using a 4.3-THz quantum cascade laser and a 320 /spl times/ 240 microbolometer focal-plane array', IEEE Photonics Technol. Lett., vol. 18, no. 13, pp. 1415–1417, Jul. 2006, doi: 10.1109/LPT.2006.877220.

[49] A. Valavanis et al., 'Development of Terahertz Quantum-Cascade Lasers for Satellite-Borne Measurement of Key Gas Species', in Conference on Lasers and Electro-Optics, San Jose, California: OSA, 2019, p. AW3P.5. doi: 10.1364/CLEO_AT.2019.AW3P.5.

[50] A. Dunn et al., 'High-speed modulation of a terahertz quantum cascade laser by coherent acoustic phonon pulses', Nat. Commun., vol. 11, no. 1, p. 835, Feb. 2020, doi: 10.1038/s41467-020-14662-w.

[51] A. Valavanis et al., 'Waveguide-integrated THz Quantum-Cascade Lasers for Atmospheric-Research Satellite Payloads', in 2019 IEEE MTT-S International

Wireless Symposium (IWS), Guangzhou, China: IEEE, May 2019, pp. 1–3. doi: 10.1109/IEEE-IWS.2019.8803875.

[52] J. W. Waters et al., ‘The Earth observing system microwave limb sounder (EOS MLS) on the aura Satellite’, IEEE Trans. Geosci. Remote Sens., vol. 44, no. 5, pp. 1075–1092, May 2006, doi: 10.1109/TGRS.2006.873771.

[53] H. M. Pickett, ‘Microwave Limb Sounder THz module on Aura’, IEEE Trans. Geosci. Remote Sens., vol. 44, no. 5, pp. 1122–1130, May 2006, doi: 10.1109/TGRS.2005.862667.

[54] L. F. Rolo, M. H. Paquay, R. J. Daddato, J. A. Parian, D. Doyle, and P. de Maagt, ‘Terahertz Antenna Technology and Verification: Herschel and Planck - A Review’, IEEE Trans. Microw. Theory Tech., vol. 58, no. 7, pp. 2046–2063, Jul. 2010, doi: 10.1109/TMTT.2010.2050179.

[55] N. Aghanim et al., ‘Planck 2018 results - III. High Frequency Instrument data processing and frequency maps’, Astron. Astrophys., vol. 641, p. A3, Sep. 2020, doi: 10.1051/0004-6361/201832909.

[56] G. L. Pilbratt et al., ‘Herschel Space Observatory - An ESA facility for far-infrared and submillimetre astronomy’, Astron. Astrophys., vol. 518, p. L1, Jul. 2010, doi: 10.1051/0004-6361/201014759.

[57] M. Signore and D. Puy, ‘Cosmic microwave background and first molecules in the early universe’, Eur. Phys. J. C, vol. 59, no. 1, pp. 117–172, Jan. 2009, doi: 10.1140/epjc/s10052-008-0807-z.

[58] T. de Graauw et al., ‘The Herschel-Heterodyne Instrument for the Far-Infrared (HIFI)’, Astron. Astrophys., vol. 518, p. L6, Jul. 2010, doi: 10.1051/0004-6361/201014698.

[59] D. Kester, R. Higgins, and D. Teyssier, ‘Derivation of sideband gain ratio for Herschel /HIFI’, Astron. Astrophys., vol. 599, p. A115, Mar. 2017, doi: 10.1051/0004-6361/201629553.

[60] R. Guesten et al., ‘GREAT: the first-generation German heterodyne receiver for SOFIA’, in Airborne Telescope Systems, SPIE, Jun. 2000, pp. 23–30. doi: 10.1117/12.389122.

[61] S. Heyminck, U. U. Graf, R. Güsten, J. Stutzki, H. W. Hübers, and P. Hartogh, ‘GREAT: the SOFIA high-frequency heterodyne instrument’, Astron. Astrophys., vol. 542, p. L1, Jun. 2012, doi: 10.1051/0004-6361/201218811.

[62] C. Risacher et al., ‘The upGREAT Dual Frequency Heterodyne Arrays for SOFIA’, J. Astron. Instrum., vol. 07, no. 04, p. 1840014, Dec. 2018, doi: 10.1142/S2251171718400147.

[63] D. J. Hayton et al., ‘A 4.7 THz HEB/QCL heterodyne receiver for STO-2’, in 2014 39th International Conference on Infrared, Millimeter, and Terahertz waves (IRMMW-THz), Sep. 2014, pp. 1–2. doi: 10.1109/IRMMW-THz.2014.6956203.

[64] D. J. Lawrence et al., ‘Near-space operation of compact CsI, CLYC, and CeBr3 sensors: Results from two high-altitude balloon flights’, Nucl. Instrum. Methods Phys. Res. Sect. Accel. Spectrometers Detect. Assoc. Equip., vol. 905, pp. 33–46, Oct. 2018, doi: 10.1016/j.nima.2018.07.026.

[65] J. R. G. Silva et al., ‘4×2 HEB receiver at 4.7 THz for GUSTO’, in Millimeter, Submillimeter, and Far-Infrared Detectors and Instrumentation for Astronomy IX, SPIE, Jul. 2018, pp. 200–209. doi: 10.1117/12.2313410.

[66] M. Wienold, A. Semenov, H. Richter, and H.-W. Hübers, ‘OSAS-B: a balloon-borne heterodyne spectrometer for sounding atomic oxygen in the MLT region’, Copernicus Meetings, EGU21-10874, Mar. 2021. doi: 10.5194/egusphere-egu21-10874.

[67] M. Wienold et al., ‘OSAS-B: A balloon-borne terahertz spectrometer for atomic oxygen in the upper atmosphere’, IEEE Trans. Terahertz Sci. Technol., pp. 1–9, 2024, doi: 10.1109/TTHZ.2024.3363135.

[68] M. Wienold et al., ‘OSAS-B: a 4.7-THz Heterodyne Spectrometer for Atomic Oxygen in the Mesosphere and Lower Thermosphere’, in 2023 48th International Conference on Infrared, Millimeter, and Terahertz Waves (IRMMW-THz), Sep. 2023, pp. 1–2. doi: 10.1109/IRMMW-THz57677.2023.10299165.

[69] H. Richter, M. Wienold, L. Schrottke, K. Biermann, H. T. Grahn, and H.-W. Hübers, ‘4.7-THz Local Oscillator for the GREAT Heterodyne Spectrometer on SOFIA’, IEEE Trans. Terahertz Sci. Technol., vol. 5, no. 4, pp. 539–545, Jul. 2015, doi: 10.1109/TTHZ.2015.2442155.

[70] P. N. Bernasconi, D. M. Rust, H. A. Eaton, and G. A. Murphy, ‘Balloon-borne telescope for high-resolution solar imaging and polarimetry’, presented at the Astronomical Telescopes and Instrumentation, R. K. Melugin and H.-P. Roeser, Eds., Munich, Germany, Jun. 2000, p. 214. doi: 10.1117/12.389100.

[71] S. P. Rea et al., ‘The Low-Cost Upper-Atmosphere Sounder (LOCUS)’, 26th International Symposium on Space Terahertz Technology. Accessed: Apr. 03, 2023.

Chapter 2
Terahertz quantum cascade lasers

This chapter provides fundamental concepts crucial for understanding QCLs. It explains the role of heterostructures and quantum confinement, shedding light on how these factors influence the behaviour of electrons within quantum wells. It also discusses the fundamental principles that govern how QCLs operate, as well as the essential components within QCLs, such as active regions and laser waveguides.

Furthermore, the chapter highlights the fabrication and characterization of THz QCL devices. Specifically, focusing on two QCL devices emitting at ~ 5 THz and 3 THz. The characterization results include various analyses, such as Light-Current-Voltage (LIV) measurements taken at different heat-sink temperatures, spectral analysis, and an evaluation of device performance against the requirements for KEYSTONE satellite applications.

2.1 Quantum cascade laser theory

2.1.1 Quantum well Background

Nanoscale materials can be broken down into three different types, quantum wells, quantum wires and quantum dots which can be classified based on their quantum confinement and density of states. These types are represented as two, one and zero dimensional respectively [1].

Single quantum wells can be fabricated by sandwiching one semiconductor thin layer of material ‘A’ between two semiconductor thick layers of material ‘B’ forming a heterojunction. The method of designing a quantum well came by introducing a Low Dimensional system (or structure). The physicochemical characteristics of bulk solids change when the size of the solid is shrunk. This undergoes a change in the mechanical,

chemical, magnetic, electrical and optical properties. Such structures are called low-dimensional structures (or systems). Usually, electrons and holes present in the low dimensional structure change their behaviour pattern which falls in the category of quantum-size effects. Heterostructures like GaAs and AlGaAs are most relevant and popular for designing a quantum well because they have closely matched lattice constants and the same crystal structures which is important for high-quality crystal growth [2].

When the various semiconductor materials are combined to produce a heterostructure in a quantum well, the bonds between the materials are formed at the atomic level. Heterostructures are formed by several heterojunctions consisting of a semiconductor crystal formed by two materials which are aligned head-to-head.

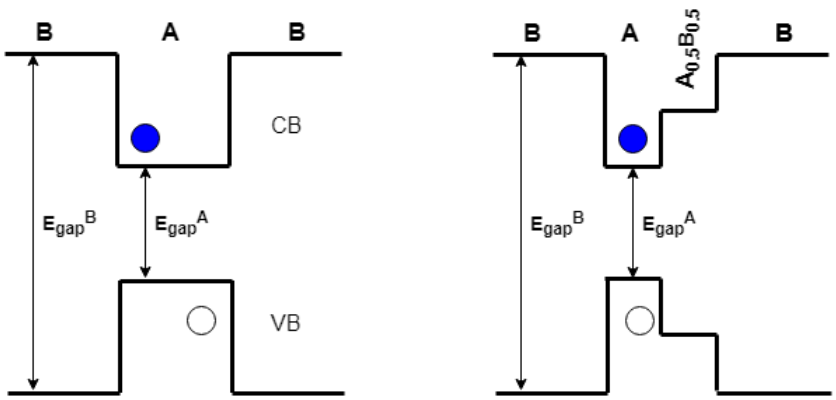

Figure 2.1: (Left) Single Quantum Well (reproduced [3]), (Right) Stepped quantum well (reproduced [3])

In Figure 2.1, two heterojunctions are used such that a layer of material ‘A’ is sandwiched between two layers of material ‘B’, where material ‘A’ has a narrow bandgap compared to material ‘B’. As discussed previously, these two heterojunctions form a heterostructure which is called a “single quantum well”. Figure 2.1 (Left) illustrates a typical single quantum well with potentials $V(z)$ in conduction and valence bands. The stepped quantum well can also be fabricated by adding an alloy between material ‘A’ and ‘B’, in Figure 2.1 (Right), the alloy of 50% doping of both materials ‘A’ and ‘B’ is added in the quantum well [3].

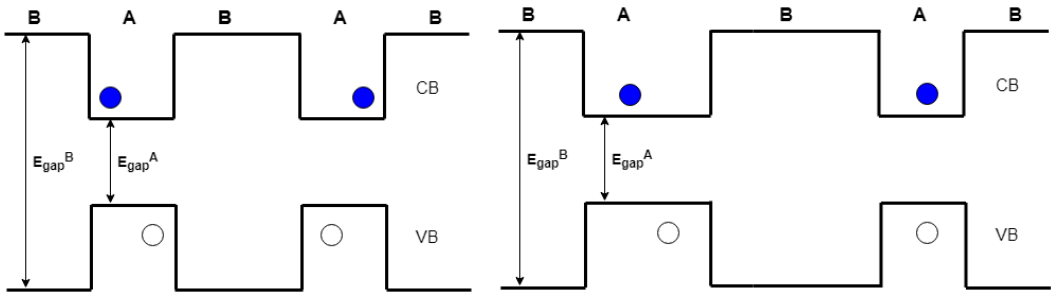

Figure 2.2: (Left) Asymmetrical double quantum well (reproduced [3]), (Right)Symmetrical double quantum well (reproduced [3])

Moving towards complex heterostructures where a number of heterojunctions are used, Figure 2.2 show two heterostructures to form a symmetrical double quantum well and an asymmetrical double quantum well respectively. For the fabrication of a symmetrical double quantum well, two identical single quantum wells are placed adjacent with the same well length, shown in Figure 2.2 (Left). Likewise, asymmetrical double quantum well can be fabricated, but in this the lengths of the two single quantum wells are different Figure 2.2 (Right). Similarly, multiple quantum wells can also be fabricated using multiple heterostructures [3].

Heterostructures have a wide range of applications in various fields including electronics, optics, and optoelectronics. The integration of heterostructures in these fields has led to the development of advanced electronic devices, such as resonant tunnelling diodes, modulation-doped field-effect transistors, and heterojunction bipolar transistors, which offer improved performance and functionality. They can also be used in optical components like mirrors, resonators, waveguides and in optoelectronic device consisting of laser diodes, quantum well photodetectors and many more. However, heterostructures could have one of the most important technologies by integrating all the uses discussed previously (advanced electronic device, optical components and optoelectronic devices) [4].

Schrödinger's equation can be used to deduce a wave equation of an electron, inside a QW. The Schrödinger's equation has two forms, time dependant and time independent [5],[6]. Generally, the time dependent Schrödinger's equation is used to analyse the wave mechanics [7], where the time independent Schrödinger's equation is used to calculate the allowed energies within the structure [8]. A discussion of the time independent solution is given below.

As per De Broglie equation, the wavelength (λ) of a particle is always related to its momentum (p) as [3];

$$\lambda = h\,p \tag{2.1}$$

The wave function for a particle in free space can be written in the plane-wave form

$$\varphi = Ae^{i(k.r-\omega t)} \tag{2.2}$$

where 'A' is amplitude of the wave function, 'r' represents the spatial location, 'ω' is the angular frequency, $k = \frac{2\pi}{\lambda}$ is the wave vector, and 't' is time [9].

Observable values may be extracted from the wave function by using the corresponding quantum mechanical operator. For example, the momentum 'p', is found by applying the $\hat{p} = -i\hbar\nabla$ operator.

$$-i\hbar\nabla\varphi = p\varphi = \hat{p}\varphi \tag{2.3}$$

where

$$\nabla = \frac{\partial}{\partial x}i + \frac{\partial}{\partial y}j + \frac{\partial}{\partial z}k \tag{2.4}$$

and,

$$\hbar = \frac{h}{2\pi} \tag{2.5}$$

Thus, momentum in the form of eigenvalue can be deduced as

$$p = \hbar\left(k_x i + k_y j + k_z k\right) = \hbar k \tag{2.6}$$

For a particle in an external potential, the total energy (E) is the sum of potential (V) and kinetic (T) energies

$$T\varphi + V\varphi = E\varphi \tag{2.7}$$

For a free particle, $V = 0$ and therefore the total energy (E) will be equal to kinetic energy (T).

$$T\varphi = E\varphi \tag{2.8}$$

$$E\varphi = -\frac{\hbar^2}{2m}\nabla^2\varphi \tag{2.9}$$

The equation (2.10) is called the "time independent Schrödinger's equation". In one dimension, this reduces to:

$$E\varphi(z) = -\frac{\hbar^2}{2m}\frac{\partial^2}{\partial z^2}\varphi(z) \qquad (2.10)$$

For a free particle as in (2.2), it can be shown that, $E = \frac{\hbar^2 \mathrm{k}^2}{2m}$

In the study of quantum mechanics, the infinite quantum well is one of the first structure to be studied. It is the simplest and the ideal structure of the quantum well. The potential energy inside the well is zero ($V(z) = 0$) and outside the well is infinite ($V(z) = \infty$), as shown in Figure 2.3 [9].

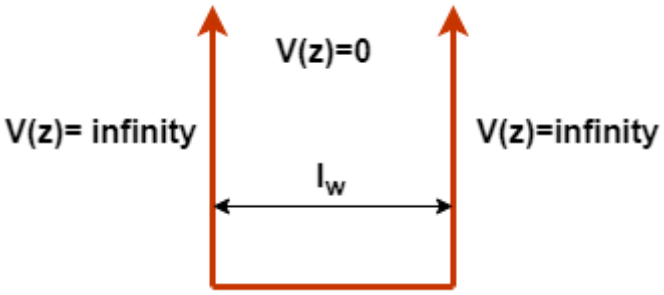

Figure 2.3

Figure 2.3: The one-dimensional infinite well (reproduced [30])

The wavefunction can be determined by considering the combination of the function $f(z)$ which can be double differentiated to get $-f(z)$, where the solution for φ is a linear combination of the functions $f(z)$ [9].

So, the equation of wavefunction will be,

$$\varphi(z) = Asin(kz) + Bcos(kz) \qquad (2.11)$$

Consider length of the well (l_w) from the origin in z-axis. The $\varphi(z)$ in a region is zero when potential energy in that region is infinite. Therefore, $\varphi(z)$ outside the well will be zero, i.e. at $z = 0$ and $z = l_w$, $\varphi(0) = 0$.

$$\varphi(0) = Asin(0) + Bcos(0) = 0 \qquad (2.12)$$

From the equation (2.12), $B = 0$

Therefore, the equation of the wavefunction $\varphi(z)$ will be,

$$\varphi(z) = Asin(kz) \tag{2.13}$$

Further, $\varphi(0) = \varphi(l_w) = 0$

From the equation (2.13), we can represent,

$$k = \frac{\pi n}{l_w} \tag{2.14}$$

Thus, by substituting the equation (2.14) into Schrodinger's equation, the energy in the confined states can be deduced as:

$$E_n = \frac{\hbar^2 \pi^2 n^2}{2m{l_w}^2} \tag{2.15}$$

For calculating the Energy of an electron in GaAs, effective mass (m*) for the particle mass (m) should be considered.

As described previously, a QW structure is designed by placing a narrow bandgap material between two wider bandgap materials. If the well thickness decreases then the wave function of electrons and holes are confined to a narrower region, illustrated in Figure 2.4 [4]. Also, E_n increases as l_w decreases, shown in equation (2.15).

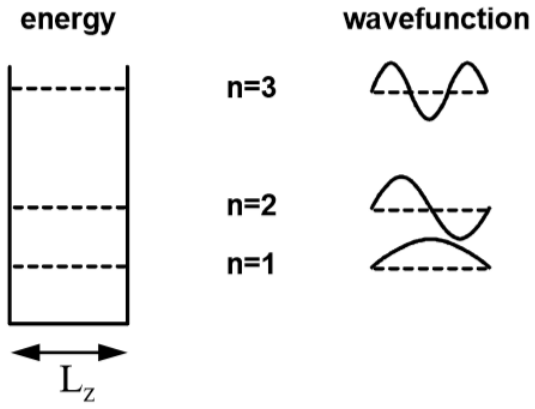

Figure 2.4: Energy levels in QW and corresponding wave function (adapted from [4])

Note that the solutions are much more complicated for finite wells or heterostructures, and need numerical solvers. However, the general principle discussed here give a qualitative understanding of the behaviour of electrons in such devices.

2.1.2 Quantum cascade laser background

In 1971, Kazarinov and Suris provided the idea of QCLs [11]. They proposed an idea of controlling frequency in the same semiconductor material by varying the width of the quantum well based on the intersubband transition. However, this idea was just a concept and was not implemented practically. In 1994, the first demonstration was put forward by Faist at Bell Laboratories which worked at mid-IR frequencies. The very first working QCL was fabricated which was for short wavelengths (4.2 μm) and peak power at 8 mW in pulsed mode at 10 K [12].

In QCLs the layer thickness plays an important role in the position of the energy level, instead of the material. While using a same material, possible tuning of emission wavelength for a wide range can be achieved in QCL [13].

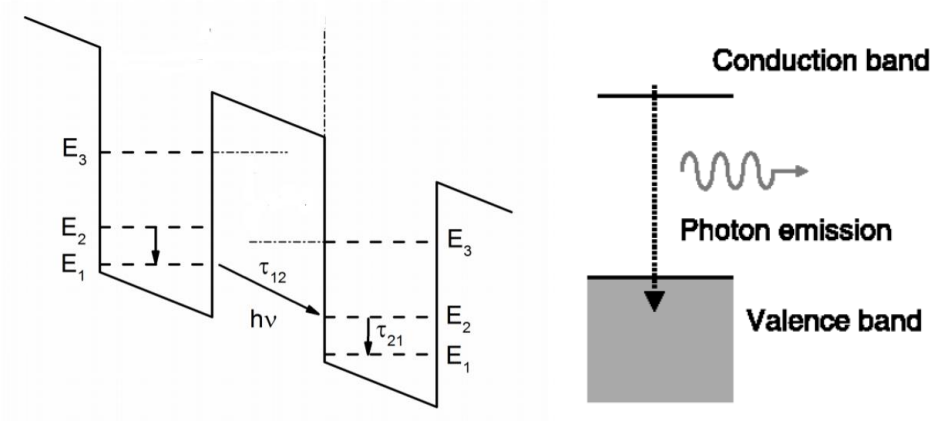

Figure 2.5: (Left) Quantum Cascade Laser (adapted from [14]),
(Right) Conventional Laser (adapted from [15])

Figure 2.5 (Left) illustrates that, an electron in a QCL can emit multiple photons because of the intersubband transitions as the structure is periodic [14], which is compared with conventional laser, shown in Figure 2.5 (Right). The electron in conventional laser cannot play any further role after emission of a photon [15]. Theoretically, each free electrons in QCL which are in the high energy state is responsible to emit multiple photons due to the superlattice structure made of multiple

cascaded quantum wells [16],[17]. This increases the quantum efficiency in the QCL structure thus increases the output power.

A QCL consists of two main sections: the active region and the injector/extractor region. In the active region, electrons are initially pushed to a higher energy level. This process creates a situation called population inversion. When these electrons drop down to a lower energy level, they emit THz photons. Achieving population inversion can be done in various ways, and the most commonly used methods are discussed in Section 2.1.3. After emitting the THz photon, the electron moves to the extractor region, where it goes through resonant tunnelling. This allows the electron to pass into the adjacent QW, and the whole process repeats.

The materials used in mid-infrared lasers are not suitable for generating THz frequencies for several reasons. One key difference is that THz generation requires a much smaller energy gap, typically ranging from 4 to 25 millielectronvolts (meV), which is significantly smaller than what mid-IR lasers operate with. This small energy gap makes it challenging to introduce electrons into the right subbands to achieve population inversion because these subbands are very close together.

Furthermore, there is a risk of losing population inversion and, consequently, gain in THz QCLs due to two factors: thermal backfilling and thermally activated phonon scattering. Thermal backfilling occurs when an electron from the injector region of a QW is thermally excited back to the lower energy level of the previous QW, which disrupts the desired electron population distribution. Thermally activated phonon scattering happens when electrons possess enough kinetic energy to emit a longitudinal optic phonon instead of emitting a photon, again leading to a loss of gain [18].

Due to these complexities and challenges, THz QCLs are typically required to operate at very low temperatures, specifically cryogenic temperatures [18].

2.1.3 QCL active region

The QCL active region design is important as population inversion is achieved by proper growth of the active region. The important factors include wavefunction, energy level and rate of electron scattering from one subband to another [19]. Numerous QCL active regions have been demonstrated but these can be categorized into three main types.

2.1.3.1 Chirped Superlattice (CSL)

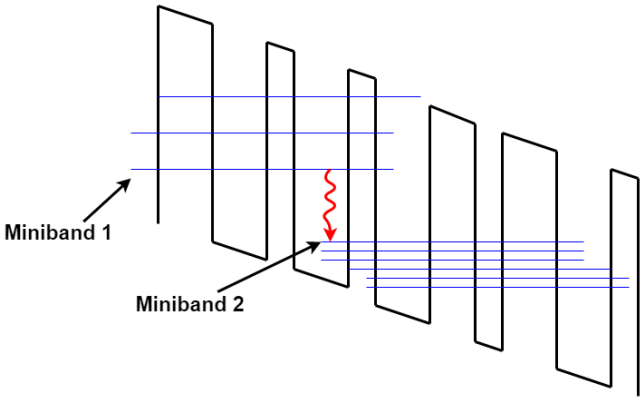

Figure 2.6: Chirped Superlattice

Numerous quantum wells are coupled to form a chirped superlattice having many minibands. These minibands are responsible for photon transition. As shown in Figure 2.6, there are two minibands having different energy gaps. These energy levels in the minibands can be adjusted by varying the barrier and the well thickness. When an electric field is applied on the QCL, the photon emission takes place between the lower energy level of the miniband 1 and upper energy level of the miniband 2 [18]. In this type, the population inversion can be achieved by electron elastic scattering between miniband 1 and miniband 2 [20]. This type of superlattice structure has less threshold current density but poorer population inversion [21].

2.1.3.2 Bound to continuum (BTC)

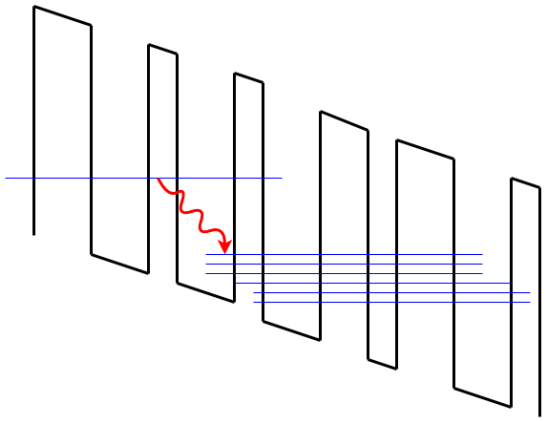

Figure 2.7: Bound to Continuum

The lower miniband of the BTC type is similar to the CSL but, the upper miniband in BTC contains a bound (isolated) state as shown in Figure 2.7. The main reason of formation of the bound state is because the thin quantum well is beside the injection barrier. By this, the photon emission takes place between the nearest state to the injection barrier and the lower miniband. This causes a diagonal transition which has many benefits compared to CSL type like the efficiency of injecting and the lasing period of the upper lasing level increases in BTC which provides a low thermal backfilling and better population inversion [21].

2.1.3.3 Resonant-phonon (RP)

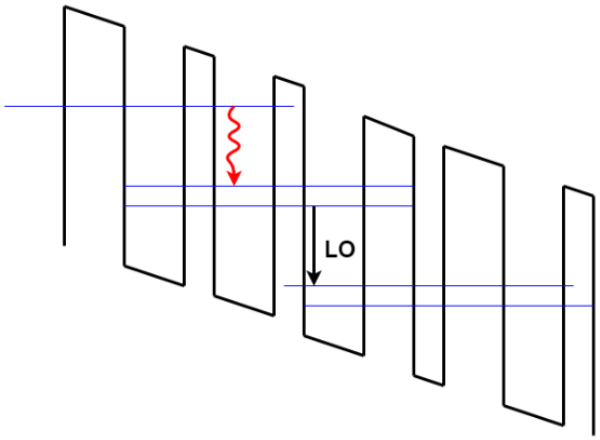

Figure 2.8: Resonant Phonon

In the resonant-phonon, the energy bandgap between the injector and the collector is chosen such that the electrons in the lower energy level are scattered quickly to the injector state [22]. This is due to a resonant condition, where electrons can lose energy, E_{LO}, and generate a longitudinal-optic phonon, as shown in Figure 2.8. This phonon energy varies from material to material, in GaAs, the E_{LO} should be 36 meV for resonant conditions. This provides faster extraction of electron from lower laser level and reduces thermal backfilling [23].

However, there are some limitations of using RP type active region design. These limitations are higher threshold current density and higher voltage for operating. This limitations can cause more thermal emission when working on high duty cycles [23].

2.1.4 THz waveguide design

Waveguides are used for better heat extraction and to get robust photon confinement in THz QCL. Ridge waveguides are used when fabricating an infrared or visible laser device, this is because the ridge waveguide have two facets which restrict the propagated light in two dimensions [24]. This confinement traps the light within the active region, leading to a build-up of photon density. In order to maintain effective waveguide confinement, the refractive index of the cladding layer is typically kept lower than the refractive index of the active region. This is because the difference in refractive indices creates a boundary that can confine the electromagnetic wave within the active region [18]. However, this approach does not work at THz frequency, as the wavelength is much larger than the QCL ridge thickness. Instead, plasmonic wvaeguides are used, in which the THz field is pinned against a conductive (metallic or highly doped) layer, as described in the following section.

The threshold gain (g_{th}) is determined by the confinement factor (Γ), mirror loss coefficient (a_m), and waveguide loss coefficient (a_w). The fraction of light lost at the mirrors and within the waveguide are represented by the mirror loss coefficient and waveguide loss coefficient respectively. The confinement factor measures the percentage of light that is confined within the active region [18].

$$g_{th} = a_w + \frac{a_m}{\Gamma} \tag{2.11}$$

To date, there are two types of waveguides used for fabricating THz QCLs. The semi-insulating surface plasmon (SI-SP) waveguides, and the metal-metal waveguides [18].

2.1.4.1 Semi Insulating Surface Plasmon (SI-SP) waveguides

The SI-SP waveguide structure as shown in Figure 2.9, represents how the THz mode is confined. The ridge (active region) made of thequantum well heterostructure which is sandwiched between a top metal layer and a thin lightly n^+ doped layer [25],[18]. Surface plasmon form at the interface between the QCL and the conductive layers. With this design of SI-SP, the absorption losses can be reduced and the optical mode can be tightly confined at longer wavelength [26]. Hence, the high optical power can be obtained in such design, but the minimum device area is limited due tightly confined optical mode results in a small confinement factor which reduces the temperature performance of the device [19], [24], [25]. SI-SP waveguide based 3.4 THz QCLs can produce maximum optical power up to 1.01 W at 10 K and can be operated up to 123 K [17].

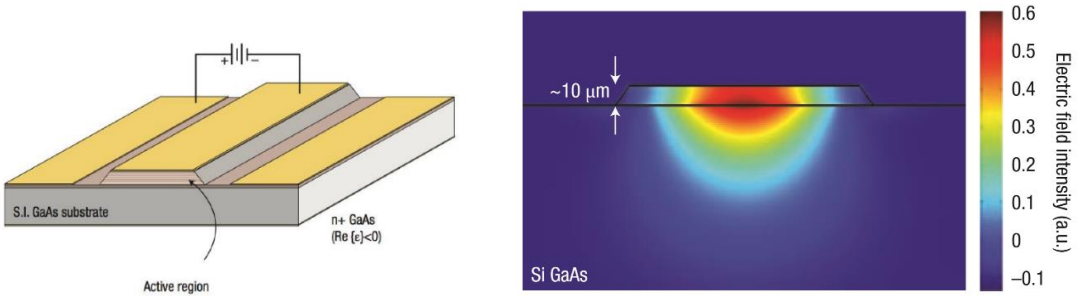

Figure 2.9: (Left) THz QCL SI-SP waveguide (adapted from [18]), (Right) Mode intensity pattern in SI-SP waveguide (adapted from [18])

2.1.5.2 Double metal or metal-metal (MM) waveguides

The structure of the double metal waveguide QCL device as shown in Figure 2.10, is similar to a waveguide of parallel plate. The confinement factor for such design is very high ($\Gamma \sim 1$) because the waveguide confines the mode within the active region [27]. This helps the structure to work at higher temperature > 250 K as the confinements is increased and gain threshold reduced by the second metallic layer [28]. However, due to very high confinement factor in double metal waveguides, the beam quality is very poor. Compared to SI-SP waveguide, MM waveguide QCL devices can out-couple maximum optical power up to few millwatts and have a highly divergent beam (because the aperture is smaller) [27].

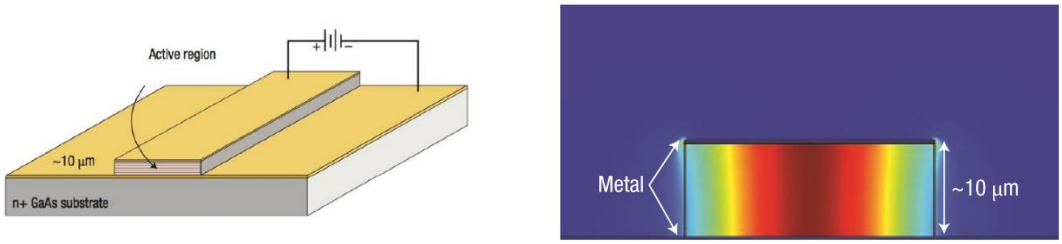

Figure 2.10: (Left) THz QCL MM waveguide (adapted from [18]) Mode intensity pattern in MM waveguide (adapted from [18])

2.2 QCL Characterisation

To support the KEYSTONE satellite mission, QCL devices emitting at 3.5 THz and 4.7 THz will serve as local oscillators in the KEYSTONE THz receiver. So, an approach was made to understand the fabrication of THz QCL. This section presents a systematic experimental comparison of two semi insulating surface plasmon (SI-SP) waveguide THz QCLs to provide emission frequencies of ~ 5 THz and ~ 3 THz. The aim of this study was to understand the performance of SI-SP waveguide THz QCLs and compare with the requirements of local oscillator (LO) in KEYSTONE satellite

mission. The study of LIV curve at different heat-sink operating temperature and spectra measurements at different currents are highlighted.

The QCL devices mentioned in this section are “Device A” and “Device B” (full description of devices used in the thesis is outlined in the appendix Table B). The “Device A” and “Device B” were fabricated using the identical method outlined in the appendix, using a combination of photolithographic and wet chemical etching steps.

After the fabrication process, the performance of these devices was determined using the LIV characterisation. Factors such as the device output power, threshold current, and voltage as a function of drive current can be provided by LIV characterisation. The maximum output power (P_{max}) is a crucial parameter that determines the ability of the QCL to deliver high-power THz radiation for applications. The threshold current (I_{th}), at an operating voltage (V_{th}), is the minimum current required for the device to start lasing. The thermal behaviour of QCL is another important factor that affects their performance. QCL produce a substantial amount of heat throughout the operation, which degrades the output power performance at high temperatures.

2.3.1 Experimental set-up for the LIV characteristics

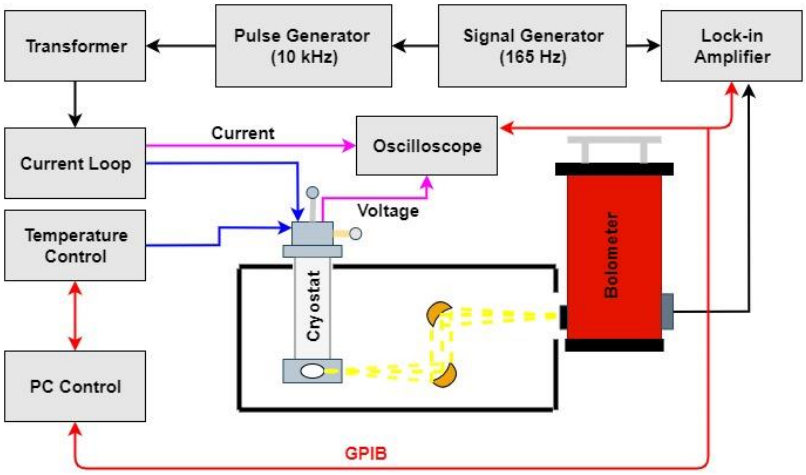

Figure 2.11: Schematic diagram of experimental set-up for the LIV characteristics

As shown in the Figure 2.11, the block diagram explains the set-up for measuring the LIV characteristics of the QCL device. After mounting the QCL on the cold finger of a Janis ST-100 continuous flow cryostat (shown in Figure 2.12), a turbo vacuum pump was used to pump down to a vacuum pressure of ~8×10^{-6} mbar in order to provide thermal insulation, shown in Figure 2.13. The temperature of the cryostat is then lowered to ~10 K by pumping liquid helium in the cryostat and its operating temperature was regulated by a temperature controller connected to a heater.

Figure 2.12: Photograph of QCL mounting block attached to the cold-finger of a helium-cooled optical Janis cryostat

Figure 2.13: Photograph of cryostat connected to turbo vacuum pump with continuous liquid helium flow through liquid helium cryogenic storage dewar. The instrument in red is the (He) cooled QMC QSIB/3 bolometer.

The signal generator was used to generate modulation frequency of 165 Hz which is connected to the pulse generator and lock in amplifier for matching the responsivity of the bolometer detector. A current pulse train was produced by a pulse generator at 10 kHz repetition rate and duty cycle of 2%. It was electrically using the 165 Hz modulation input and used to drive the QCL via a current probe and transformer. The operating current and voltage of the QCL is measured by connecting the current loop of the cryostat sense port to the oscilloscope. The THz radiation generated by QCL is detected on the (He) cooled QMC QSIB/3 bolometer (shown in Figure 2.13) using a gold plated parabolic mirror to focus the beam. This is done in the presence of the nitrogen gas in a Perspex chamber to minimise the absorption of THz radiation by water vapour. The THz signal is then recovered using a 7225 DSP lock-in amplifier. A National Instruments LabVIEW instrument panel is used to record the LIV curves and raw data by interfacing the temperature control, lock-in amplifier and oscilloscope to the PC through GPIB connection. The values of current, voltage and power are reproduced in MATLAB and Origin Pro to plot the LIV curves.

2.3.2 Experimental set-up for the spectra characteristics

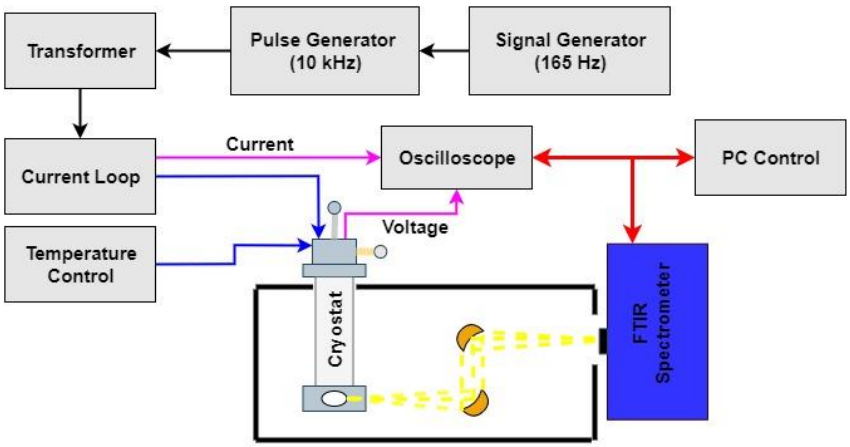

Figure 2.14: Schematic diagram of experimental set-up for the spectra measurements

The spectral characteristics are used to analyse the device's behaviour as a single-mode or multi-mode emission. Depending on the device design and fabrication process, QCLs can have a narrowband or wideband spectrum.

Narrowband spectrums are ideal for high-resolution spectroscopy because they provide fine spectral detail. They are also used in sensing applications such as gas spectroscopy, where narrowband spectra enhance the selectivity and sensitivity of measurements, enabling the detection of trace amounts of specific substances by isolating their absorption or emission lines.

Conversely, in free-space optical communication, wideband spectrums are preferred because they can carry more information over a given bandwidth. Moreover, wideband sources help capture a wide range of colours or spectral signatures simultaneously, therefore used in imaging applications. [17].

The spectra characterisation setup is similar to the LIV characterisation setup as discussed in the previous section. The key distinction lies in the utilization of an FTIR instrument (Bruker IFS/66) for spectrum measurement, where spectra scans are conducted across various driving currents while maintaining a constant temperature, as depicted in Figure 2.14. Spectrometer control software (OPUS) is used for measuring and recording the spectral characteristics.

2.3.3 QCL device characterisation results

2.3.3.1 Device A

The “Device A” was fabricated with dimensions of 2 mm length and 150 µm ridge width. Optical lithography was used for defining the laser ridges and ohmic contacts. The thicknesses of the Au/Ge/Ni bottom and top contacts were ~ 200 µm and ~ 100 µm respectively, and the thickness of the Ti/Au over-layer was 100-150 nm.

The experiment was conducted in pulse mode operation at different heat sink temperature to examine the LIV performance of the device as shown in Figure 2.15. The device threshold current was observed to be ~1.7 A where it start lasing. The maximum optical output power of the device that has been obtained at temperature 4 K was ~ 81 µW with peak current of ~3.8 A. An exponential decrease of the optical output power as a function of the heat sink has been observed, as shown in Figure 2.16. This device worked at temperature up to 65 K with optical output power of ~ 19.6 µW.

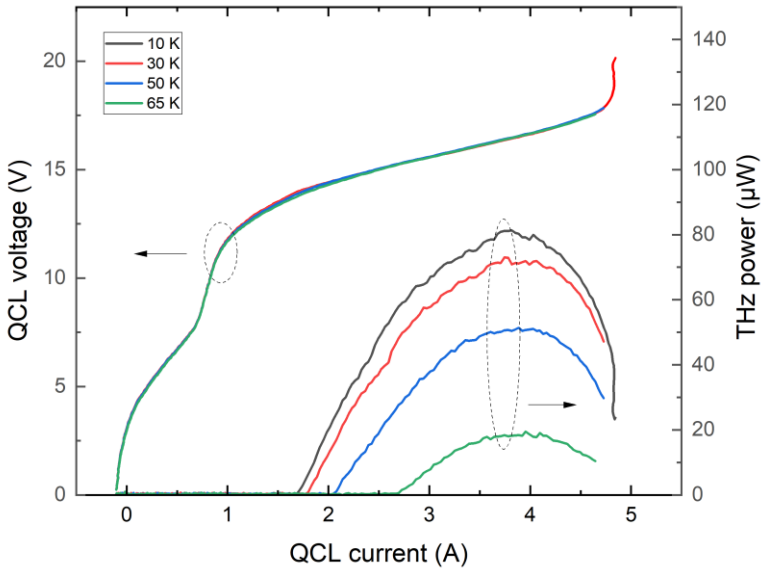

Figure 2.15: LIV characteristics of "Device A"

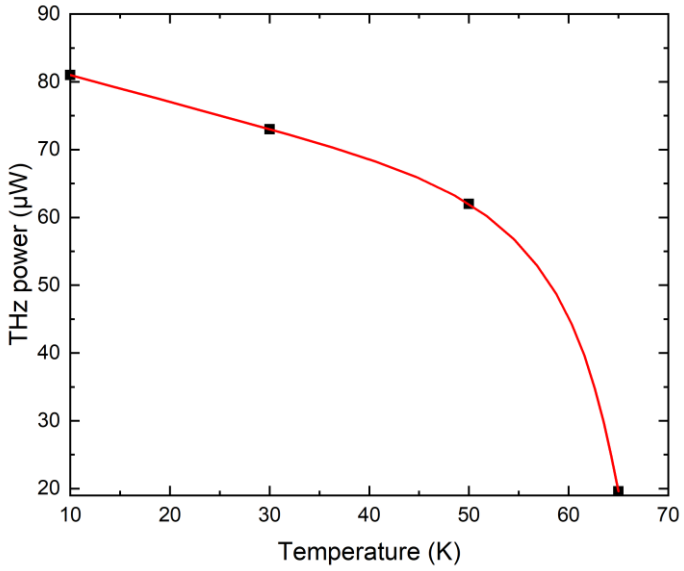

Figure 2.16: Optical output power as a function of heat-sink temperature for "Device A"

The spectral measurement of the device has been obtained at nine different drive currents starting above the threshold current and end below the rollover current as shown in Figure 2.17. The results recorded with fixed heat sink temperature at 10 K shows multi-mode emission with central frequency at 4.954 THz. The multi-mode emission was observed between 4.7 and 5.1 THz. At higher current value the ~4.8 THz mode disappears.

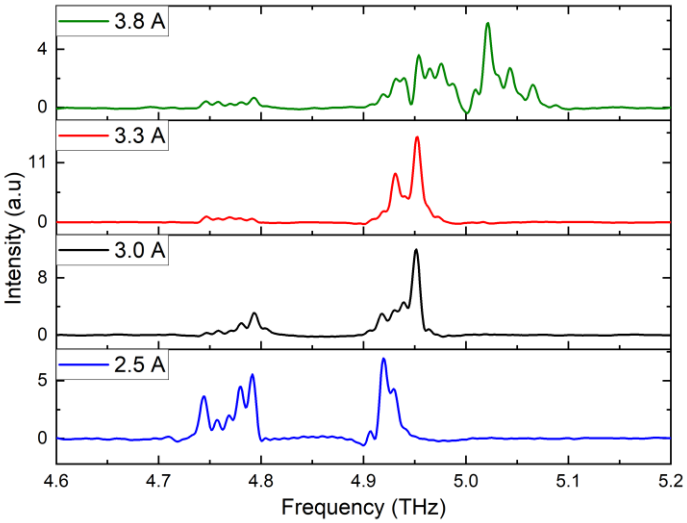

Figure 2.17: Spectra measurements of “Device A”, at four different drive currents at 10 K heat-sink temperature.

2.3.3.2 Device B

The “Device B” was fabricated with a similar recipe as for the “Device A”. The LIV performance of the “Device B” are shown in Figure 2.18. The device threshold current was observed to be ~ 0.4 A where it start lasing. The maximum optical output power of the device that has been obtained at temperature 6 K was ~ 38.8 µW with peak current of ~ 1 A. Figure 2.19 shows a decrease of the maximum power of the device as function of temperature. This device worked at temperature up to 101 K with optical output power of ~ 1.1 µW.

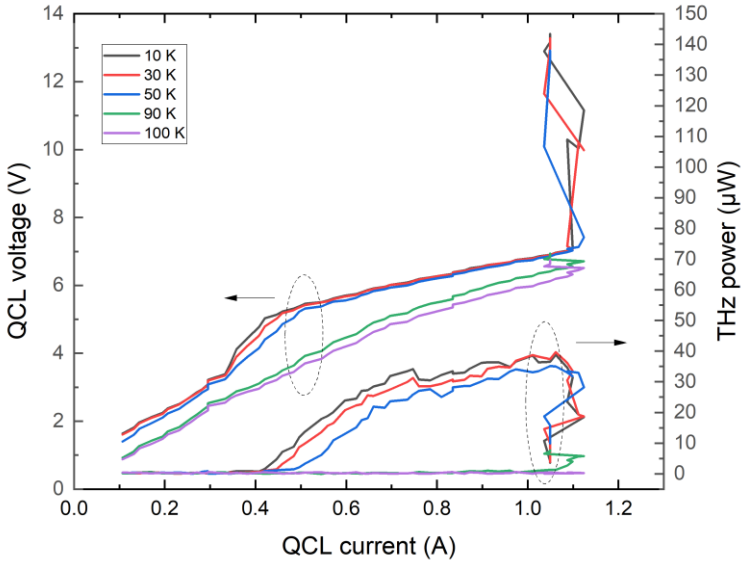

Figure 2.18: LIV characteristics of “Device B”

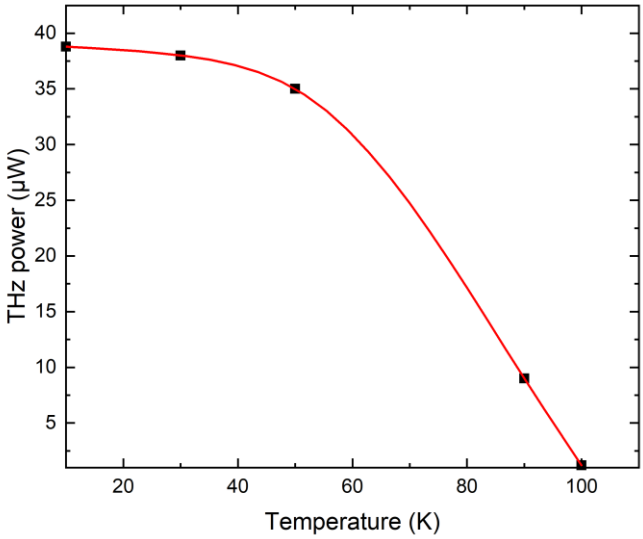

Figure 2.19: Optical output power as a function of heat-sink temperature for “Device B”

The spectral measurements of the “Device B” have been obtained at two different drive currents as shown in Figure 2.20. The results recorded and measured with fixed heat sink temperature at 10 K shows multi-mode emission with central frequency at 2.941 THz. The multi-mode emission was observed between 2.8 and 3.13 THz.

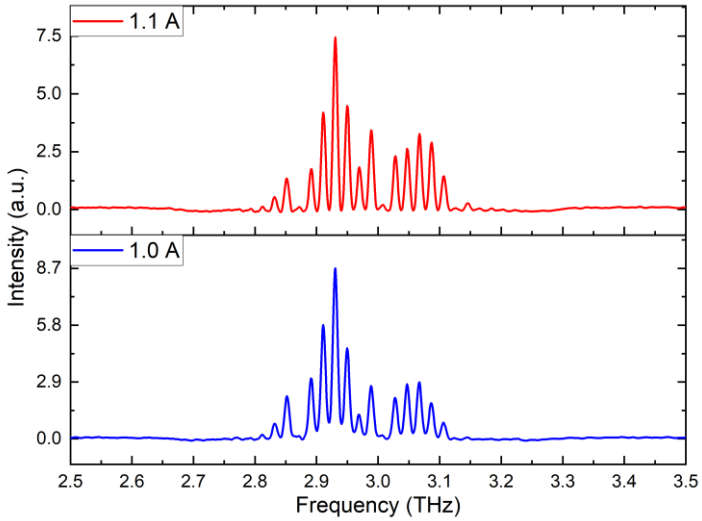

Figure 2.20: Spectra measurements of "Device B", at two different drive currents at 10 K heat-sink temperature.

It is important to note that these spectral measurements are for simple ridge waveguide. The emission frequency can be tailored using photonic grating structures to any single mode within the laser gain-bandwidth.

2.3.3 Variation in LIV performance with heat-sink temperature

As the heat-sink temperature increases, thermal back-filling within the device becomes more common, leading to a reduction in the optical output power. Consequently, the device becomes unable to lase effectively at higher temperatures [29].

The QCL devices (Device A & B) based on SI-SP waveguide technology has demonstrated high optical output power. However, the temperature performance of the devices was compromised because of poor optical confinement in the SI-SP waveguide structure.

The KEYSTONE satellite mission necessitates the utilization of QCL devices that can operate in continuous-wave mode within a temperature range of 50K to 100K. These QCL devices must exhibit frequency and power stabilisation and should generate more than 10 mW of optical power.

Furthermore, these devices should be designed for robust integration, offering protection against physical contact and shielding from ionizing radiation exposure. Chapters 3, 4, and 5 of the thesis will give a detailed discussion on progress made towards developing such QCL devices (Note that, different QCL devices are used in Chapters 3, 4, and 5, these are outlined in the appendix Table B), which are intended for use as Local Oscillators (LO) in the KEYSTONE front-end receiver.

The thermal performance could be improved in several ways; increasing the length of the laser cavities which could enhance its maximum optical output power, primarily because a larger gain medium can provide a higher net gain. However, QCL output power will eventually saturate at high device length due to the influence of heating effects. The temperature of the active region rises as the device length increases [30].

Moreover the power consumption for “Device A” was 56 W which was extremely high, which eventually degrades its temperature performance.

2.4 Conclusions

In conclusion, this chapter has provided a comprehensive overview of the fundamental concepts crucial for understanding QCLs, with a particular focus on Terahertz (THz) QCL devices emitting at approximately 3 THz and 5 THz. The chapter began by providing a detailed explanation on the role of heterostructures and quantum confinement, emphasizing the influence of the behaviour of electrons within quantum wells. It also focuses on the essential principles governing QCL operation and highlights key components within QCLs, including active regions and laser waveguides.

Moreover, the chapter discussed the fabrication and characterization of THz QCL devices, covering various analyses such as LIV measurements at different heat-sink temperatures, spectral analysis, and an evaluation of device performance for potential KEYSTONE satellite applications.

2.5 Bibliography

[1] ‘Lim, C.T., 2017. Nanofiber technology: current status and emerging developments. Progress in Polymer Science, 70, pp.1-17.’.

[2] W. R. Frensley, ‘Chapter 1 - Heterostructure and Quantum Well Physics’, in VLSI Electronics Microstructure Science, vol. 24, N. G. Einspruch and W. R. Frensley, Eds., in Heterostructures and Quantum Devices, vol. 24. , Elsevier, 1994, pp. 1–24. doi: 10.1016/B978-0-12-234124-3.50006-9.

[3] ‘Quantum Wells, Wires and Dots: Theoretical and Computational Physics of Semiconductor Nanostructures, 4th Edition | Wiley’, Wiley.com. Accessed: Mar. 20, 2023.

[4] A. David and B. Miller, ‘Optical physics of quantum wells’, in Quantum Dynamics of Simple Systems, 1st ed., G.-L. Oppo, S. M. Barnett, E. Riis, and M. Wilkinson, Eds., CRC Press, 2020, pp. 239–266. doi: 10.1201/9781003072973-9.

[5] H. Sakaki, M. Tsuchiya, and J. Yoshino, ‘Energy levels and electron wave functions in semiconductor quantum wells having superlattice alloylike material (0.9 nm GaAs/0.9 nm AlGaAs) as barrier layers’, Appl. Phys. Lett., vol. 47, no. 3, pp. 295–297, Aug. 1985, doi: 10.1063/1.96197.

[6] E. Nelson, ‘Derivation of the Schrodinger Equation from Newtonian Mechanics’, Phys. Rev., vol. 150, no. 4, pp. 1079–1085, Oct. 1966, doi: 10.1103/PhysRev.150.1079.

[7] N. Moiseyev, M. Chrysos, and R. Lefebvre, ‘The solution of the time-dependent Schrodinger equation by the method: application to intense field molecular photodissociation’, J. Phys. B At. Mol. Opt. Phys., vol. 28, no. 13, pp. 2599–2609, 1995.

[8] H. H. Erbil, ‘A Simple Solution of the Time-Independent Schrodinger Equation in One Dimension’. arXiv, May 26, 2003. doi: 10.48550/arXiv.quant-ph/0305158.

[9] R. K. Kawakami et al., ‘Quantum-well states in copper thin films’, Nature, vol. 398, pp. 132–134, Mar. 1999, doi: 10.1038/18178.

[10] G. Bastard, ‘Wave mechanics applied to semiconductor heterostructures’, Jan. 1990, Accessed: Mar. 20, 2023.

[11] ‘Possibility of the amplification of electromagnetic waves in a semiconductor with a superlattice | BibSonomy’. Accessed: Mar. 20, 2023.

[12] J. Faist et al., ‘High power mid-infrared (λ∼5 μm) quantum cascade lasers operating above room temperature’, Appl. Phys. Lett., vol. 68, no. 26, pp. 3680–3682, Jun. 1996, doi: 10.1063/1.115741.

[13] B. G. Lee et al., ‘DFB Quantum Cascade Laser Arrays’, IEEE J. Quantum Electron., vol. 45, no. 5, pp. 554–565, May 2009, doi: 10.1109/JQE.2009.2013175.

[14] D. Vaitiekus, ‘Development of Quantum Cascade Lasers for Gas Sensing Applications’.

[15] S. L. Chuang, ‘Physics of Photonic Devices, 2nd Edition’.

[16] M. Razeghi, ‘Quantum Cascade Lasers’, in Technology of Quantum Devices, M. Razeghi, Ed., Boston, MA: Springer US, 2010, pp. 271–319. doi: 10.1007/978-1-4419-1056-1_7.

[17] J. Faist, F. Capasso, D. L. Sivco, C. Sirtori, A. L. Hutchinson, and A. Y. Cho, ‘Quantum cascade laser’, Science, vol. 264, no. 5158, pp. 553–556, Apr. 1994, doi: 10.1126/science.264.5158.553.

[18] B. S. Williams, ‘Terahertz quantum-cascade lasers’, Nat. Photonics, vol. 1, no. 9, Art. no. 9, Sep. 2007, doi: 10.1038/nphoton.2007.166.

[19] L. Li et al., ‘Terahertz quantum cascade lasers with >1 W output powers’, Electron. Lett., vol. 50, no. 4, pp. 309–311, 2014, doi: 10.1049/el.2013.4035.

[20] H. Luo, S. R. Laframboise, Z. R. Wasilewski, G. C. Aers, H. C. Liu, and J. C. Cao, ‘Terahertz quantum-cascade lasers based on a three-well active module’, Appl. Phys. Lett., vol. 90, no. 4, p. 041112, Jan. 2007, doi: 10.1063/1.2437071.

[21] C. A. Evans, ‘The optical and thermal properties of quantum cascade lasers’.

[22] Q. Hu, B. S. Williams, S. Kumar, H. Callebaut, and J. L. Reno, ‘Terahertz quantum cascade lasers based on resonant phonon scattering for depopulation’, Philos. Transact. A Math. Phys. Eng. Sci., vol. 362, no. 1815, pp. 233–247; discussion 247-249, Feb. 2004, doi: 10.1098/rsta.2003.1314.

[23] ‘3.4-THz quantum cascade laser based on longitudinal-optical-phonon scattering for depopulation: Applied Physics Letters: Vol 82, No 7’.

[24] D. M. Mittleman, R. H. Jacobsen, R. Neelamani, R. G. Baraniuk, and M. C. Nuss, ‘Gas sensing using terahertz time-domain spectroscopy’, Appl. Phys. B, vol. 67, no. 3, pp. 379–390, Sep. 1998, doi: 10.1007/s003400050520.

[25] S. Kumar, ‘Recent Progress in Terahertz Quantum Cascade Lasers’, IEEE J. Sel. Top. Quantum Electron., vol. 17, no. 1, pp. 38–47, Jan. 2011, doi: 10.1109/JSTQE.2010.2049735.

[26] R. Köhler et al., ‘Terahertz semiconductor-heterostructure laser’, Nature, vol. 417, no. 6885, pp. 156–159, May 2002, doi: 10.1038/417156a.

[27] M. Brandstetter et al., ‘High-power THz quantum cascade lasers’, presented at the Proceedings of the 2015 High Power Diode Lasers & Systems Conference (HPD), IEEE, 2015, pp. 5–6. Accessed: Mar. 20, 2023.

[28] ‘High-power and high-temperature THz quantum-cascade lasers based on lens-coupled metal-metal waveguides’. Accessed: Mar. 20, 2023.

[29] S. Kohen, B. S. Williams, and Q. Hu, ‘Electromagnetic modeling of terahertz quantum cascade laser waveguides and resonators’, J. Appl. Phys., vol. 97, no. 5, p. 053106, Mar. 2005, doi: 10.1063/1.1855394.

Chapter 3
Terahertz quantum cascade lasers power locking

3.1 Overview

The work undertaken in this chapter aims to advance THz local oscillators for the proposed KEYSTONE satellite [1]. THz output power from a QCL is susceptible to temperature fluctuations and optical feedback. Atmospheric absorption and mechanical vibrations (e.g., from cryocoolers) also introduce fluctuations in the out coupled power, causing significant drifts in system performance. It is, therefore, desirable to provide active power stabilization.

Numerous QCL power stabilization techniques have been developed, including the use of a swing-arm voice coil actuator as a variable beam-block [2], a graphene-loaded split-ring-resonator array as an external amplitude modulator [3], or illumination with an external diode laser to perturb QCL emission [4]. All these techniques, however, rely on external optical elements, which increase system size and complexity.

This chapter reports the power modulation and locking of THz QCLs using a simple photonic integrated circuit formed by coupling a racetrack resonator (RTR) with a QCL ridge waveguide using a co-directional coupler. By varying the electrical bias on the RTR, the optical modes of the RTR can be brought in and out of resonance with the QCL. Therefore, the THz field can effectively be confined within the ring, resulting in the THz output power modulation.

3.2 Review of previous technique

3.2.1 Swing-arm voice coil actuator

The setup used for power stabilization of QCL by swing-arm voice actuator is illustrated in Figure 3.1. The THz radiation from the QCL passes through a voice coil actuator, and then the signal is directed to a HEB (Hot-electron bolometer) mixer for detection. The HEB mixer is a type of fast superconducting device that is sensitive to THz radiation [2].

The voice coil actuator is used in conjunction with a PID feedback loop to stabilise the amplitude of the Local Oscillator (LO). The voice coil actuator is a variable optical attenuator used to disrupt a part of the LO beam in order to control the LO power and maintain the HEB mixer's DC current constant. The PID feedback loop is intended to regulate the voice coil actuator in response to variations in the HEB mixer's DC current, which serves as a reference signal for the required LO power [2].

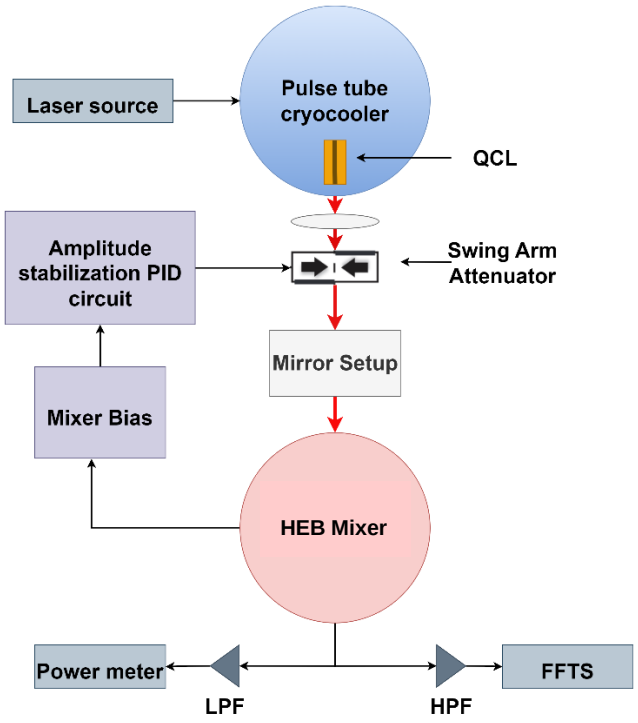

Figure 3.1: Schematic of the measurement setup for demonstrating amplitude stabilization using swing arm voice coil actuator (adapted [2]).

The usage of a voice coil actuator for amplitude stabilisation provides numerous advantages over other amplitude stabilisation approaches such as a rotating polarizer. The voice coil actuator is fast and can respond at up to 1 kHz, which is essential for maintaining stability in the context of rapid LO power variations. Furthermore, the voice coil actuator has a high resolution and a wide dynamic range, allowing for accurate LO power shifts. This approach can contribute to minimise not only LO amplitude fluctuation, but also other variables such as atmospheric turbulence along the LO channel and LO mechanical destabilisation [2]. However, there are few limitations to this approach of power locking which includes its slow response time and the requirement for a sizable and fragile setup. The system also potentially introduces knife-edge diffraction, reducing beam quality.

3.2.2 Graphene-loaded split-ring-resonator array as an external amplitude modulator

Active amplitude modulators are often required to accomplish amplitude stability for a specific frequency range. Graphene loaded metamaterial arrays offer a promising solution due to their high modulation depth and speed [5], as well as ease of implementation [6]. Metamaterials can confine electromagnetic radiation at a certain frequency [7], and the electrical conductivity of graphene can be tuned substantially by varying the carrier concentration [8]. This combination allows for effective tunable reflectivity within a specific frequency band. Many THz modulators based on graphene loaded metamaterials have been developed [3], including split ring resonators that operate with ultra-low bias [9],[10], achieving 100% modulation depths when associated with a THz QCL [10].

Arrays of hybrid metamaterials graphene split ring resonators (SRR) are used in the modulator. The hybrid graphene-SRR modulator is placed externally to the cryostat, as shown in Figure 3.2. A PID loop controller was used to dynamically modify the gate voltage of the SRR and compensate for QCL power fluctuation. The controller regulates the voltage provided to the SRR to ensuring the stable output power of the laser. This is accomplished by monitoring the laser's output power and comparing it

to a specified set point value, and then adjusting the voltage provided to the SRR with the PID controller to maintain the desired output power [3].

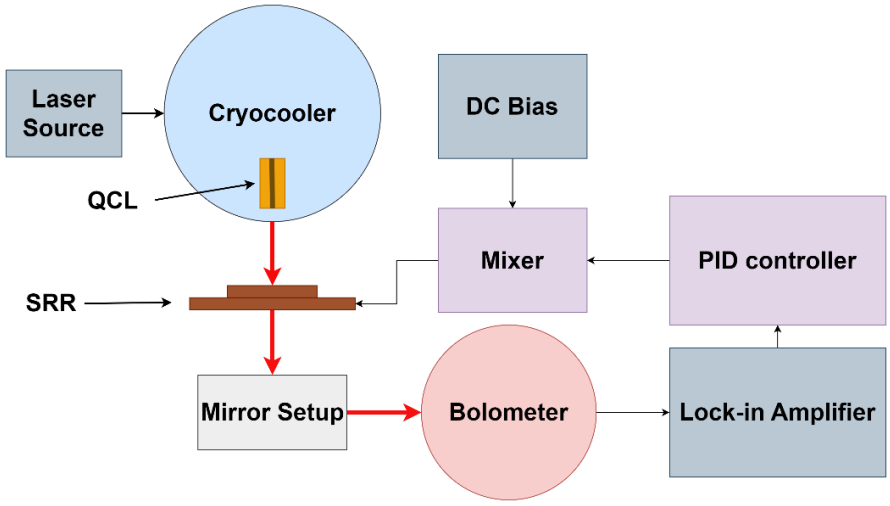

Figure 3.2: Schematic of the set-up for amplitude stabilization using graphene-loaded split-ring-resonator (adapted [3]).

A liquid-He cooled Si-bolometer was used to measure the output power of the THz QCL after it passed through the hybrid metamaterial/graphene SRR modulator. The bolometer signal is initially extracted by a lock-in amplifier at a certain reference frequency, which is also the gate frequency delivered to the QCL. The signal is then passed to the PID controller, which provides a DC output when the bolometer signal deviates from a set point. This set point can be changed to define the laser's desired power after transmission through the SRR device. This DC output is applied to the back gate of the SRR device in order to control its transmission characteristics and compensate for changes in laser power. This enabled accurate and precise regulation of the THz QCL's output power, proving the efficacy of the hybrid metamaterial/graphene SRR modulator and PID loop controller in accomplishing amplitude stability [3].

The PID loop controller and SRR modulator have a limited bandwidth, which means they can only compensate for variations in laser output up to a particular frequency. The fluctuations cannot be controlled above this frequency, resulting in residual amplitude fluctuations [3]. Furthermore, these power locking systems tend to

be bulky and rely on external means to achieve power modulation. However, the response time of such modulation scheme is much faster that the voice coil actuator.

3.2.3 NIR diode laser to perturb QCL emission

An alternative approach is to use a near-infrared (NIR) diode laser excitation to the QCL's rear facet, with the illumination directly coupled through an optical fibre. This provides a QCL separate control parameter from drive current to achieve amplitude stability in a system with a PID feedback loop [4]. The feedback loop varies the diode laser driving current based on the signal from a Ge:Ga detector, which also serves as a reference for the QCL power level, illustrated in Figure 3.3. Such system can achieve stability without the need for an external THz modulator.

One advantage of this setup is that it is relatively compact and robust. This is due to the direct coupling of the illumination through an optical fibre, which eliminates the need for an external THz optical modulator to regulate the frequency and output power. This makes the setup simpler and easier to use, and potentially more cost-effective than alternative setups that require additional equipment [4].

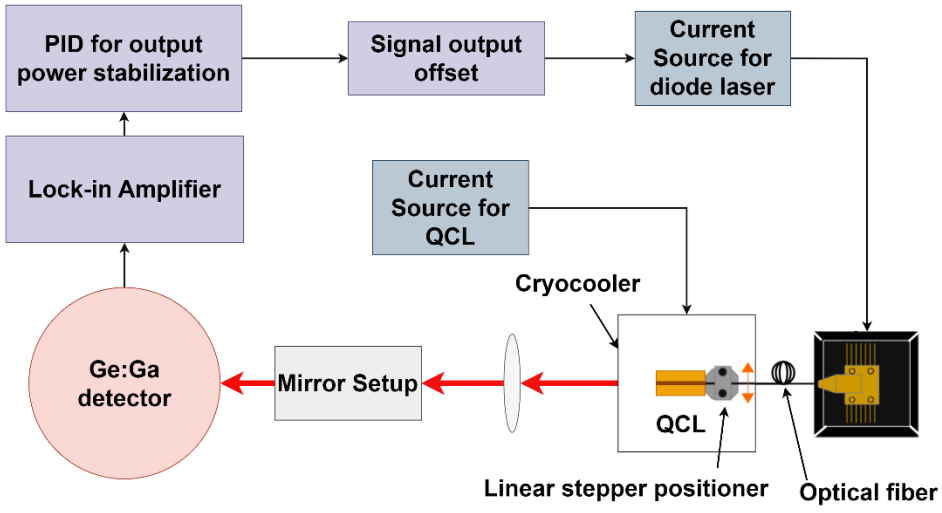

Figure 3.3: The schematic diagram of the setup used to stabilize the output power using NIR diode laser (adapted [4]).

Overall, the described technique appears to be a promising way to achieve stable performance in a QCL-based system. However, as with any control system, there may be limitations or trade-offs to consider, such as the response time of the feedback loops and their impact on the overall system performance. Further experimentation and analysis may be necessary to fully understand these factors and optimize the system accordingly [4]. However, this system requires an external diode laser modulation, resulting in increased system size and complexity.

3.3 THz QCL - Race Track Resonator

3.3.1 Simulation and design

The University of Leeds approach to THz generation and modulation involves using a racetrack resonator (RTR) design coupled to a quantum cascade laser (QCL). The THz RTR-QCL device discussed in this chapter is “Device C”, which is outlined in appendix Table B. The RTR is a component often used in silicon photonics and telecom lasers [11]. The optical modes of the RTR can be brought in and out of resonance with the QCL by varying the resonator electrically. This resonator ring is kept below the threshold, introducing an optical loss. This effectively traps the THz field inside the ring and contributes to modulating the THz output power. Figure 3.4 depicts a schematic of how the RTR and QCL connection are set up [12].

QCLs have low refractive index tuning rates, requiring larger electroabsorption modulator (EAM) and Mach-Zehnder interferometer (MZI) structures. As such, a different approach is needed at the THz frequencies. Here, the radiation from the QCL cavity is coupled into an RTR structure in the RTR-QCL technique, and the effective optical length of the RTR can be controlled simply using the applied voltage. This voltage-controlled tuning allows for the adjustment of the phase matching of the coupled radiation, enabling efficient THz generation and modulation.

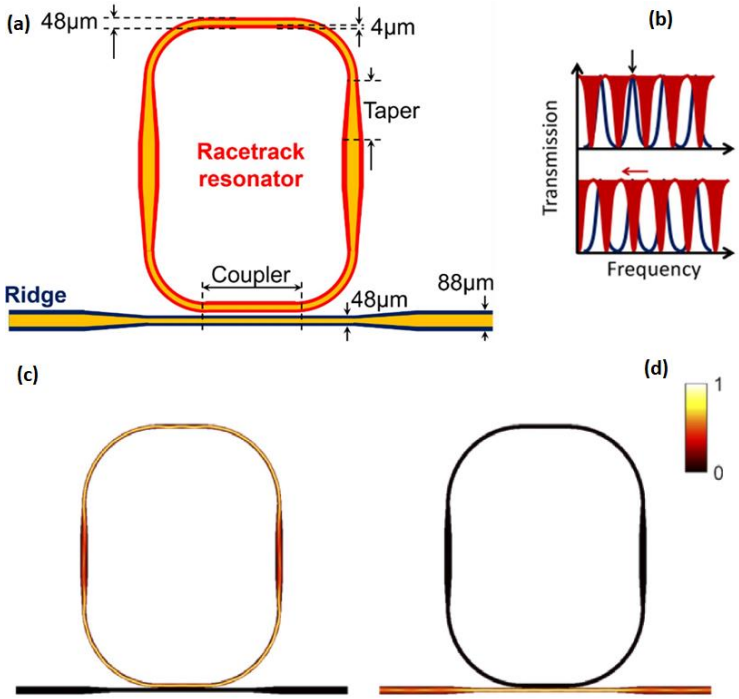

Figure 3.4: (a) QCL+modulator device ("Device C") concept, in which the Mach–Zehnder scheme is adapted into a "racetrack resonator" structure. (b) Stark shift occurring at RTR. Finite element modelling of power distribution across the "Device C", when (c) electric field is almost fully confined in the RTR; (d) electric field is almost fully transmitted through the ridge. (adapted from [12]).

Figure 3.4 (a) shows a narrow ridge section (blue outline) coupled to an RTR section (red outline) through a 48 μm wide coupler section. A wider cavity of 88 μm is used for wire bonding and is connected to the narrow waveguide through a 350 μm long taper section. To prevent higher-order transverse modes, a 4 μm wide absorber is used. The transmission properties of the coupled-RTR device are managed by adjusting the lengths of the ridge, coupler, air gap, and RTR arc radius. These lengths are set at 4 mm, 565 μm, 3 μm, and 893.52 μm, respectively [12].

An RTR is connected longitudinally to a ridge laser using the evanescent field, resulting in the formation of a comb of stop band frequencies, shown as red bands in Figure 3.4 (b). The lengths of the cavity sections are precisely selected so that the free spectral range (FSR) of the ridge laser almost matches the frequency spacing between consecutive resonances within the RTR. When the stop bands of the combs formed by

the RTR experience a shift, it leads to the suppression of longitudinal modes and a decrease in the output power [12]. In simulations, a frequency comb comprised of band-stop filters was generated, shown in Figure 3.4 (a). The electric field was largely contained within the RTR, with minimal transmission through the ridge, shown in Figure 3.4 (c). When the electric field intensity across the RTR was increased, it caused a red-shift in the comb of stop band frequencies due to alterations in the refractive index. When decreasing the electric field across the RTR, the fully transmitted power distribution through the ridge was shown in Figure 3.4 (d) [12].

An advantage of this approach is that the QCL achieves refractive index tuning twice as fast compared to NIR diode laser.

3.3.2 Mask development

“Device C” structure fabrication can typically be accomplished by using a photolithographic technique. This technique has a drawback in that it requires a unique mask set for each design iteration, making the design process time-consuming. To solve this, we have switched to a maskless alignment technology that uses a laser to directly write the photolithographic pattern, allowing for quicker design iteration. This approach only requires a CAD pattern as the "mask". Figure 3.5 depicts a three-dimensional representation of the “Device C” structure that is created using this novel maskless alignment technique.

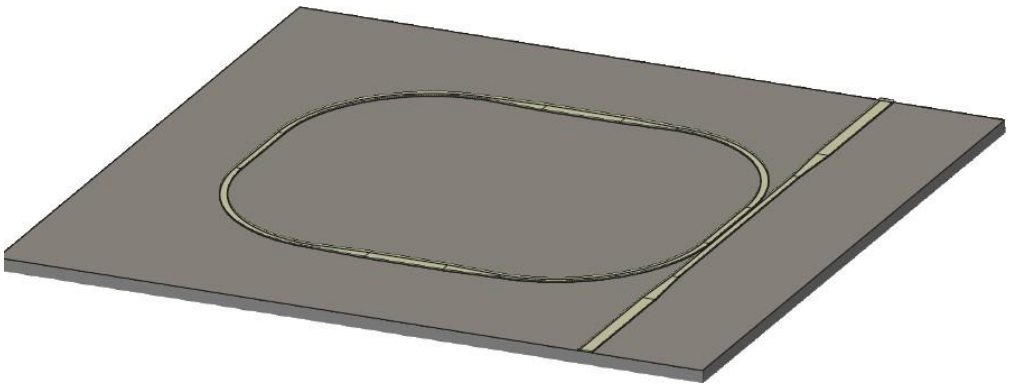

Figure 3.5: CAD rendering of the “Device C” mask design.

3.3.3 Modulator fabrication

The following crucial steps were involved in the fabrication of the “Device C”:

Wafer-bonding of the QCL to a carrier substrate: The QCL is bonded to a carrier substrate to offer the device mechanical stability throughout the process.

Mask-less aligner to pattern the structure: The device structure is patterned without the need of a photomask using a mask less aligner. This reduces the fabrication process and lowers the cost while enabling precise control over the device dimensions.

Dry reactive etching process: The device structure is etched to produce well-defined ridges with vertical sidewalls that offers high selectivity and anisotropic etching.

Focused ion beam used as an etching process: A focused ion beam (FIB), which permits high-precision etching of microscopic features, is utilised to etch the narrow air gap between the QCL ridge and modulator.

Metallisation of the ridge: The ridge is metalized to give the QCL an electrical connection, allowing current to be injected to produce THz radiation.

Device substrate thinning: Thinning of device substrate is done to lower thermal resistance and improve heat dissipation from the device.

The measured air gap between the QCL ridge and resonator was marginally larger (2.54-μm wide) than the design expected value (2.5-μm wide), but still within an acceptable range for the device to function as intended, shown in Figure 3.6.

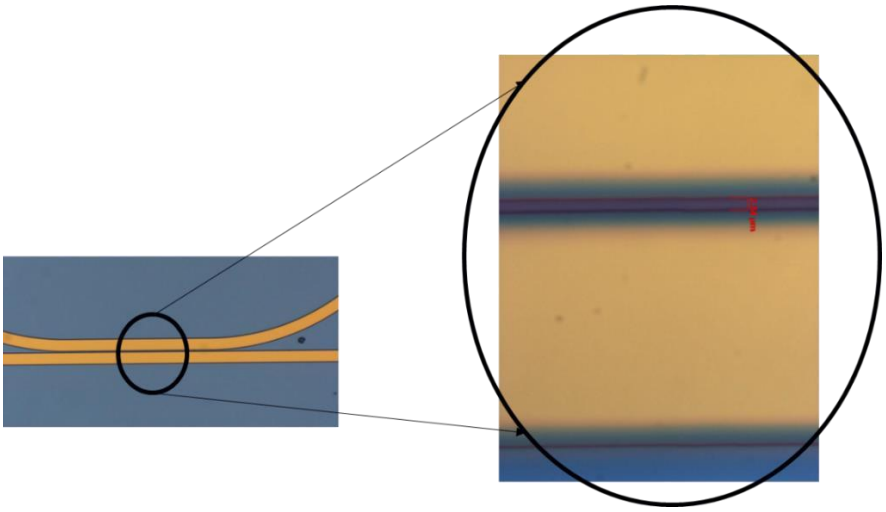

Figure 3.6: “Device C”, as fabricated. Microscopy images shown of the coupler region between the QCL and resonator.

In the processing of the "Device C", the GaAs-etch process was stopped immediately upon the observation of the reflective Au layer. This was done to avoid Au sputtering onto the device's sidewalls, which may result in an electrical short. However, as can be seen in Figure 3.7, this resulted in a minor under-etch near to the ridge. To address this issue, the device underwent a UV/oxygen etch which removes the residual photoresist. This step assists in ensuring any contamination or debris that can affect the device's performance has been removed.

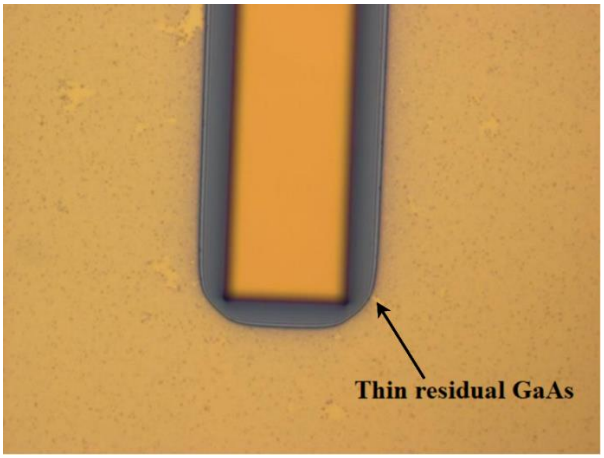

Figure 3.7: Photograph showing thin residual GaAs layer around the edge of the ridge.

The effective coupling of THz radiation from the device into a waveguide or free space requires a well-defined end-facet, as illustrated in Figure 3.8. It also helps to limit light reflection back into the device, which could reduce its efficiency.

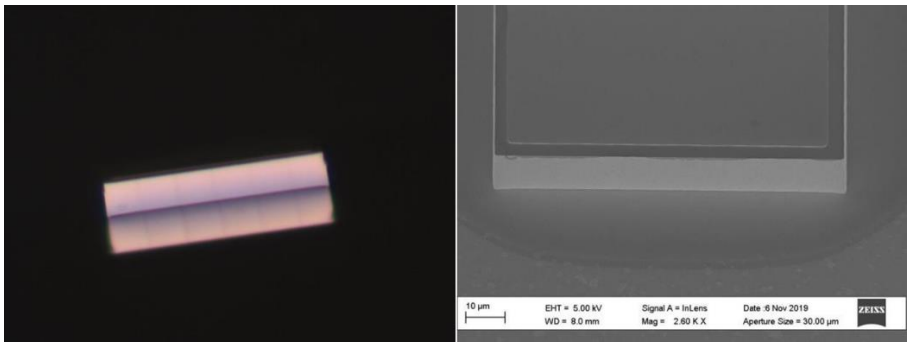

Figure 3.8: (left) Optical 50× view (and its reflection), and (right) SEM image of the end-facet.

It was possible to check the quality of the etch between the ridge and the ring resonator by etching a similar pattern on a GaAs sample and obtaining an optical cross-section of the device, as shown in Figure 3.9. Instead of the full height of the ridge, the measured depth of the etch was approximately 7 μm, leaving a potential issue with electrical isolation. To address this, a focused ion-beam etch post-process step was considered to remove the remaining material [13].

To provide total electrical isolation in this instance, the focused ion-beam etch would be used to mill through the residual material between the ridge and the ring resonator. It is crucial to carefully analyse the etch process parameters, to limit any possible damage to the surrounding material and to make sure that the etch is performed with the necessary precision and accuracy.

Four trial QCL/modulator devices were fabricated before fabricating "Device C". However, testing one the trial devices showed that the FIB milling post-process step used to fix the under-etch between the QCL ridge and the modulator was found to be challenging.

Because the trench width was greater than the ion-beam area, a substantial percentage of the material that had been ablated was redeposited onto the side walls, causing the milling depth to be uneven and the side walls to be rough. This led to an electrical short in the trial device during a DC electrical measurement. As such, the FIB step was not used for "Device C".

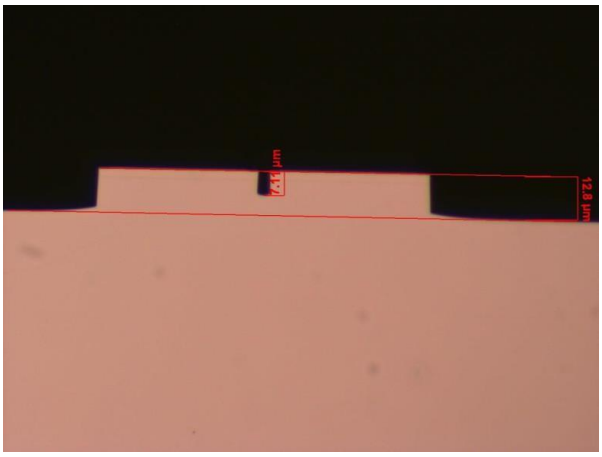

Figure 3.9: Cross-section of trial etch on sample GaAs material, showing the ring resonator and ridge in parallel

3.3.4 Modulator demonstration and test

The “Device C” structure was installed on a copper heat-sink mount after dicing. A series of electrical contact pads were wire-bonded to the structure, providing good electrical biasing to the device. The device was mounted on the cold-finger of a Janis ST-100 liquid-helium cryostat, shown in Figure 3.10. An Agilent 8114A high-current pulse generator was used to drive the device. Using two off-axis paraboloidal mirrors, the THz radiation was coupled into a helium-cooled bolometric detector.

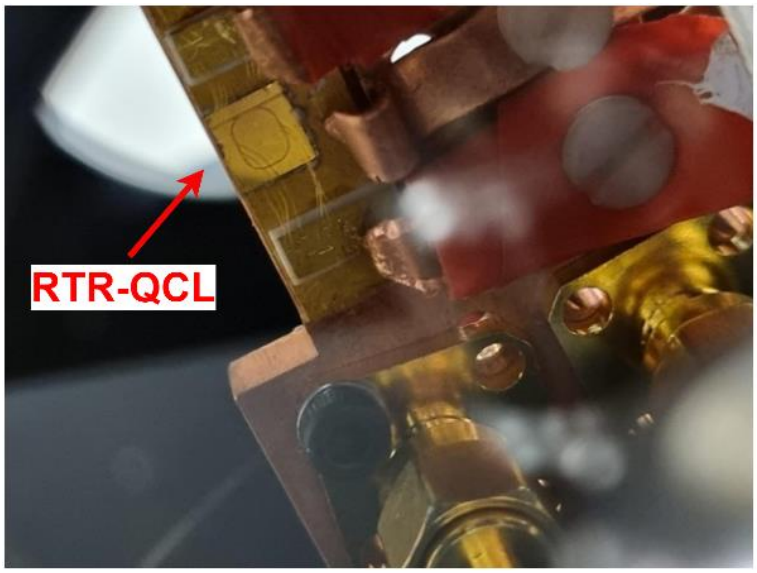

Figure 3.10: “Device C” mounted on the cold-finger of a Janis ST- 100 liquid-helium cryostat

The LIV characterisation when the ring resonator was switched off shows that the threshold current measured was around 0.37 A, as shown in Figure 3.11. Beyond this threshold current, the detector signal increases and reaches a peak at around 1.1 A drive current at 10 K temperature. The estimated range for the overall electrical power usage was 2.25-8.8 W, which is within the range of the RAL space-qualified Stirling cooler, for the KEYSTONE payload. Moreover the device lased up to 120 K in pulse-mode, which implies that the device can operate continuously without overheating. As continuous-wave emission is often preferred in many applications, this is a crucial aspect to consider.

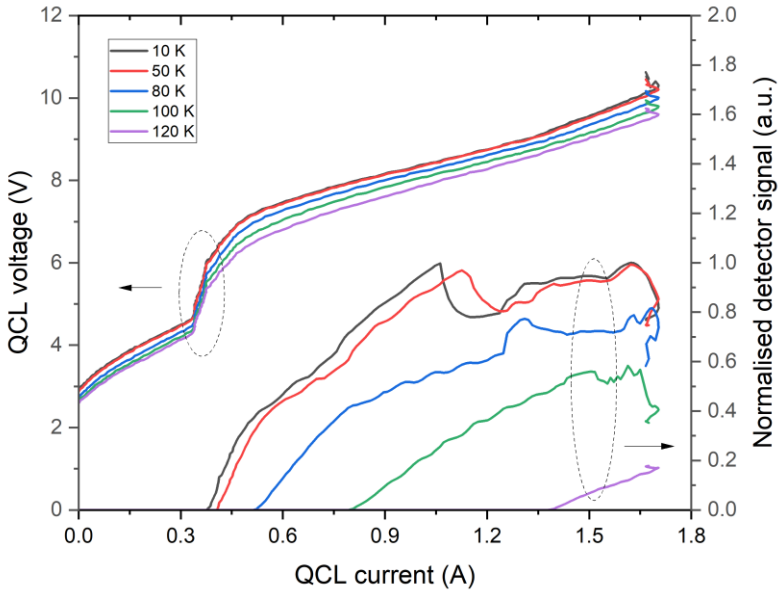

Figure 3.11: Detector signal and QCL voltage as a function of drive current into the QCL, with the ring modulator switched off.

Figure 3.12 shows the continuous-wave (CW) characterisation results of the "Device C" in which the detector signal and voltage of the QCL are shown as a function of the drive current, with the ring modulator switched off. The QCL was operated from a TTi DC power supply. The QCL has a threshold current of 0.5 A and peak emission at 1.30 A drive current at 40 K, with the ability to work up to 63 K in CW mode. Note that the THz power was too low for calibrated measurements and is shown in normalized arbitrary units. Some figures presented in the thesis do not include THz power measurement calculations and are thus plotted in normalized arbitrary units.

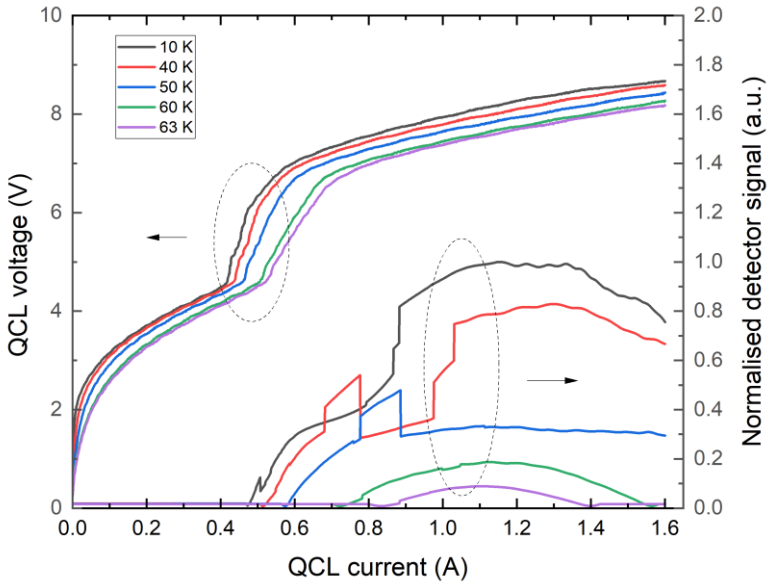

Figure 3.12: LIV characterisation of the "Device C" in CW mode. The device operated at different temperatures with the ring modulator switched off

In Figure 3.13 the characterization results shows the effects of the ring modulator on the output power of the QCL, when the Arroyo 4302 laser source was used to modulate the resonator. The output power of the QCL decreases with the increase of the drive current into the ring modulator. At a temperature of 50 K, the modulation depth can reach 100%, which suggests that the ring modulator is capable of producing a significant modulation effect on the device output power.

Overall, these results demonstrate that the continuous-wave output power of the QCL can be controlled over a ~30% modulation depth, i.e. larger modulation than the typical QCL power drift of ~5%. This satisfies the requirements of power lock system.

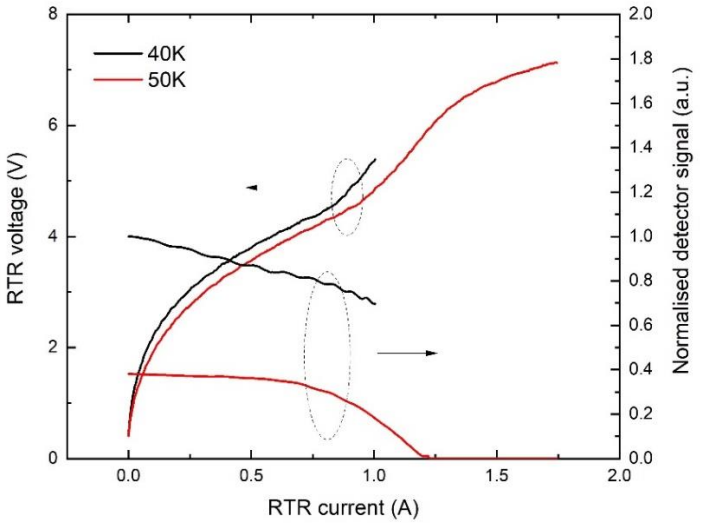

Figure 3.13: The QCL at a fixed current of 1.30 A and the ring-modulator driven by CW current.

The "Device C" was operated at 40 K. The emission spectrum of the device in continuous-wave operation was characterised using a Bruker FS66 Fourier Transform Infrared (FTIR) spectrometer. Radiation from the device is emitted mainly over four principal modes at around 3.277 THz, 3.285 THz, 3.372 THz and 3.392 THz, as shown in Figure 3.14. By varying the drive current to the QCL, the frequency of the two modes can be adjusted over a range of a few GHz, as shown in Figure 3.16.

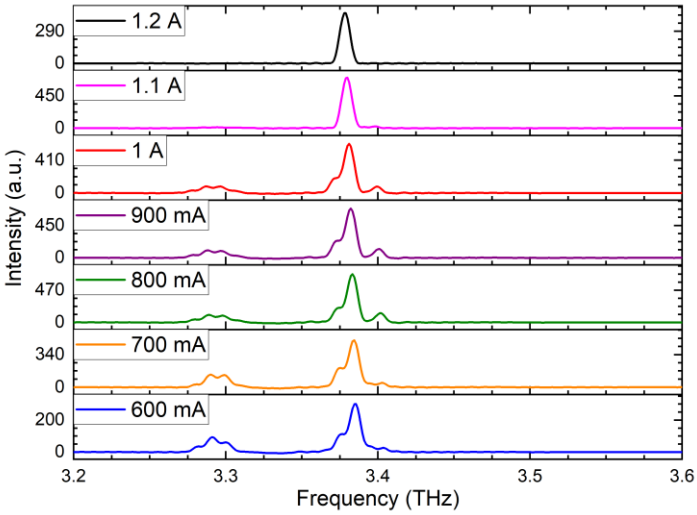

Figure 3.3.14: Emission spectra of the "Device C", obtained using a FTIR spectrometer at a range of drive currents, with the modulator switched off.

However, Figure 3.15 and Figure 3.16 shows that the laser frequency remains almost constant as the modulator bias varies. Modulator structure must exhibit such behaviour, resulting in adjusting the output power independently from the laser emission frequency. This is a desirable characteristic for many applications, as it allows for fine-tuning of the output power while maintaining a stable laser frequency.

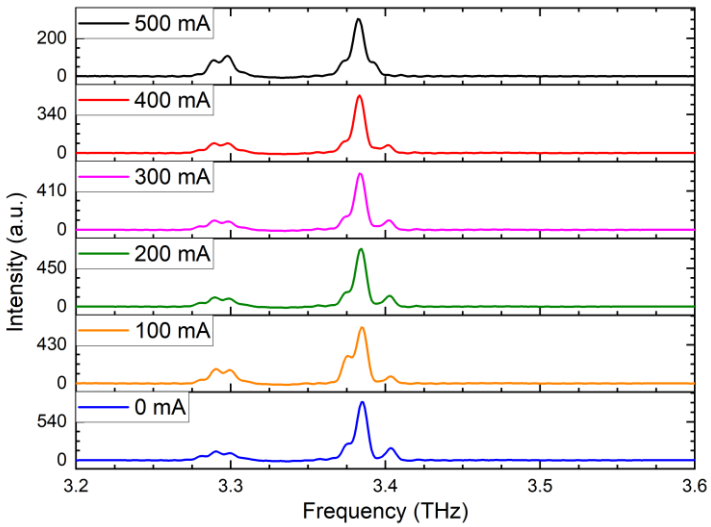

Figure 3.15: Emission spectra of the "Device C", obtained using a Fourier Transform Infrared spectrometer with the QCL at a fixed bias of 9.71 V and the ring-modulator driven at a range of currents.

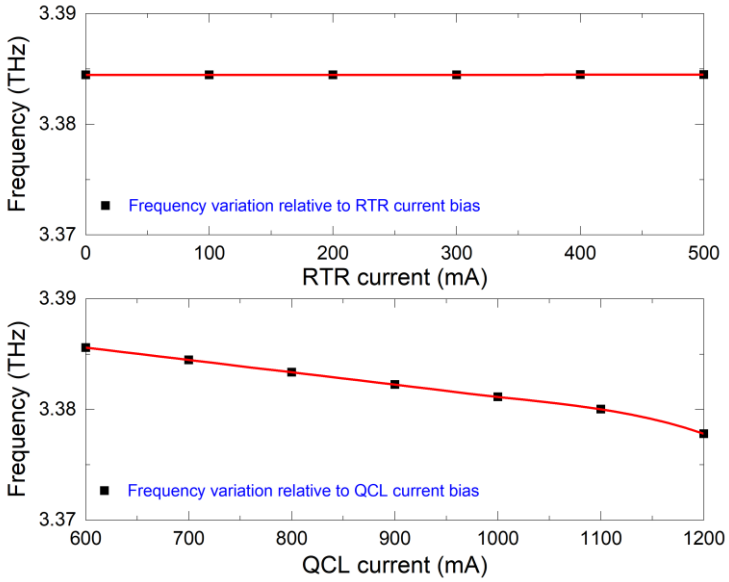

Figure 3.16: Frequency variation relative to QCL current bias) upon RTR switched-off, and RTR current bias upon QCL switched-off.

3.4 QCL Power locking system

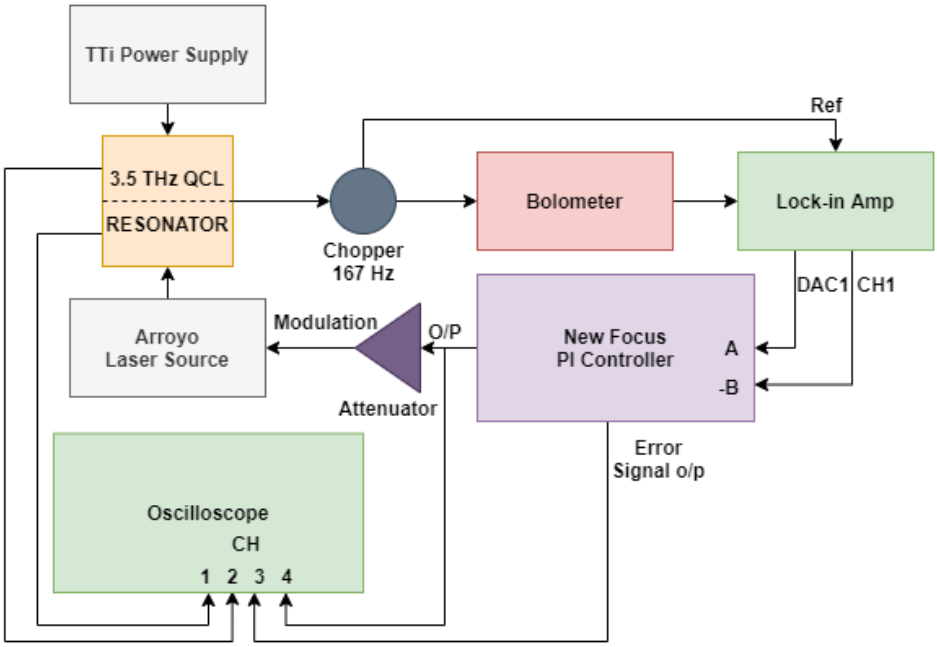

Figure 3.17: Schematic representation of power-lock system with PI controller.

The experimental configuration is shown as a schematic representation in Figure 3.17. The New Focus Proportional-Integral (PI) controller was used instead of the PID controller. The PI controller generated an error signal $e(t)$, by comparing the magnitude of the lock-in amplifier signal (B) to a reference voltage (A), which was set at 0.116 V, obtained by an instantaneous free-running detector voltage value.

$$e(t) = P_{set}(t) - P_{out}(t) \tag{3.1}$$

The proportional gain is set at 2, which corrects the large quantities of error in a short time interval, while the integral part sums the error over time and reduces the offset. The controlled output function $u(t)$ represent the proportional-integral control formalism;

$$u(t) = e(t)\left[k_p + k_i \int dt\right] \tag{3.2}$$

Following the modulation function shown in Figure 3.17, the minimum output power is obtained at the maximum modulator current. As such, the control system is

designed to operate at a zero-bias point in the middle of the modulator range, and to provide an increase in modulator voltage in response to an increase in the error signal.

$$V_{mod}(t) = \frac{V_{max}}{2}[1 - u(t)] \tag{3.3}$$

The Arroyo supply was set to 400 mA to restrict the modulation current to 350-500 mA to prevent overcurrent damage to the resonator. The modulation voltage-to-current conversion has been preconfigured within the modulation port of Arroyo supply, which is $I_{mod} = 0.2\ V_{mod}$. As a result, the maximum output of the PI controller was limited to ±10 V and attenuated it with a potential divider up to ±1 V.

A feedback loop was used to achieve amplitude stabilization by varying the modulator driving current, where the DAC1 signal of the lock-in amplifier was used as a reference for the "Device C" power level. The deviation of the power signal from this predefined set point was used as an error signal. To characterize the stabilization approach, we monitored the fluctuations of the output power of the "Device C" for different cases.

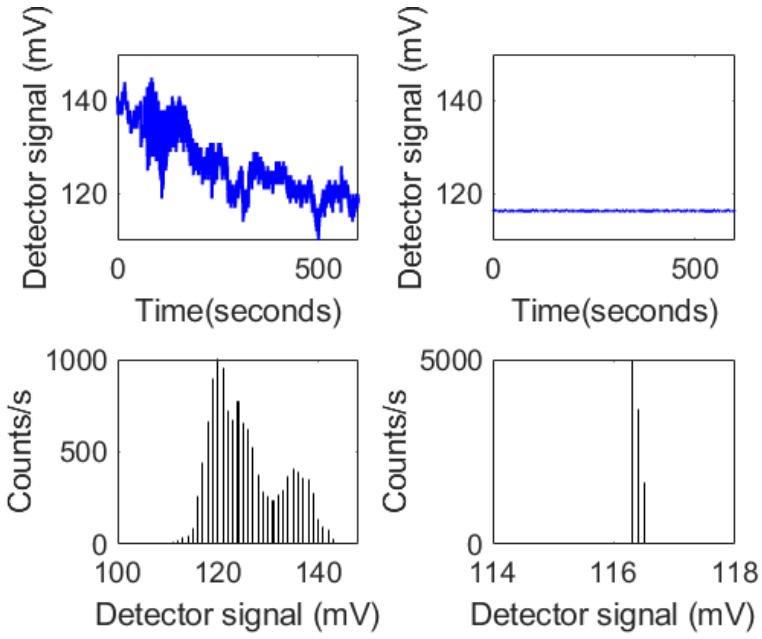

Figure 3.18: (a) Free-running QCL "Device C" output power versus time detected by the lock-in amplifier. (b) QCL output power-locked versus time detected by the lock-in amplifier. (c)–(d) Histograms of the power fluctuations corresponding to the unlocked state and the locked states respectively (limited by sensitivity of lock-in amplifier).

Figure 3.18 (a) and (b) show the free-running output power of the QCL and output power-locked of the QCL, respectively. The QCL output power depends on three control parameters: the QCL driving current, the heat sink temperature, and the modulator driving current. The temperature control is typically slow for active stabilization. The set point was predefined as 0.116 V on the lock-in amplifier with a time constant set of 50 milliseconds. The output power-locked was for 623 seconds at 40K temperature, which is a desirable power stability duration for THz QCL integrated into the KEYSTONE satellite mission, as the observation cycle of the satellite is 300 seconds of observation cycle, so need power stability for 300 seconds.

The free-running QCL had a standard deviation of 6.96 mV, whereas the power-locked QCL exhibited a significantly lower standard deviation of 72.3 µV, indicating a substantial reduction in power fluctuation compared to the free-running QCL. The free-running QCL exhibited a calculated noise power density of 1.55 mV/√Hz, whereas the power-locked QCL showed a significantly improved noise reduction, with a noise power density of 16.2 µV/√Hz.

Figure 3.18 (c) and (d) show the histogram of free-running QCL output power and QCL output power-locked, respectively. Comparing the power stability for the cases of the free-running and power-locked, the fluctuations in the free-running case and its non-Gaussian shape are a consequence of the relatively strong amplitude fluctuations correlated with the mechanical vibrations. When the amplitude stabilization loop is active, the output power becomes well stabilized, and the fluctuations are reduced.

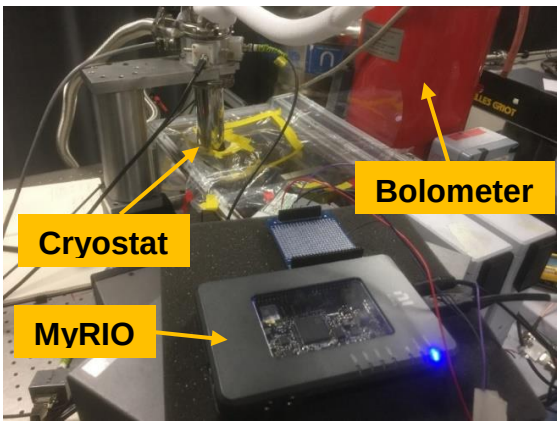

Figure 3.19: MyRIO National Instrument as an FPGA based PID controller.

A real-time implementation of such a controlled loop may be realized with the help of a controller based on a field-programmable gate array (FPGA), shown in Figure 3.19. Compared to the conventional PID implementation, using an FPGA-based controller offers several benefits, including enhanced speed, the ability to handle complex functions, and low power consumption. Additionally, FPGA-based platforms have the capacity to perform concurrent operations, enabling the parallel architectural design of various digital control systems [14].

By replacing the PI controller with the FPGA based PID controller, the controlled output function $u(t)$ represent the Proportional-Integral- Derivative control formalism;

$$u(t) = e(t)\left[k_p + k_i \int dt + k_d \frac{\partial}{\partial t}\right] \tag{3.4}$$

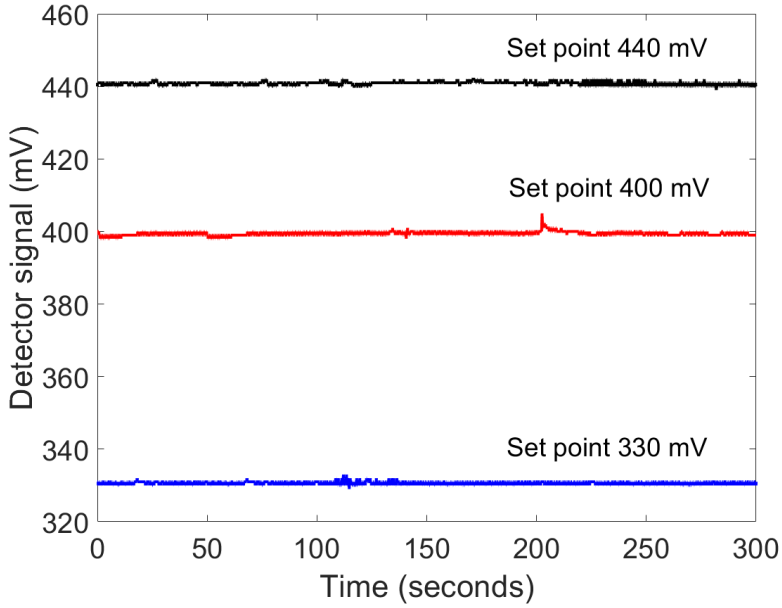

Figure 3.20: QCL "Device C" output power-locked at different set points.

Figure 3.20 shows the "Device C" output power locked by using a FPGA based PID controller. In this work, we used the MyRIO National Instrument as an FPGA based PID controller. Power-locking was performed for various set points, and at each set point, the PID controller minimized the error signal. The PID gains were arbitrarily set as $K_c = 0.1$, $T_i = 0.001$ and $T_d = 0.00075$. The power-lock duration was up to 300 seconds, where the temperature was set at 30K and the lock-in amplifier set on 50

ms time constant. The calculate standard deviation and noise power density for the set points is shown in the Table 3.1.

Table 3.1: Standard Deviation and Noise Power Density Measurements for power-locked QCL "Device C" using FPGA-based PID controller.

Set point (mV)	Standard deviation (μV)	Noise power density (μV/√Hz)
330	**425.5**	**95.2**
400	**588.3**	**131.5**
440	**443.8**	**99.2**

The power-locking using an FPGA-based PID controller has demonstrated higher standard deviation and noise power density compared to the New Focus Proportional-Integral (PI) controller. There could be multiple reasons for this; firstly, the experiments were conducted on different days, potentially leading to variations in the system purge and introducing slight mechanical noise that could affect the results. Additionally, the FPGA controller converts the analog signal to digital, processes it, and then converts it back to analog. In this process of conversion, a few data bits might get lost due to quantization, which could contribute to the observed differences in standard deviation and noise power density.

3.5 Conclusions

"Device C" have been integrated monolithically with racetrack resonator structures, which are suitable for power-locking. These devices have been processed into high-performance double-metal waveguides, and exhibit emission at around 60 K in continuous-wave operation. Crucially, the emission frequency was shown not to change by a measurable amount as the bias on the modulator structure was adjusted, indicating that independent control over the emission power and frequency could be realised.

The output power stabilization of a THz QCL operated in a compact cryocooler using PI, and PID controller was successfully demonstrated. For output power regulation, no external THz optical modulator is required. Output power was adjusted via the modulator driving current to confine the THz field and thus resulting in THz output power modulation. This work could play a vital role in enhancing the performance of high-resolution spectroscopic systems and could potentially be used in satellite integration for detecting gas species in the atmosphere.

Overall, the power-lock approach demonstrated in Chapter 3 has a slow response time due to the slow speed of the optical chopper (below 200 Hz), which affects the THz detection speed. This limitation can be excluded by using the current modulation technique or a fast DC coupled detector, such as a TeraFET (discussed in Chapter 5). The main advantage of using current modulation is that the response time can be fast as the frequency can be reached up to 100 kHz, suitable for PIDs. Hence performing a fast power lock.

Bibliography

[1] B. Swinyard *et al.*, 'The LOw Cost Upper atmosphere Sounder: The "elegant breadboard" programme', in *2015 8th UK, Europe, China Millimeter Waves and THz Technology Workshop (UCMMT)*, Sep. 2015, pp. 1–4. doi: 10.1109/UCMMT.2015.7460627.

[2] Y. Ren *et al.*, 'Frequency and amplitude stabilized terahertz quantum cascade laser as local oscillator', *Appl. Phys. Lett.*, vol. 101, no. 10, p. 101111, Sep. 2012, doi: 10.1063/1.4751247.

[3] B. Wei *et al.*, 'Amplitude stabilization and active control of a terahertz quantum cascade laser with a graphene loaded split-ring-resonator array', *Appl. Phys. Lett.*, vol. 112, no. 20, p. 201102, May 2018, doi: 10.1063/1.5027687.

[4] T. Alam *et al.*, 'Frequency and power stabilization of a terahertz quantum-cascade laser using near-infrared optical excitation', *Opt. Express*, vol. 27, no. 25, pp. 36846–36854, Dec. 2019, doi: 10.1364/OE.27.036846.

[5] D. S. Jessop *et al.*, ‘Graphene based plasmonic terahertz amplitude modulator operating above 100 MHz’, *Appl. Phys. Lett.*, vol. 108, no. 17, p. 171101, Apr. 2016, doi: 10.1063/1.4947596.

[6] W. Liu *et al.*, ‘Graphene-enabled electrically controlled terahertz meta-lens’, *Photonics Res.*, vol. 6, no. 7, pp. 703–708, Jul. 2018, doi: 10.1364/PRJ.6.000703.

[7] H.-T. Chen, W. J. Padilla, J. M. O. Zide, A. C. Gossard, A. J. Taylor, and R. D. Averitt, ‘Active terahertz metamaterial devices’, *Nature*, vol. 444, no. 7119, pp. 597–600, Nov. 2006, doi: 10.1038/nature05343.

[8] A. H. Castro Neto, F. Guinea, N. M. R. Peres, K. S. Novoselov, and A. K. Geim, ‘The electronic properties of graphene’, *Rev. Mod. Phys.*, vol. 81, no. 1, pp. 109–162, Jan. 2009, doi: 10.1103/RevModPhys.81.109.

[9] X. He, Z.-Y. Zhao, and W. Shi, ‘Graphene-supported tunable near-IR metamaterials’, *Opt. Lett.*, vol. 40, no. 2, pp. 178–181, Jan. 2015, doi: 10.1364/OL.40.000178.

[10] S. J. Kindness *et al.*, ‘Active Control of Electromagnetically Induced Transparency in a Terahertz Metamaterial Array with Graphene for Continuous Resonance Frequency Tuning’, *Adv. Opt. Mater.*, vol. 6, no. 21, p. 1800570, 2018, doi: 10.1002/adom.201800570.

[11] I. Kundu, J. R. Freeman, P. Dean, L. H. Li, E. H. Linfield, and A. G. Davies, ‘Terahertz photonic integrated circuit for frequency tuning and power modulation’, *Opt. Express*, vol. 28, no. 4, pp. 4374–4386, Feb. 2020, doi: 10.1364/OE.380656.

[12] W. Bogaerts *et al.*, ‘Silicon microring resonators’, *Laser Photonics Rev.*, vol. 6, no. 1, pp. 47–73, 2012, doi: 10.1002/lpor.201100017.

[13] W. R. Wagner, S. E. Sakiyama-Elbert, G. Zhang, and M. J. Yaszemski, Eds., *Biomaterials science: an introduction to materials in medicine*, Fourth edition. London, United Kingdom ; San Diego, CA: Academic Press, an imprint of Elsevier, 2020.

[14] M. Kocur, S. Kozak, and B. Dvorscak, ‘Design and Implementation of FPGA - digital based PID controller’, in *Proceedings of the 2014 15th International Carpathian Control Conference (ICCC)*, May 2014, pp. 233–236. doi: 10.1109/CarpathianCC.2014.6843603.

Chapter 4
Terahertz quantum cascade laser waveguide integration

4.1 Local oscillator requirements

The main objective of the KEYSTONE payload is to incorporate five infrared receiver channels and a set of "supra-THz" radiometry channels. These channels operate in the range of 0.8–4.7 THz and are carefully chosen to cover key MLT species, as outlined in Table 1.1.

The heterodyne receiver architectures proposed for the system employ either fundamental or subharmonic Schottky barrier diode mixing technology for the initial stage of frequency down-conversion. The availability of the local oscillator (LO) and its capacity to generate adequate RF power to effectively drive the mixer for optimal performance are the primary considerations that influence the mixer type [1]. However, its application in Bands 1-3 requires generating ~4 mW of power at frequencies higher than 2 THz.

The existing harmonic up-conversion-based LO technology is unable to generate the required power for Bands 1-3 at supra-THz frequencies. Therefore, an alternate approach is required for the LO availability in these bands. In the supra-THz range, direct signal production becomes essential. Previously, the most effective method of achieving this was through the use of CO_2-pumped far infrared molecular lasers [2]. However, these systems are complex, bulky, heavy, and consume high amounts of power, and introduce long term stability issues.

Fortunately, the development of QCL devices has resulted in a considerable advancement in the ability to provide LO power at supra-THz frequencies. QCLs have the capacity to directly generate high supra-THz LO power. They utilize miniature

semiconductor components on a millimetre scale and consume only a few Watts of power. This advancement has revolutionized the availability of LO power for Bands 1-3. The emission frequency of THz QCLs is not restricted by the inherent properties of the semiconductor material but rather by the thickness of the epitaxial layers. This feature enables the design of QCLs as narrowband sources, allowing them to operate at specific frequencies within the 1.2–5.4 THz range [3], [4]. THz QCLs are acknowledged as viable radiation sources for EO and space-based applications. Their application as 4.7 THz local oscillators (LOs) in the SOFIA/GREAT heterodyne spectrometer [5] and in the STO-2 [6] and OSAS-B [7] balloon-borne observatories are notable examples of their use.

However, several challenges must be overcome before they can be used as satellite-borne LOs. These include the inherently poor far field beam quality of unmounted QCLs, and the difficulty in integrating QCLs into fundamental mode waveguides.

4.2 Quantum cascade laser integration

The fabrication and integration of the unmounted QCLs on the heatsink adapter within the cryostat are demonstrated in Chapter 2. Unmounted QCLs used in free-space applications have limitations due to their typical total thickness, which ranges from 10 to 15 μm. A highly divergent beam is emitted because this thickness is substantially less than the wavelength. As a result, the practical applications of unmounted THz-QCLs are constrained due to their limited suitability for free-space applications.

THz QCL beam quality can be enhanced in several ways, including patterning the laser ridge facet [8]–[10] or by incorporating antennas and lenses [11], [12]. Although in order to establish QCLs as feasible laser sources for space and atmospheric applications, it is crucial to develop integration techniques that allow seamless integration of the QCL with external components like waveguides and mixers. Additionally, these integration methods should eliminate the requirement for extra optics, which can lead to alignment issues. The integration approach should also be in accordance with the specifications for KEYSTONE satellite usage, considering factors such as allowed volume, mass, and power consumption.

The issues of THz QCL beam quality have been addressed in several ways throughout the years, with the goal of developing a fully integrated heterodyne system. The integration of a Schottky diode into the QCL waveguide cavity in [13], for instance, presented a novel technique. The system design was made simpler by this integration since an optical coupling channel to the mixer is no longer required. Similarly, [14] successfully integrated a THz QCL with a hot electron bolometer (HEB) mixer. This integration eliminates the requirement for an optical path between the local oscillator (LO) and the mixer, further streamlining the system design. The realisation of a completely integrated heterodyne is made possible by these developments in integration methods.

The previously mentioned methods often involve the use of large and delicate components or complex semiconductor device processing, which can result in a bulky or intricate system. In this particular project, a different integration method is employed to address these challenges. The objective is to develop an integrated approach that is suitable for space operations while ensuring mechanical robustness and reproducibility.

Double-metal waveguide QCLs offer superior thermal performance and are well-suited for near-field radiation coupling. However, QCLs face challenges including poor far-field beam quality and wide divergence when used in large-scale outdoor environments, resulting in poor coupling with external free-space optical components. These challenges can be reduced by integrating QCLs within a metallic block, providing better mechanical protection and shielding them from exposure to ionizing radiation [15].

The THz QCL devices in this chapter are “Device D, Device E, and Device F” which were assembled within a metallic waveguide cavity that is precisely micro-machined, as shown in Figure 4.1. The device specifications is outlined in the appendix Table B. This integration strategy involves incorporating a diagonal feedhorn to the end of the cavity to improve far field beam quality.

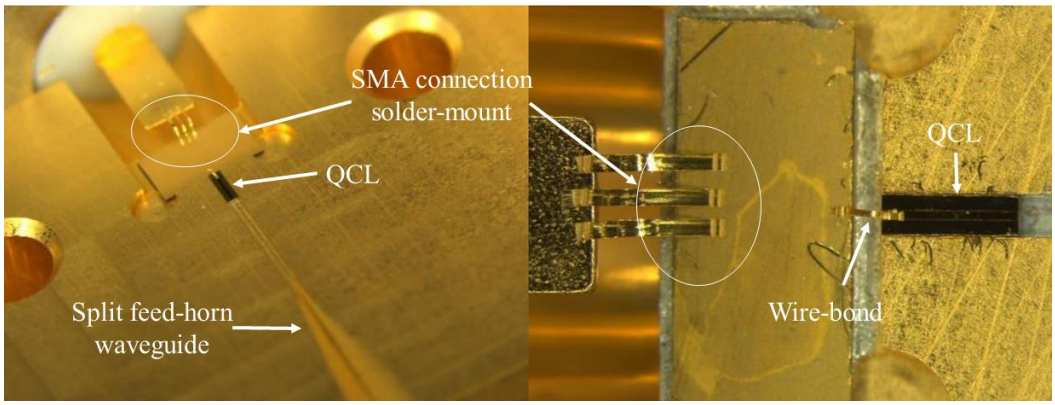

Figure 4.1: Block integration of THz QCL with solder-mounting inside a micro-machined waveguide.

Using horn antennas, the initial demonstration of this concept was conducted in the microwave frequency band [16]. Its capabilities were later expanded to include THz frequencies, leading to modifications that drastically reduced the beam divergence (< 20 degrees) [15], as horn antennas offers a notable level of directivity and gain [17]. THz QCLs were first used with rectangular feedhorns [15]. However, later iterations incorporated a diagonal feedhorn design [18], [19]. Adopting a diagonal feedhorn allowed for a gradual narrowing of the beam coming out of the metallic block, which further reduced the beam divergence. Using a cylindrical feedhorn could make the beam quality much better. Although, processing it becomes harder and more complicated.

A waveguide cavity is accurately machined into a pair of oxygen-free Copper (Cu) blocks in order to accomplish the integration of the QCL. The waveguide channel includes a diagonal feedhorn cut into either end. The QCL is mounted within the waveguide channel using a solder-mount. The two Cu blocks are then assembled to form a rectangular waveguide structure by aligning them using alignment dowels.

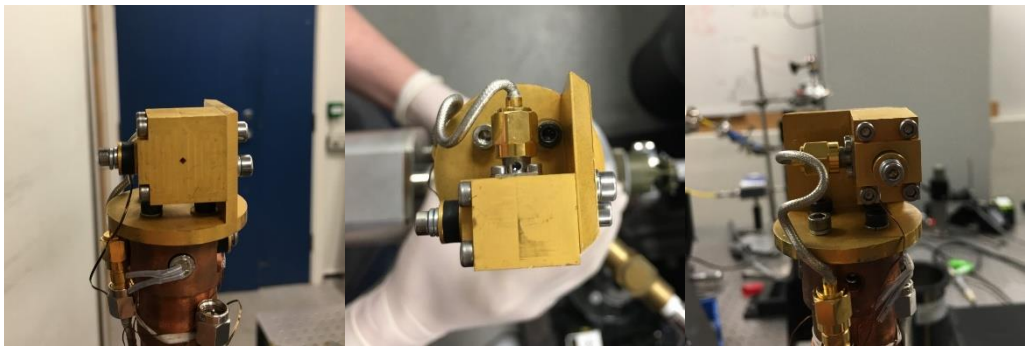

Figure 4.2: Mounting block integration of a QCL on a heatsink adapter with connection to SMA cable and temperature sensor.

As shown in Figure 4.2, a temperature sensor is attached to one of the Cu blocks in order to monitor the temperature of the QCL's heat sink. As seen in Figure 4.2, a SMA connection is found on the back facet of the device through which the QCL is biased.

Prior to mounting the QCL, the Cu blocks undergo diamond turning and electro-less gold plating processes. These treatments serve to prevent corrosion and enhance the thermal performance of the integrated system.

A range of QCL devices were integrated into waveguides in this work. The following section describe device operating at 3.5 THz – “Device D”, 4.7 THz – “Device E” and 2.0 THz – “Device F” including the integration of a racetrack resonator in “Device D”.

4.3 Integrated 3.5 terahertz quantum cascade laser

4.3.1 3.5-THz QCL with integrated RTR modulation

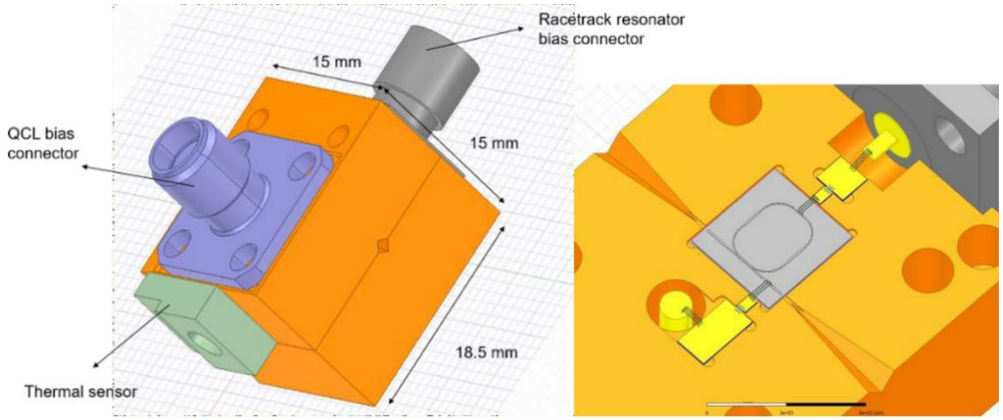

Figure 4.3: CAD drawing of (top left) external, and (top right) internal structure of waveguide block.

Chapter 3 discussed RTR modulation of the QCL using “Device C”. A similar design was used to fabricated and integrated 3.5 THz RTR-QCL into micro-machined waveguide, which is “Device D”. In the CAD design of the micro-machined waveguide shown in Figure 4.3, a decision was made to incorporate two diagonal feedhorns [19], rather than opting for a single-feedhorn configuration. This strategic choice offers two primary advantages. Firstly, the use of two diagonal feedhorns allows both facets of the QCL to be simultaneously exposed. This facilitates the utilization of one facet for the LO output, while the other facet can be effectively coupled into a power monitoring or stabilization subsystem. Secondly, by employing a dual-feedhorn design, the potential issue of introducing a back-short into the waveguide cavity, which can arise in a single-feedhorn configuration, is effectively mitigated. The presence of a back-short necessitates precise positioning of the QCL to effectively manage the formation of standing waves. These considerations highlight the significance of the decision to adopt a two diagonal feedhorn design, contributing to the enhanced functionality and performance of “Device D”.

Figure 4.4 (left) illustrates the design of the waveguide module, which incorporates a split waveguide feedhorn structure. The waveguide dimensions employed were (165 × 82) μm². These dimensions were undertaken in order to ensure desired beam

characteristics since similar-sized structures efficiently out-couple THz power and produce a nearly Gaussian far-field beam profile [15], [19]. Figure 4.4 (right) depicts the internal and external views of the assembled device.

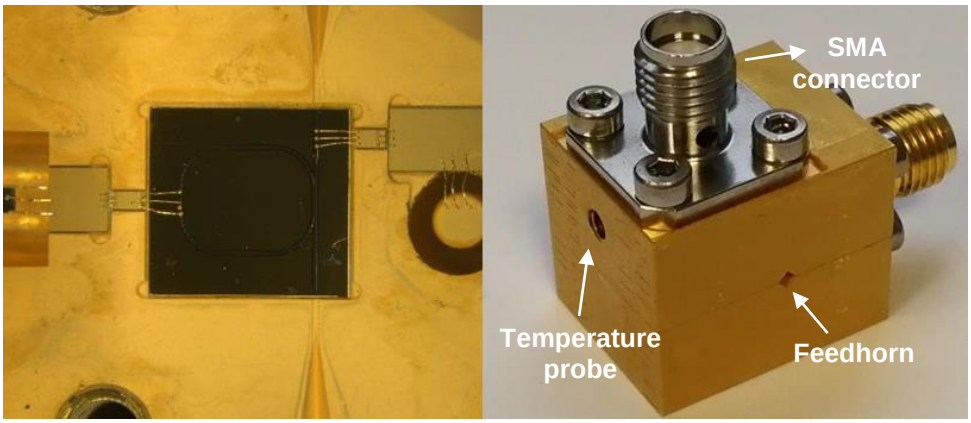

Figure 4.4: Microscope images of the assembled "Device D", showing (left) the complete chip integrated into the waveguide assembly, photographs showing external views of the assembled block-integrated "Device D" (right).

4.3.2 "Device D" characterisation

A Janis ST-100 helium–flow cryostat was used to run the "Device D", which was cooled using a continuous flow of liquid helium to maintain a stable temperature of 10 K. The QCL was driven by the Agilent pulse generator, delivering current pulses at a repetition rate of 10 kHz and a duty cycle of 2%. A signal generator generated a square-wave envelope with a frequency of 167 Hz, which was used to modulate the electrically gated pulse train. A pair of off-axis parabolic mirrors were used to collimate and focus the radiation onto helium-cooled silicon bolometric detector in order to capture the THz power. The Lock-in amplifier recorded the time-averaged detector signal, which was referenced to the 167 Hz modulation envelope. Figure 4.5 shows the measured light-current-voltage characteristics. The device operated successfully in pulsed mode, reaching a maximum operating temperature of 120 K. However, continuous-wave operation was not achieved. The maximum output power obtained in pulse mode was ~70 µW.

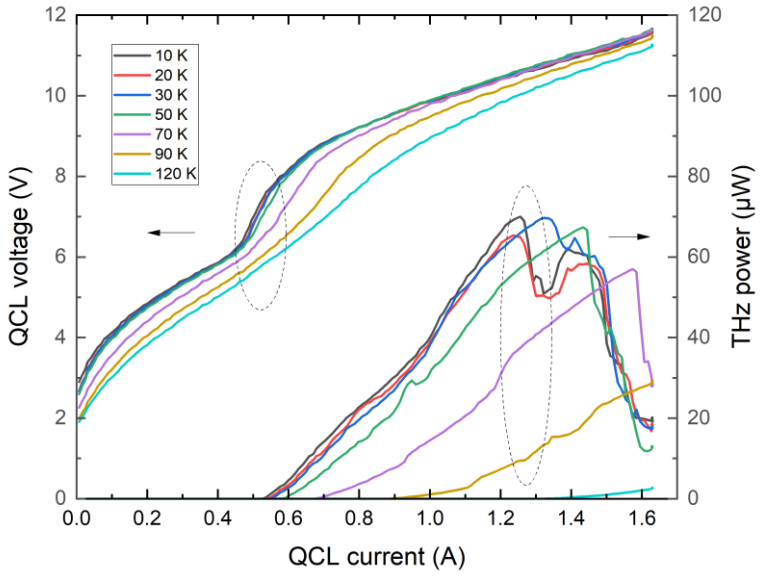

Figure 4.5: Pulsed light–current–voltage measurements of "Device D". The THz detector signal and QCL terminal voltage are shown as a function of the drive current, with zero bias across the resonator structure. LIV characteristics as a function of operating temperature.

Figure 4.6 presents a comparison between "Device C" and "Device D". The "Device D" exhibits a higher electrical impedance during continuous-wave operation. This increase in impedance may indicate poor soldering to the waveguide block, possibly due to the contact effect between the QCL and the waveguide structure. Additionally, the imperfect machining of the heatsink adapter used to connect the QCL to the cryostat may contribute to an elevated thermal resistance, further impacting device performance. Together, these effects may explain the lack of CW operation of "Device D".

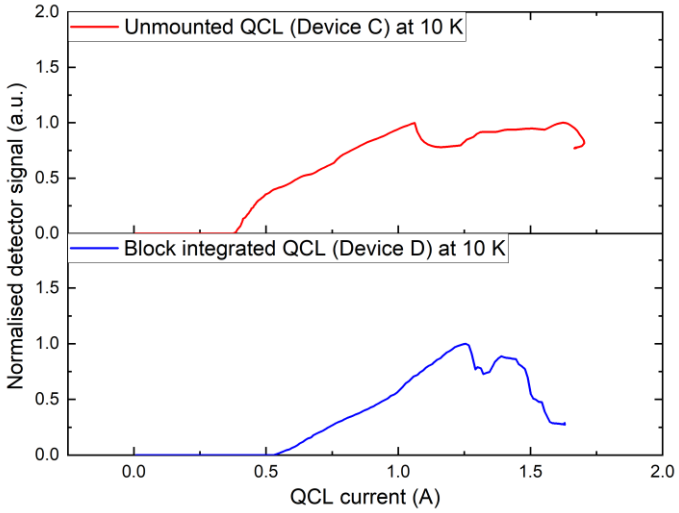

Figure 4.6: Comparison between the waveguide-integrated and unmounted devices at low temperature.

Figure 4.7 and Figure 4.8 showcases the characterization of the "Device D" emission spectrum (during pulse operation) using a Bruker IFS/66 Fourier Transform Infrared (FTIR) spectrometer. Figure 4.7 shows the QCL's emission spectrum for a range of driving currents while maintaining the RTR bias constant at 300 mA.

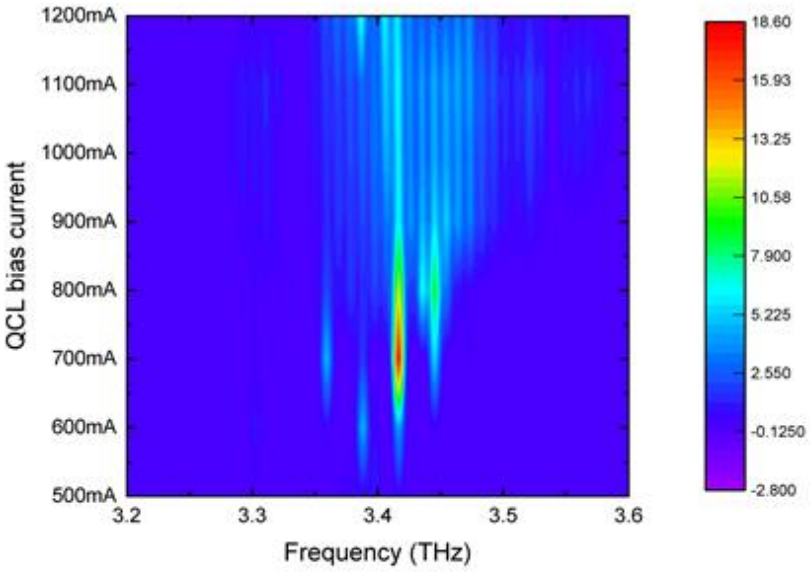

Figure 4.7: Emission spectra of "Device D" for different QCL bias current, obtained using a Fourier Transform Infrared spectrometer. Modulator current constant at 300mA.

When the QCL bias current exceeds 900 mA, the emission spectrum shows the presence of multiple modes. The FSR was measured to be ~10 GHz between each pair of modes. This indicates that these multiple modes are harmonics originating from the QCL. The following equation 4.1 was used to determine the FSR:

$$\Delta f = \frac{c}{2nL} \tag{4.1}$$

Where L is the cavity's length, which in this case is 4 mm, n is the refractive index, and c is the speed of light.

When a QCL bias of 700 mA was applied, the device emitted radiation at four principal frequencies at ~3.36 THz, 3.388 THz, 3.418 THz, and 3.446 THz. Only some modes were visible, indicating lower gain. These frequencies resulted in a free spectral range (FSR) of ~28 GHz within a Fabry-Perot cavity.

The obtained results suggest that the “Device D” exhibits a cleaner resonant cavity compared to the “Device C”. There could potentially be several explanations for such results. One explanation is that the “Device C” was measured at 40 K whereas the block-integrated device was tested at a lower temperature of 10 K. The detection of extra modes that were present in the block-integrated device may have been hindered in the unmounted device measurement at higher temperatures.

Another possible explanation is related to the odd-parity modes of “Device C”. It is plausible that these modes are being suppressed due to a defect present in the middle of the QCL ridge. The etching process used to separate the modulator from the ridge in the unmounted device may have resulted in such a defect. This defect may have influenced the resonance characteristics of the unmounted device, leading to the observation of additional modes.

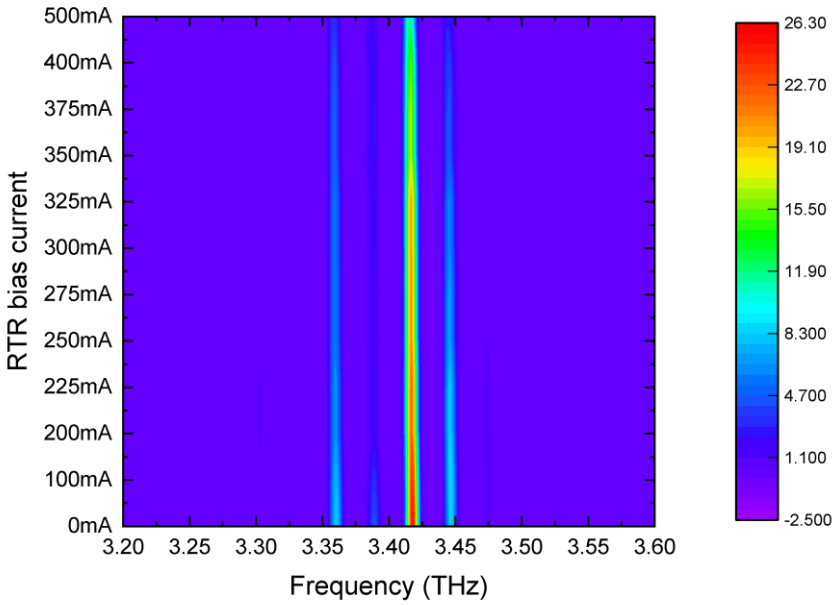

Figure 4.8: Emission spectra of "Device D" for different RTR bias current, obtained using a Fourier Transform Infrared spectrometer. QCL bias current constant at 720mA.

In contrast, Figure 4.8 shows the modulator's emission spectrum at various RTR driving currents, while maintaining a constant QCL bias of 720 mA. The device emits radiation mainly in four primary modes, centred around approximately 3.36 THz, 3.388 THz, 3.418 THz, and 3.446 THz. Notably, despite varying in the modulator bias, the QCL frequency remains constant, which was expected. However, power modulation was not observable as "Device D" did not work in CW mode.

4.4 Integrated 4.7 terahertz quantum cascade laser

4.4.1 Fabrication and micromachining of a 4.7 THz QCL in waveguide design

The 4.7 THz was manufactured using GaAs/AlGaAs materials grown by molecular beam epitaxy (MBE) based on a hybrid design explained in [20] The 4.7 THz QCL discussed in this chapter is "Device E" (specification the QCL devices is outlined in appendix Table?). Initially, a GaAs buffer layer was deposited on a 90 µm-GaAs

substrate, followed by an $Al_{0.25}Ga_{0.75}As$ etch-stop layer. Subsequently, a 17.2 nm thick n+ GaAs contact layer, doped with silicon (Si) at a density of 8×10^{16} cm^{-3}, was added. The active region consisted of repeated layers, resulting in a total thickness of 12 µm.

In order to process the device, a double-metal (DM) waveguide made of gold (Au) was used to create a transverse ridge with a width of 60 µm. The substrate was then thinned to 88 µm. The device was cleaved to a length of 1200 µm. Rectangular channels with a 170 µm × 40 µm cross-section were carefully machined inside each copper (Cu) block. Furthermore, alignment dowels were used to align and join the two blocks, creating a rectangular waveguide with a 170 µm × 80 µm cross-sectional area.

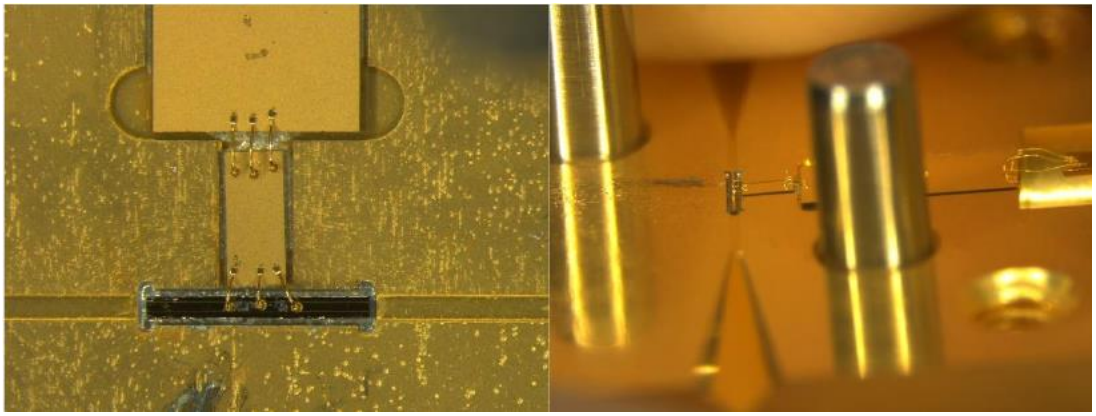

Figure 4.9: Block integration of a "Device E" with solder-mounting inside a micro-machined waveguide.

The chosen waveguide channel for "Device E" was quite large which leads to excessive overmoding for the QCL. Ideal requirement for the "Device E" should be a fundamental WM-47 waveguide of 47 µm and a height of 24 µm [21], which gives a cut-off frequency of 3.19 THz and operating range at 3.99 – 6.03 THz. However, making such a small and precise waveguide was too complex to achieve. Two diagonal feedhorns were manufactured with an aperture size of 1.56 mm × 1.56 mm along the diagonal. "Device E" was mounted into the channel using solder and connected to the SMA connector through wire bonding, as shown in Figure 4.9.

4.4.2 “Device E” characterisation

The LIV characteristics of the “Device E” were measured over a temperature range of 6-85 K and are presented in Figure 4.10. Under pulsed mode operation, the laser exhibited a current threshold of 323 mA and peak-power current value of 475mA at a heat-sink temperature of 6 K. Lasing was observed up to a maximum operating temperature of 80 K.

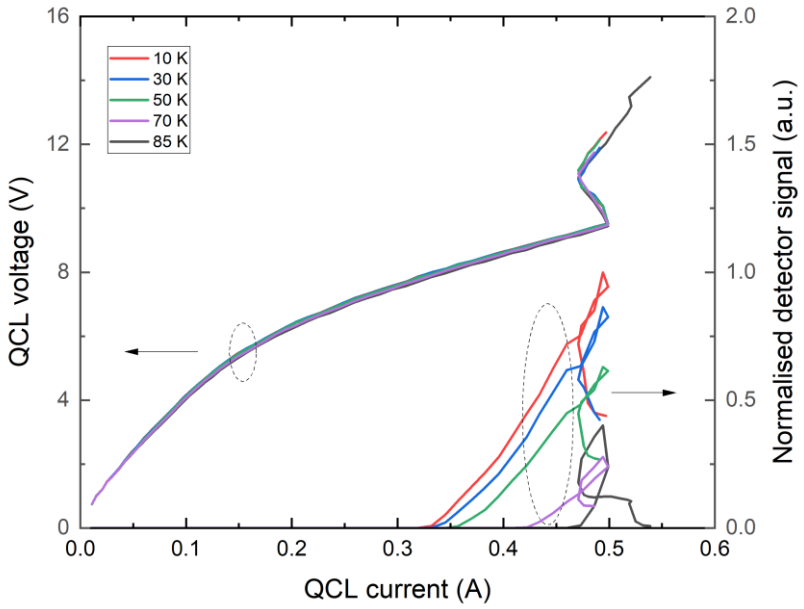

Figure 4.10: Pulsed LIV measurements of “Device E” as function of different temperatures.

Figure 4.11 illustrates the recorded FTIR spectrum. The “Device E” demonstrated multimode behaviour, with two primary emission modes at frequencies of 4.74 THz, and 4.78 THz. A 4 GHz change in frequency was observed in the main mode between 350mA and 500mA.

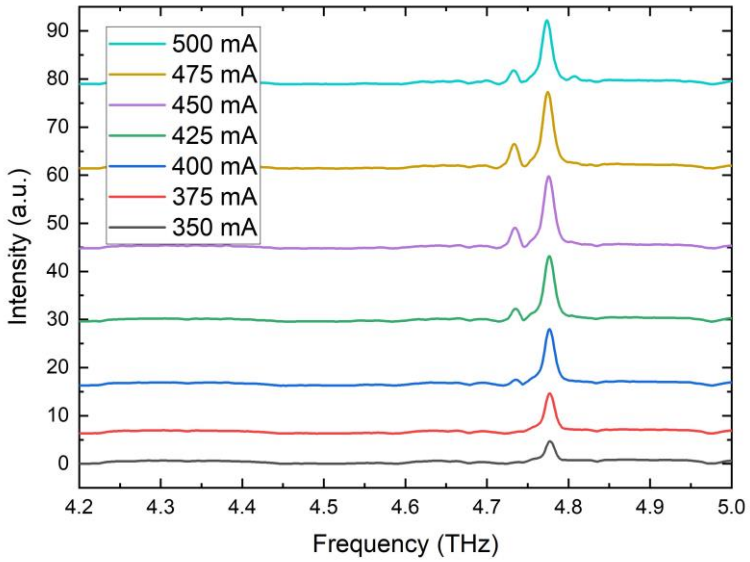

Figure 4.11: Emission spectra of "Device E" for different bias current. The plots are vertically offset for clarity.

Unfortunately, the output power of the "Device E" could not be accurately measured using an absolute THz photoacoustic power meter. The loss in power can be attributed to a high insertion loss caused by a mismatch between the laser cavity's mode profile and that of the waveguide, as well as between the waveguide aperture and free space. These mismatches can result in reflections within the laser cavity, leading to a decrease in output power.

Thermal analysis was conducted on the "Device E", revealing that it did not exhibit lasing behaviour in continuous wave (CW) operation, as shown in Figure 4.12 (Right). However, emission was observed when the device was operated at a duty cycle of up to 75% in continuous pulses, at a temperature of 20 K. Notably, as the duty cycle increased, there was a decline in the power output, as depicted in Figure 4.12 (Left).

In general, the temperature of the "Device E" active region can be approximated using the following equation:

$$T_{AR} \approx T_H + \gamma IVR_{th} \qquad (4.2)$$

Here, T_{AR} stands for the temperature of the active region, T_H for the temperature of the heatsink, denotes the duty cycle of the electrical power supply, I and V are the

supply current and voltage, respectively, and R_{th} is the thermal resistance between the active region and the heatsink of the QCL. Figure 4.13 (Right) shows the peak power as a function of heat-sink temperature. In this scenario with short pulses, the γ is ≈ 0. Therefore, the T_{AR} is roughly equal to T_H.

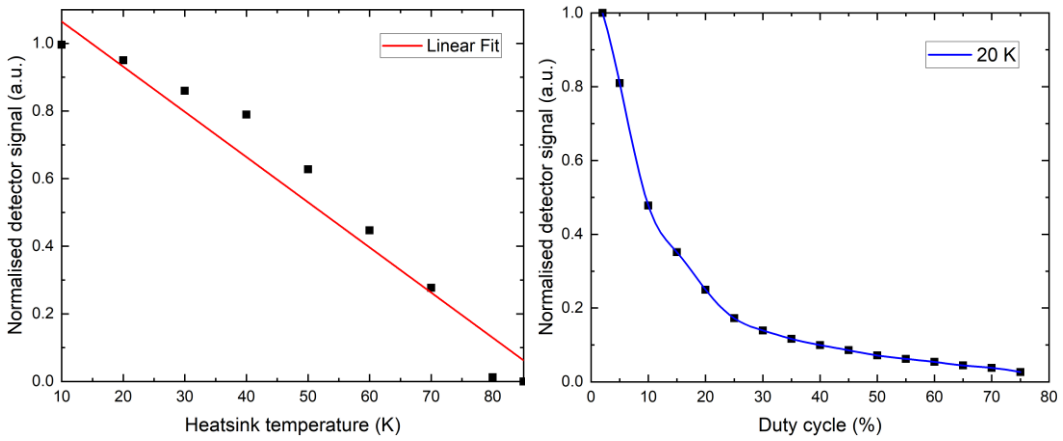

Figure 4.12: (left) Peak power recorded in pulsed mode. (Right) Peak power as a function of duty cycle, operating up to a 75 % duty cycle at 10 K.

To assess the thermal characteristics of the "Device E", the thermal resistance (R_{th}) was calculated using the equation 4.2:

$$R_{th} = \frac{\Delta T}{IV} \times 100 \qquad (4.3)$$

Here, ΔT represents the temperature offset ($T_{AR} - T_H$). The resulting thermal resistance for the device was determined from Figure 4.12 to be 31 K/W.

Based on this analysis, the inability of "Device E" to run continuously in CW mode may be due to defects in the thermal mounting process rather than inherent issues associated with the active region or waveguide design. This observation highlights the importance of optimizing thermal management strategies to enhance the performance of the device and enable efficient CW operation.

4.5 Integrated 2.0 terahertz quantum cascade laser

There are various benefits to using 2 THz QCL as local oscillators for satellite applications. The 2 THz line is a better alternative for a single-channel sensor due to several factors compared to the stronger 4.7 THz line of atomic oxygen.

One of the key advantages is the availability of numerous other spectral emission lines of interest within the 2 THz [O] window. On the other hand, the 4.7 THz [O] window primarily contains only the atomic oxygen line. This enables a 2 THz sounder to address a larger range of scientific objectives in comparison to a 4.7 THz device with a single channel, which could only measure atomic oxygen.

There are also technical benefits associated with a ~2 THz instrument. These instruments frequently employ heterodyne receivers, which display improved receiver noise temperature at lower frequencies. Therefore, a 2 THz radiometer would be more sensitive than a 4.7 THz radiometer and can determine weak signals more precisely.

Moreover, lower frequencies offer advantages in terms of surface roughness requirements and manufacturing precision for the optical telescope. At lower frequencies, it is typically simpler to satisfy these criteria, which facilitates design and manufacture. This further contributes to the overall cost-effectiveness of a ~2 THz instrument for in-orbit demonstrations.

The frequency band around 2 THz is highly significant for atmospheric radiometry due to its proximity to several important atmospheric gas species. For instance, the frequencies 2060.0 GHz, 2060.2 GHz, 2070.6 GHz, and 2070.5 GHz correspond to significant spectral lines of O, O_3, CO, and HO_2, respectively [22].

The relatively low emission frequency of the QCL in the 2 THz range offers certain advantages. It eases manufacturing tolerances, allowing for more lenient requirements in the fabrication process. Additionally, this lower frequency enables the use of a fundamental WM-130 waveguide. The 2.0 THz QCL discussed in this chapter is “Device F” (specification the QCL devices is outlined in appendix Table?). The “Device F” is first QCL which has been integrated into a rectangular metallic waveguide that complies with IEEE 1785.1-2012, standard for metallic waveguides [23].

4.5.1 Fabrication and micromachining of a 2.0-THz QCL in waveguide design

The active region of the "Device F" was grown using MBE on a semi-insulating GaAs substrate, following a design similar to [24]. The design utilized a GaAs/AlGaAs bound-to-continuum structure with $Al_{0.1}Ga_{0.9}As$, operating at a frequency of approximately 2 THz.

The fabrication process of the devices involved the use of an Au-Au double-metal waveguide, following the methods described in [25]. It began with wafer bonding, followed by the removal of the substrate using mechanical and wet etching techniques. The etch stop layer was then eliminated using hydrofluoric acid (HF). A maskless Aligner (MLA 150) was utilized to define the ridges, which had a width of 90 μm, through wet etching. The grating periods on the upper layer were also formed using wet etching, and a Ti/Au (10/130 nm) overlayer was deposited on the top. Finally, the substrate was thinned down to approximately 100 μm, and a Ti/Au (10/100 nm) metallization layer was evaporated on the back of the substrate to enhance adhesion. All devices were cleaved to a length of 2 mm.

Further for block integration, the fabricated QCL with gratings was solder-mounted carefully in micro machined rectangular waveguide structures, which then completes "Device F" fabrication and micromachining in waveguide block.

Although waveguide structures at frequencies of 3.5 THz [15], [19] and 4.7 THz [26] have already been developed, there is a possibility for the development of a fundamental waveguide at 2.0 THz. It is feasible to design and build a waveguide structure at 2.0 THz that satisfies the specifications for the height-to-width ratio and the need for appropriate wave propagation within the waveguide by following the IEEE standards.

$$f_c = \frac{c}{\sqrt{\varepsilon_r}} \times \frac{1}{2a} \tag{4.4}$$

Where c is the speed of light, ε_r is the relative permittivity of the channel medium (assumed equal to 1 for air), and a is the channel width.

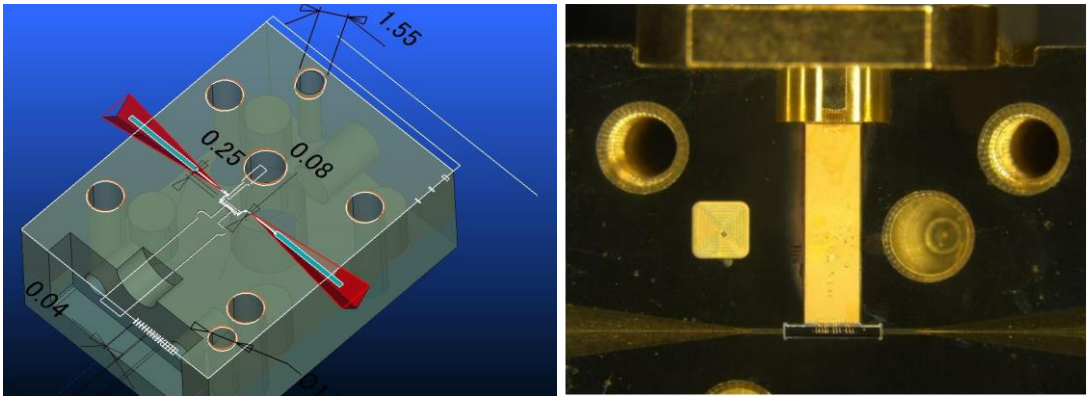

Figure 4.13: CAD rendering of waveguide module design (left) and internal view of “Device F” (right).

At the frequency of 2.0 THz, the optimal choice for fundamental operation is a WM-130 waveguide with dimensions of (130 × 65) μm². This waveguide configuration provides a lower cut-off frequency of 1.153 THz, which is recommended for use in the frequency range of 1.4–2.2 THz. Building upon this prior work, the integration of approximately 2 THz lasers into a similar precision-machined waveguide module was pursued following the dimensions specified by the IEEE WM-130 standard, as shown in Figure 4.13 (left).

Each laser facet in this configuration is effectively out coupled into free space by a diagonal feedhorn Figure 4.13 (right). The integration of the ~2 THz lasers into this waveguide module resulted in potential performance improvements compared to the higher-frequency devices.

One notable advantage was the relaxation of dimensional and surface-roughness tolerances at lower frequencies. The manufacturing process has been significantly simplified by the relaxing of tolerances, making it less complex and more cost-effective. Furthermore, operating the system in the fundamental mode at 2 THz yielded benefits like superior spectral performance. This fundamental-mode operation made it easier to couple to Schottky diodes and feedhorn antennas, improving the performance and efficiency of the entire system. [26].

“Device F”- waveguide block that was securely mounted onto the cold finger of a Janis ST-100 continuous-flow liquid helium cryostat is shown in Figure 4.14. Within the waveguide block, the THz beam is precisely coupled into a silicon bolometric

detector. A pair of off-axis paraboloidal mirrors is used to facilitate the coupling process.

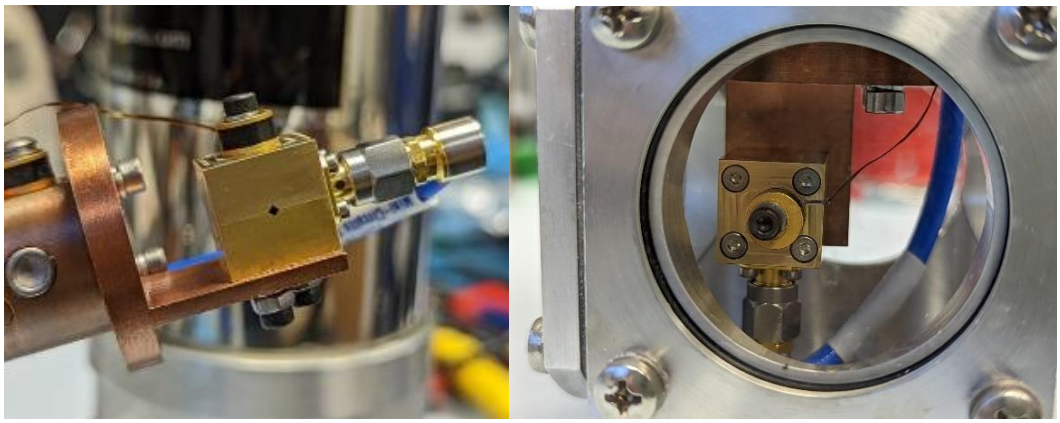

Figure 4.14: Integration of a “Device F”, which is a 2.0-THz LO Module into a Continuous-Flow Cryostat for Characterisation.

4.5.2 “Device F” characterisation

The device consumes approximately 1.5 W of electrical power, which aligns with the cooling system specifications. A silicon bolometric detector was used to measure the max output power in pulsed mode, which was 300 μW.

Figure 4.15 illustrates the emitted power in the THz range and the electrical behaviour of the device when operated in cw mode. The THz power in cw mode at 20 K was ~37 μW with 1.62 W of electrical power consumption. An emission frequency of 2.102 THz was successfully achieved at 50 K, which corresponds to a slight 2% deviation from the intended local oscillator (LO) frequency. In cw mode the QCL works up to 60 K having threshold current value at ~225 mA and peak current value at ~285 mA.

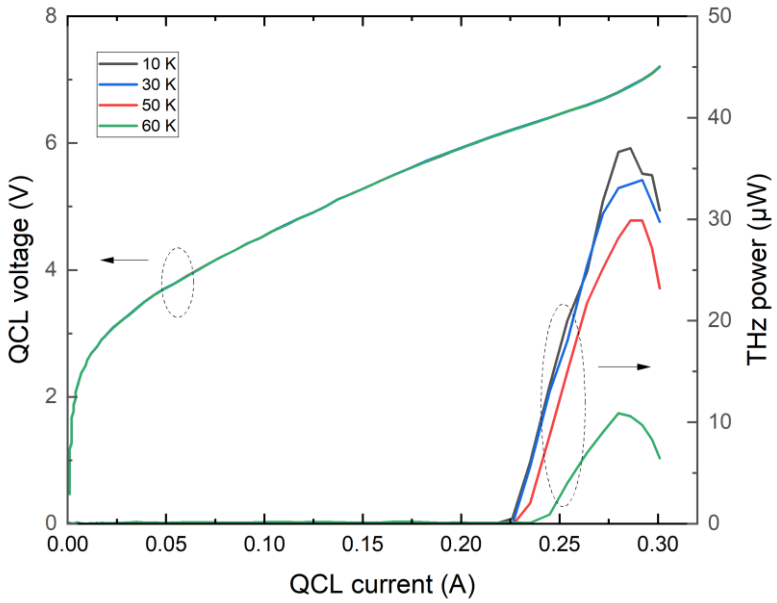

Figure 4.15: Continuous wave mode LIV measurements for "Device F" as function of different temperatures.

The difference between the maximum performance achieved in pulsed and continuous-wave (c.w.) operation can serve as a basis for estimating the thermal resistance.

The second component of the temperature approximation equation (4.2) is minimal when the QCL is operated with extremely short duty-cycle pulses. On the other hand, in continuous-wave operation, γ is equal to 1. As a result, the temperature offset between the continuous-wave and pulsed modes can roughly be expressed as approximately $\Delta T \approx IVR_{th}$. By substituting the measured 30 K offset and the power dissipation of 1.5 W for this specific device, gives an estimated thermal resistance of $R_{th} \approx 20\ KW^{-1}$. This indicates that the "Device F" outperforms the previously obtained value of $31\ KW^{-1}$for a "Device E", demonstrating relatively effective thermal mounting within the system block.

Figure 4.16 illustrates the spectra of the "Device F" in continuous wave mode at temperatures of 20 K, 45 K, and 50 K. All spectra were recorded at a supply current of 270 mA. Figure 4.17 shows the spectra at various current value at 20 K. Notably, the single modes remain stable at approximately 2.10 THz across different

temperatures. This observation indicates that the device maintains consistent emission characteristics at the desired frequency throughout the temperature range examined.

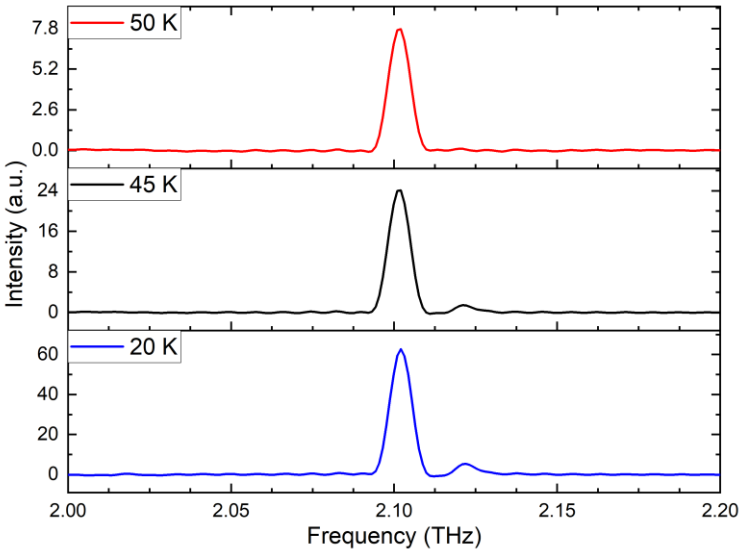

Figure 4.16: Spectra of “Device F” at different temperatures.

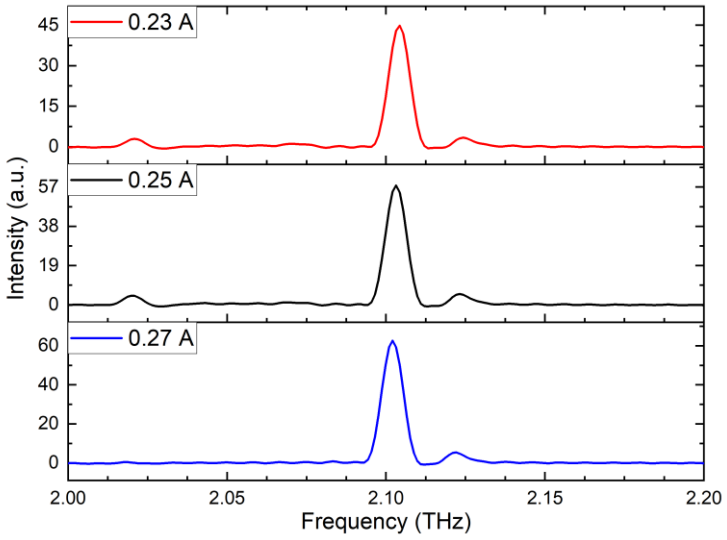

Figure 4.17: Spectra of “Device F” at 20K at different current values.

This single-mode emission is evidence for fundamental waveguide operation. “Device F”, is capable of single mode emission because it was fabricated using Distributed feedback (DFB) grating.

4.6 Conclusions

The chapter presents detailed characterizations of integrated THz QCLs operating at 3.5 THz (Device D), 4.7 THz (Device E), and 2.0 THz (Device F).

The “Device D” demonstrated successful operation in pulsed mode, reaching a maximum operating temperature of 120 K with an output power of ~70 μW. This device is the first Photonic integrated power control QCL incorporated into a waveguide block.

The “Device E” showed pulsed mode operation with a current threshold of 323 mA and peak-power current value of 475 mA at 6 K. Continuous-wave operation was not achieved in either device due to issues related to thermal management. Challenges related to thermal management and soldering issues need to be addressed for continuous-wave operation for “Device D” and “Device E”.

The “Device F” operated effectively at temperatures up to 60 K in CW mode, with an electrical power consumption of approximately 1.5 W and THz output power of 300 μW. It achieved an emission frequency of 2.102 THz with stable single modes across different temperatures. This device is the First QCL in IEEE standard waveguide – single-mode operation.

Waveguide integration demonstrated across entire QCL operating range (2.0 to 4.7 THz). Challenges related to thermal management and soldering issues need to be addressed for continuous-wave operation.

Bibliography

[1] A. Valavanis et al., ‘Waveguide-integrated THz Quantum-Cascade Lasers for Atmospheric-Research Satellite Payloads’, in 2019 IEEE MTT-S International Wireless Symposium (IWS), Guangzhou, China: IEEE, May 2019, pp. 1–3. doi: 10.1109/IEEE-IWS.2019.8803875.

[2] T. Hori and N. Hiromot, ‘Characteristics of a far-infrared molecular laser optically pumped by a high-power CO2 laser’, Int. J. Infrared Millim. Waves, vol. 13, no. 4, pp. 483–496, Apr. 1992, doi: 10.1007/BF01010707.

[3] C. Walther, M. Fischer, G. Scalari, R. Terazzi, N. Hoyler, and J. Faist, ‘Quantum cascade lasers operating from 1.2to1.6THz’, Appl. Phys. Lett., vol. 91, no. 13, p. 131122, Sep. 2007, doi: 10.1063/1.2793177.

[4] M. Wienold et al., ‘Frequency dependence of the maximum operating temperature for quantum-cascade lasers up to 5.4 THz’, Appl. Phys. Lett., vol. 107, no. 20, p. 202101, Nov. 2015, doi: 10.1063/1.4935942.

[5] H. Richter, M. Wienold, L. Schrottke, K. Biermann, H. T. Grahn, and H.-W. Hübers, ‘4.7-THz Local Oscillator for the GREAT Heterodyne Spectrometer on SOFIA’, IEEE Trans. Terahertz Sci. Technol., vol. 5, no. 4, pp. 539–545, Jul. 2015, doi: 10.1109/TTHZ.2015.2442155.

[6] D. J. Hayton et al., ‘A 4.7 THz HEB/QCL heterodyne receiver for STO-2’, in 2014 39th International Conference on Infrared, Millimeter, and Terahertz waves (IRMMW-THz), Sep. 2014, pp. 1–2. doi: 10.1109/IRMMW-THz.2014.6956203.

[7] M. Wienold, A. Semenov, H. Richter, and H.-W. Hübers, ‘OSAS-B: a balloon-borne heterodyne spectrometer for sounding atomic oxygen in the MLT region’, Copernicus Meetings, EGU21-10874, Mar. 2021. doi: 10.5194/egusphere-egu21-10874.

[8] G. Liang et al., ‘Low divergence single-mode surface-emitting concentric-circular-grating terahertz quantum cascade lasers’, Opt. Express, vol. 21, no. 26, pp. 31872–31882, Dec. 2013, doi: 10.1364/OE.21.031872.

[9] N. Yu et al., ‘Designer spoof surface plasmon structures collimate terahertz laser beams’, Nat. Mater., vol. 9, no. 9, Art. no. 9, Sep. 2010, doi: 10.1038/nmat2822.

[10] J. A. Fan et al., ‘Surface emitting terahertz quantum cascade laser with a double-metal waveguide’, Opt. Express, vol. 14, no. 24, pp. 11672–11680, Nov. 2006, doi: 10.1364/OE.14.011672.

[11] M. I. Amanti, M. Fischer, C. Walther, G. Scalari, and J. Faist, ‘Horn antennas for terahertz quantum cascade lasers’, Electron. Lett., vol. 43, no. 10, pp. 573–574, May 2007, doi: 10.1049/el:20070450.

[12] A. W. M. Lee, Q. Qin, S. Kumar, B. S. Williams, Q. Hu, and J. L. Reno, ‘High-power and high-temperature THz quantum-cascade lasers based on lens-coupled

metal-metal waveguides', Opt. Lett., vol. 32, no. 19, pp. 2840–2842, Oct. 2007, doi: 10.1364/OL.32.002840.

[13] M. C. Wanke et al., 'Monolithically integrated solid-state terahertz transceivers', Nat. Photonics, vol. 4, no. 8, Art. no. 8, Aug. 2010, doi: 10.1038/nphoton.2010.137.

[14] W. Miao et al., 'Demonstration of a fully integrated superconducting receiver with a 2.7 THz quantum cascade laser', Opt. Express, vol. 23, no. 4, pp. 4453–4458, Feb. 2015, doi: 10.1364/OE.23.004453.

[15] A. Valavanis et al., 'Mechanically robust waveguide-integration and beam shaping of terahertz quantum cascade lasers', Electron. Lett., vol. 51, no. 12, pp. 919–921, 2015, doi: 10.1049/el.2015.1137.

[16] 'Antenna Theory: Analysis and Design, 4th Edition | Wiley', Wiley.com. Accessed: Jun. 20, 2023.

[17] L. Daniyan et al., 'HORN ANTENNA DESIGN: THE CONCEPTS AND CONSIDERATIONS', May 2014.

[18] J. F. Johansson and N. D. Whyborn, 'The diagonal horn as a sub-millimeter wave antenna', IEEE Trans. Microw. Theory Tech., vol. 40, no. 5, pp. 795–800, May 1992, doi: 10.1109/22.137380.

[19] B. N. Ellison et al., '3.5 THz quantum-cascade laser emission from dual diagonal feedhorns', Int. J. Microw. Wirel. Technol., vol. 11, no. 9, pp. 909–917, Nov. 2019, doi: 10.1017/S175907871900028X.

[20] L. Schrottke et al., 'Quantum-cascade lasers as local oscillators for heterodyne spectrometers in the spectral range around 4.745 THz', Semicond. Sci. Technol., vol. 28, no. 3, p. 035011, Feb. 2013, doi: 10.1088/0268-1242/28/3/035011.

[21] 'IEEE Standard for Rectangular Metallic Waveguides and Their Interfaces for Frequencies of 110 GHz and Above—Part 2: Waveguide Interfaces', IEEE Std 17852-2016, pp. 1–22, Sep. 2016, doi: 10.1109/IEEESTD.2016.7564020.

[22] I. E. Gordon et al., 'The HITRAN2020 molecular spectroscopic database', J. Quant. Spectrosc. Radiat. Transf., vol. 277, p. 107949, Jan. 2022, doi: 10.1016/j.jqsrt.2021.107949.

[23] 'IEEE Std 1785.1-2012: IEEE Standard for Rectangular Metallic Waveguides and Their Interfaces for Frequencies of 110 GHz and Above--Part 1: Frequency Bands and Waveguide Dimensions'.

[24] C. Worrall et al., ‘Continuous wave operation of a superlattic quantum cascade laser emitting at 2 THz’, Opt. Express, vol. 14, no. 1, pp. 171–181, Jan. 2006, doi: 10.1364/OPEX.14.000171.

[25] B. S. Williams, S. Kumar, H. Callebaut, Q. Hu, and J. L. Reno, ‘Terahertz quantum-cascade laser at λ≈100 μm using metal waveguide for mode confinement’, Appl. Phys. Lett., vol. 83, no. 11, pp. 2124–2126, Sep. 2003, doi: 10.1063/1.1611642.

[26] E. Nuttall et al., ‘Waveguide integration of a >4.7-THz quantum-cascade laser’, Electron. Lett., vol. 59, no. 2, p. e12703, 2023, doi: 10.1049/ell2.12703.

Chapter 5
Terahertz fast modulation and detection

5.1 Overview

Terahertz detection involves converting terahertz signals into measurable electrical signals, which allow the retrieval of various crucial information, from terahertz waves. This information encompasses aspects like amplitude, phase, spectroscopic features, and polarization. By analysing such data valuable insights can be known between the interactions of terahertz waves with various materials [1], [2].

However, the widespread commercial success of THz sensing and imaging has been limited due to the lack of suitable components in the 300 GHz to 10 THz spectral range. Achieving cost-effective, real-time THz spectroscopy remains a challenge, despite research efforts on sources and detectors. Passive sensors typically rely on detecting thermal radiation emitted by the source/object or radiation reflected from it. However, at THz frequencies, the power levels of ambient radiation are lower compared to the infrared and visible spectral ranges. Opto-electronic approaches, based on lasers operating in the near-infrared or visible range use coherent optoelectronic conversion to and from THz frequencies, which could offer fast imaging systems [3], [4]. Although, these existing detector systems are too bulky [5], [6] and expensive [7], [8]. In terms of detector research, there have been advancements in years with various thermal, photonic and electronic detection concepts. These developments show promising potential for sensitive detection [9].

This chapter will provide an overview of different detectors in the terahertz region, with a specific focus on the TeraFET detector. The chapter will also discuss the

investigation and application of the TeraFET detector for fast THz detection and modulation using a current modulation scheme. Additionally, it will include a comparative analysis between the TeraFET and bolometer detectors, emphasizing the utility of the TeraFET for rapid spectrum scanning and gas spectroscopy.

5.2 Terahertz detectors

5.2.2 Bolometer

Semiconductor bolometers are widely used due to their enhanced sensitivity and reduced thermal noise when operated at low temperatures. Typically, these bolometers are cooled using liquid helium, which enables them to function at temperatures around 4.2 K, the standard operating temperature. However, it is possible to achieve even higher sensitivity and lower noise levels by lowering the temperature to 2 K through a process of pumping away the evolving helium gas, resulting in a lower boiling temperature [10], [11], [12].

In operation, the bolometer element is exposed to radiation by concentrating it through a cone or series of cones. Filters are then utilized to eliminate higher frequency radiation and maintain the low temperature necessary for accurate measurements [12].

Figure 5.1 (Left) illustrates a simplified model of a bolometer. In this model, a bolometer comprises an absorber connected to a thermistor with resistance (R) and operating at a temperature (T). The coupling between the bolometer and a heat sink is deliberately kept weak, where bolometer temperature (T) $\geq$ heatsink temperature (T_0). Typically, T_0 is referred to as the stage temperature, as it corresponds to the cold stage of the fridge being used when making measurements. The thermal connection between the bolometer and the heat sink has a length (L) and a static thermal conductance (G_s). The bolometer also has a heat capacity of C(T) [13].

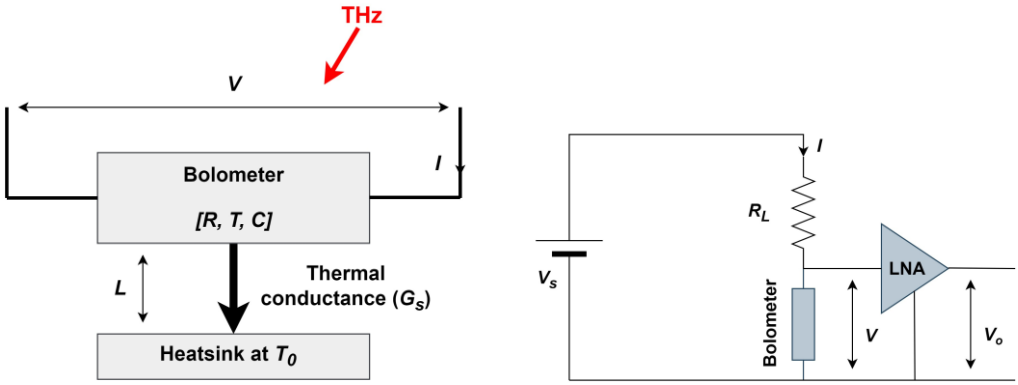

Figure 5.1: (Left) Bolometer schematic diagram. (Right) Electrical connection to the bolometer for THz power measurement.

To achieve the voltage drop across the bolometer, a bias current (I) is passed through the thermistor, creating a voltage, $V = IR$. Figure 5.1 (Right) illustrates a standard electrical bias and measurement circuit for a bolometer. In this setup, a voltage source (V_s) is a source voltage which is supplied to bias the bolometer, typically connected in series with a load resistance (R_L). The voltage across the bolometer is then detected using a low-noise voltage amplifier (LNA) [13].

When setting up the thermal link to the cold bath, there is a delicate balance between sensitivity (requiring a weaker thermal link) and response time (requiring a stronger thermal link), response time is typically $C(T)/G_s$. Typical semiconductor bolometers have a responsivity of approximately 107 V/ W and a Noise Equivalent Power (NEP) of around 10^{-14} W/√Hz [12].

5.2.2 Pyroelectric detector

Pyroelectric detectors work by utilizing pyroelectric materials, which have an electric polarization that is affected by temperature. As the material absorbs heat, its temperature increases, resulting in a change of the electric field, across opposite faces of the material. This change is then observed by including the material as the dielectric in a capacitor.

In practical application, a reverse current is introduced across the pyroelectric material to balance out the effects of surface charge accumulation. By this process, the temperature can be determined which helps to capture the amount of THz signal. Pyroelectric detectors commonly use materials, like triglycine sulfate (TGS) deuterated triglycine sulfate (DTGS) lead zirconate titanate (PZT) barium strontium titanate (BST) and lithium tantalate (LT). These detectors typically have a responsivity of ~103 V/W and their Noise Equivalent Power (NEP) is usually ~ 10^{-9} W/√Hz [12], [14], [15].

Pyroelectric detectors also serve as essential metrology standards. A prime example is the large-area thin-film pyroelectric detector which is manufactured using a polyvinylidene fluoride (PVDF) foil coated with metal oxide on both sides. Extensive characterization at a frequency range of 0.30–30 THz utilizing three radiation sources; synchrotron, laser and blackbody radiation. The spectral response of this detector was consistently observed to be flat throughout the range. However, pyroelectric detectors are relatively compact and robust but may be less sensitive. One noteworthy limitation is their response time requiring several hundred milliseconds to accurately register changes [12].

5.2.3 Photoconductive antenna

The photoconductive detector, also known as a photoconductive switch or photoconductive antenna, is an essential component in terahertz time-domain spectroscopy (TDS). Its operation relies on monitoring the conductivity of a semiconductor material. In the absence of bias, no photocurrent is generated across the device's terminals. However, when an optical pulse initiates the generation of electron-hole pairs (photogeneration or photoinjection), there is still no current produced. The crucial step occurs when terahertz radiation falls on the photoconductive device, creating an asymmetric electric field that induces a flow of current. This photocurrent is directly proportional to the amplitude of the terahertz electric field, and by adjusting the time delay of the probe pulse relative to the terahertz pulse, phase information can also be obtained [12], [16], [17], [18].

In practical implementation, a lens may be used to focus the beam onto the photoconductive material, as semiconductor photoconductor elements have a significant refractive index mismatch with air. The electrode structure is typically placed on the backside of the material and is commonly made of metals like gold through the evaporation process. The gap between the electrodes is typically in the range of 10 to 100 μm, and the use of thin layers is necessary for broadband detection.

To ensure efficient operation in TDS, the carrier lifetime of the material must be much shorter than the duration of the terahertz pulse, ideally sub-picosecond. This requirement is achieved through the presence of defects in the material. Low-temperature GaAs-based detectors have demonstrated operation at frequencies up to 20 THz because low-temperature GaAs have a high mobility. There are other materials such as InGaAsP:Fe and InGaAs/InAlAs:Be, operating at 1550 nm, which may also be employed [12].

5.2.4 Heterodyne detection

In this technique, the frequency of terahertz emission (f_{THz}) is combined with a reference frequency (f_{LO}) which is generated by a local oscillator. Mainly used local oscillators are the solid-state or gas lasers [12], which have precise frequency and power characteristics required for LO. The combination of terahertz and reference radiation takes place in a non-linear mixer, which produces frequency components corresponding to the sum ($f_{THz} + f_{LO}$) and difference ($f_{THz} - f_{LO}$) of the frequencies. The sum frequency corresponds to the up-conversion of the terahertz signal, while the difference frequency, known as the intermediate frequency, corresponds to the down-conversion and has a frequency in the microwave range. This intermediate frequency can again be down-converted into radio wave frequency (MHz) by using a RF mixer. Usually, this down-conversion is crucial to interface with the instruments used for characterisation of THz radiation. The output amplitude at the intermediate frequency is directly proportional to the original amplitude of terahertz signal [12].

This method is used for coherent detection of continuous-wave (CW) terahertz radiation, which determines the phase information. However, incoherent detection is

much simpler to implement and more commonly used. This technique is well-suited for spectroscopy, as scanning the LO signal reproduces the terahertz spectrum [19].

Various types of mixer are available for this purpose, such as Schottky diodes, superconductor-insulator-superconductors, and hot electron bolometers. Superconductor-insulator-superconductor detectors offer excellent near-quantum limited performance in the 0.3 to 1 THz range, while superconducting hot electron bolometers are preferable at higher frequencies.

Photomixing is another approach used in THz detection in CW system. The reference signal is created by combining two near-infrared CW sources to generate terahertz radiation. This reference signal is then mixed with the terahertz radiation at a photoconductive switch, resulting in a sinusoidal variation of the photocurrent with the phase difference between the terahertz radiation and the reference signal. Photomixing has been successfully demonstrated for imaging at $\leq$ 3 THz [20], [21].

Although the mixing methods are inherently narrowband due to the frequency mixing with the terahertz signal, they exhibit exceptional sensitivity, making them invaluable tools for astronomical observations and finding wide applications in diverse research fields [12].

5.3 TeraFET detectors

5.3.1 Introduction

For a long time, practical terahertz (THz) frequency range detectors have frequently employed thermal detection methods. These thermal detectors offer the advantage of easy calibration and traceability by employing the absorption mechanism for delivering radiation to the sensing element [22] [23]. However, they have certain drawbacks that limit their use, including slow modulation speed, relatively large size, and the requirement for additional filters to accomplish frequency selectivity.

In contrast, there are uncooled devices like the Schottky barrier detector [24], [25] and more recently developed field-effect transistor (FET)-based detectors that make up another class of THz detectors. Due to their fast response time and high sensitivity, both of them are gaining popularity and are thus appealing for use in practical

applications. The ability to produce FET-based detectors in huge arrays is another advantage of advances in integrated circuit technology [26], [27].

A set of TeraFET devices were provided by a collaboration with Goethe University Frankfurt. Their operation is described in detail in [28], [29], [30], [31] and can be summarised briefly as follows.

The key principle behind the efficient operation of TeraFET detectors at frequencies surpassing the transistor cut-off limit relies on exciting damped plasma oscillations in a two-dimensional Electrongas (2DEG) within the transistor channel [28], [29], [30], [31].

In many FETs, the conductivity of the channel can be manipulated by applying a gate potential, denoted as V_{GS}, as shown in Figure 5.2. TeraFETs can serve as detectors for terahertz radiation when an electromagnetic radiation is encountered. Typically, radiation is coupled to the source (S) terminal of the transistor. The drain (D) electrode is capacitively connected to the gate electrode, resulting in a high capacitive overlap between the gate and drain electrodes. This capacitive connection introduces an AC-ground potential at the drain electrode. The radiation modulates the carrier density of the 2DEG channel periodically. The steady state of a current-carrying FET is disrupted by an inherent instability, leading to the growth of plasma waves at terahertz frequencies. Decreasing charge carrier density in the channel leads to a DC potential difference ΔUDS between the source and drain electrodes, with ΔUDS proportional to the THz power ($\Delta UDS \propto P_{THz}$) [32], [33], [34], [35].

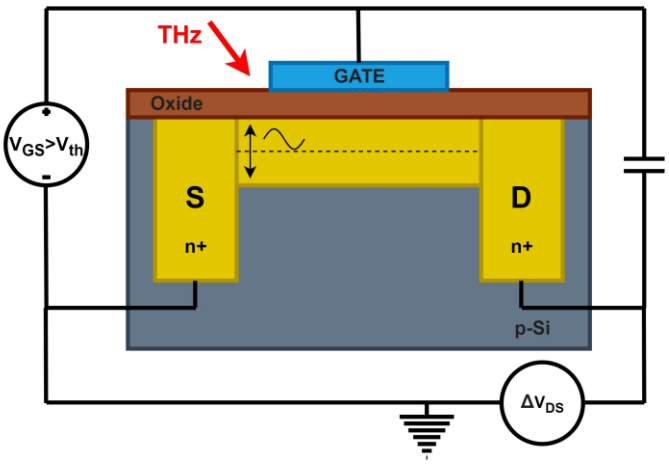

Figure 5.2: Schematic diagram of TeraFET electrical connection.

The fact that the rectifying section of the FET is substantially smaller than the THz wavelength (hundreds of μm) raises a significant obstacle. As a result, in order to define the effective detector area during sensitivity measurement, the THz radiation must be connected to the FET using a grating or intentional/unintentional antennas. For three-terminal transistors, there are no such ready-made solutions available, in contrast to two-terminal devices like Schottky diodes, which may be incorporated into metal waveguides with existing methods [32].

This section aims to explore the performance and capabilities of TeraFET detectors in detail, including IV characteristics, responsivity of the detector, current modulation scheme and time domain LI characterisation.

5.3.2 TeraFET characterisation

One of the critical design considerations is to enhance the efficiency of radiation coupling to the Source electrode of the transistor. To achieve this goal, antennas are utilized (although it is possible without an antenna, but only a small portion of the radiation gets coupled to the channel). The maximum radiation power can be effectively transferred from the antenna to the transistor when the channel impedance $Z_{ch}(\omega)$ (typically in the $k\Omega$ range) and antenna impedance $Z_{Ant}(\omega)$ are conjugately matched (following the maximum power transfer theorem, $Z_{ch}(\omega) = Z_{Ant}*(\omega)$).

The choice of antenna largely depends on the specific application. Some antennas operate across a broad frequency range, such as the Bow-Tie or Log-spiral antennas, while others are designed for narrowband operation, like Patch antennas. The TeraFET shown in Figure 5.3 consists of an array of transistors, each having its designated Patch antennas of specific dimensions, as shown in Table 5.1. This enhanced coupling efficiency around ω_0 makes them well-suited for applications within a narrow frequency range, such as QCL-based spectroscopy.

Table 5.1: FET antennas with their size and detection frequencies.

	B1	B2	B3	B4	B5	B6	B7	B8	B9	B10
Patch (µm)	**40**	**30**	**30**	**30-34**	**18-20**	**13-15**	**12**	**10**	**8**	**6**
THz	**1.36**	**1.63**	**1.63**	**1.63**	**2.35**	**3.4**	**5.34**	**6.26**	**7.2**	**8**

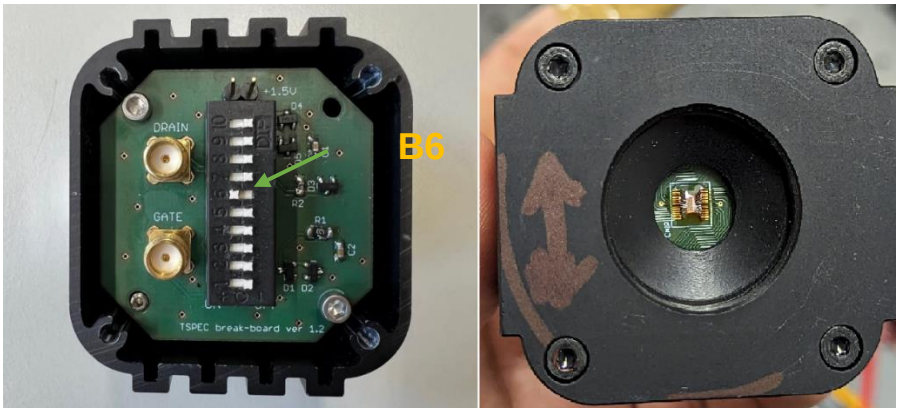

Figure 5.3: (Left) Backside of TeraFET. (Right) Front side of TeraFET.

In Figure 5.3 (Left), the device labelled as "B6" corresponds to the frequency of interest, which is 3.5 THz. The connection marked as "+1.5 V" is for protective purposes. To open the detector, a voltage of +1.6 V is applied. The drain contact receives voltages of +10mV and -10mV. The drain current is measured for both voltage values, while the gate voltage is swept from 0 to 1V. Figure 5.3 (Right) shows the front side of the TeraFET with array of FETs wire-bonded on the chip.

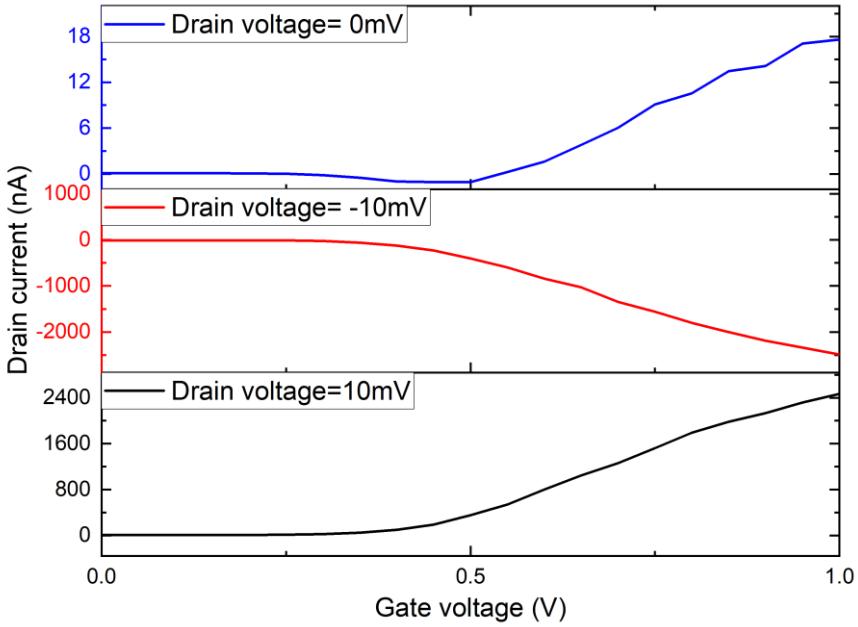

Figure 5.4: TeraFET - Drain IV characteristics as a function of Gate voltage.

Before conducting the actual THz quantum cascade laser (QCL) tests, it was essential to validate the functionality of the TeraFET detector. This validation aimed to ensure that the TeraFET detector has correct electrical characteristics. To achieve this, intentional voltage was applied to the drain terminal. Additionally, a gate signal was introduced to assess whether any drain current could be observed from the drain terminal.

When the gate voltage is set to zero, there should be no detectable drain current. However, when the gate voltage is increased to a specific threshold value, such as 0.55 V in this case, the drain current should become apparent, as shown in Figure 5.4. This behaviour confirms the proper functioning of the FET.

The key objective was to examine the drain current while the gate voltage exceeded the critical threshold. This observation would serve as evidence that the FET is operating above threshold as required to detect THz emissions originating from the QCL. The detection process involves converting these emissions into an electrical signal, represented as a drain voltage. This signal can then be measured using a lock-in amplifier or an oscilloscope.

During the TeraFET characterization, a range of drain voltages was considered, including 10 mV, 0 mV, and -10 mV. The purpose of this characterization was to

demonstrate that the FET functions as expected even in cases where the THz signal is not detected (as seen with 0 mV drain voltage). This characterization helps affirm the robust operation of the FET device.

5.3.3 Pulsed 3.4 THz QCL characterisation

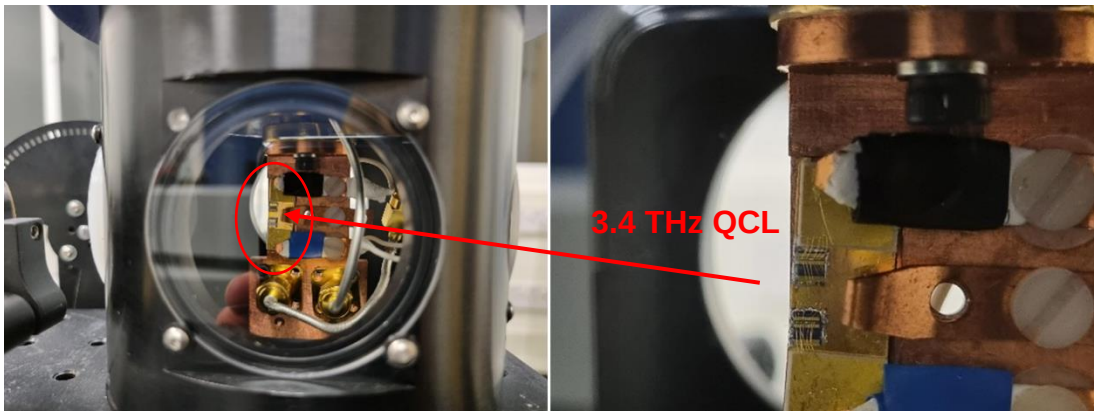

Figure 5.5: SI-SP single-mode 3.4-THz QCL integrated in the ColdEdge closed-cycle cryocooler .

An SI-SP single-mode 3.4-THz QCL served as the radiation source, shown in Figure 5.5. The 3.4 THz QCL discussed in this chapter is “Device G” (specification the QCL devices is outlined in appendix Table B). The device was driven using a Wavelength Electronics QCL1000 LAB dc current source. The current bias through the current source was fixed at 550 mA. The modulation of the device output was achieved using a Keysight signal generator to drive the current source modulation input of 550mA square wave. This made a pulse train starting from 550 mA up to 1.1 A. The current source value was chosen to be the same as the threshold current value of the “Device G”, which is 550 mA. Therefore at 550mA the device is switched off, and at 1.1 A the device is switch on, having its peak power operation.

The device was mounted within a ColdEdge closed-cycle cryocooler, maintaining an operational temperature of 22 K. The emission from the “Device G” was collimated and focused on the detector using a set of off-axis parabolic mirrors.

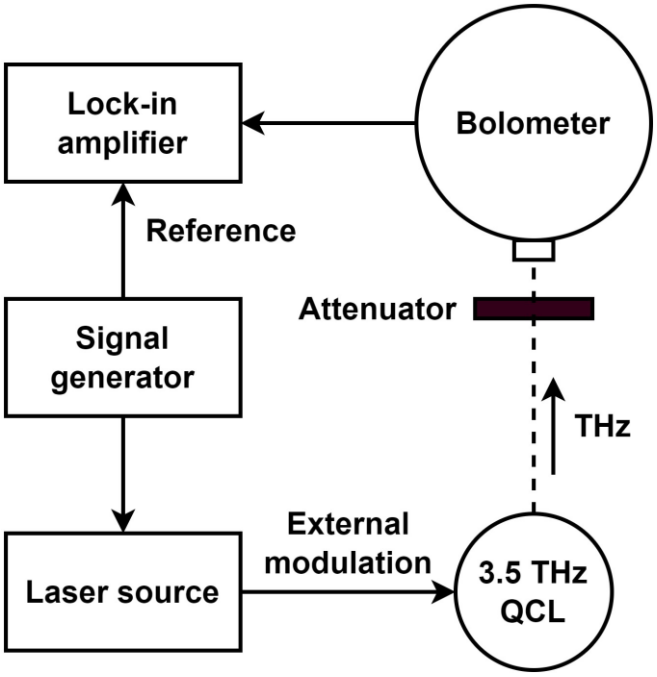

Figure 5.6: Schematic of current modulation setup using bolometer. The Laser source mentioned in the schematic diagram is the Wavelength Electronics QCL1000 LAB current source, used to trigger the QCL.

Initially, a helium-cooled silicon bolometer was used as a detection system to demonstrate current modulation, as shown in Figure 5.6. Additionally, this setup facilitated a direct comparison between the outcomes obtained through current modulation and the established results achieved using a standard optical chopper.

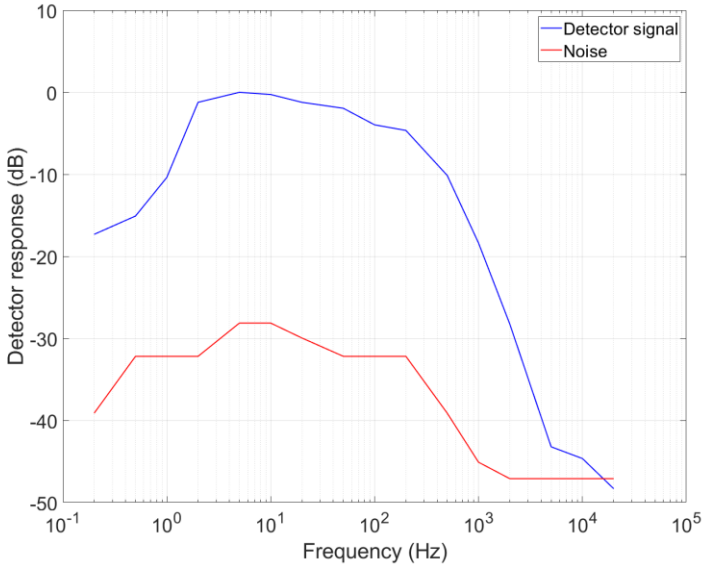

Figure 5.7: Frequency response of bolometer

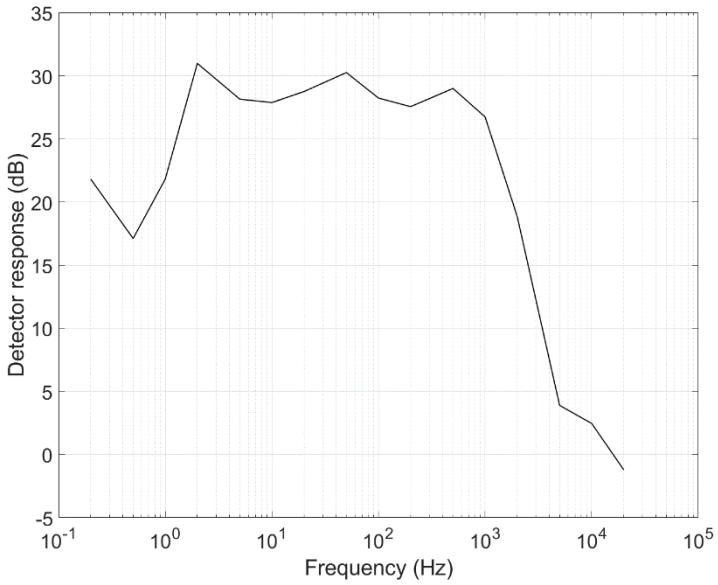

Figure 5.8: SNR of bolometer performance

Figure 5.7 shows the response of the bolometer signals at various modulation frequency ranges. The figure illustrates both the detected signal and the accompanying noise as registered by the bolometer. Looking at the bolometer's response, it is clear that it effectively detects signals when the modulation frequency falls within the range of 2 Hz to 500 Hz. The 3 dB bandwidth is 498 Hz. However, as the modulation frequency surpasses 1 kHz, the bolometer's responsivity decreases. This indicates that

detecting the QCL signal becomes challenging for the bolometer when the modulation frequency exceeds 1 kHz.

Figure 5.8 showcases the signal-to-noise ratio (SNR) of the bolometer performance. Significantly, the signal-to-noise ratio retains its positive performance across the frequency span of 2-500 Hz, maintaining a minimum value of 27 dB. Despite the bolometer's commendable sensitivity, its responsivity diminishes when faced with modulation frequencies surpassing 1 kHz. Figure 5.8 also shows that the bolometer exhibits strong sensitivity, however, its capacity to capture signals becomes compromised when dealing with modulation frequencies higher than 1 kHz. In comparison to bolometers, TeraFETs typically exhibit superior responsivity and are capable of performing well at higher modulation frequencies, reaching up to the MHz range.

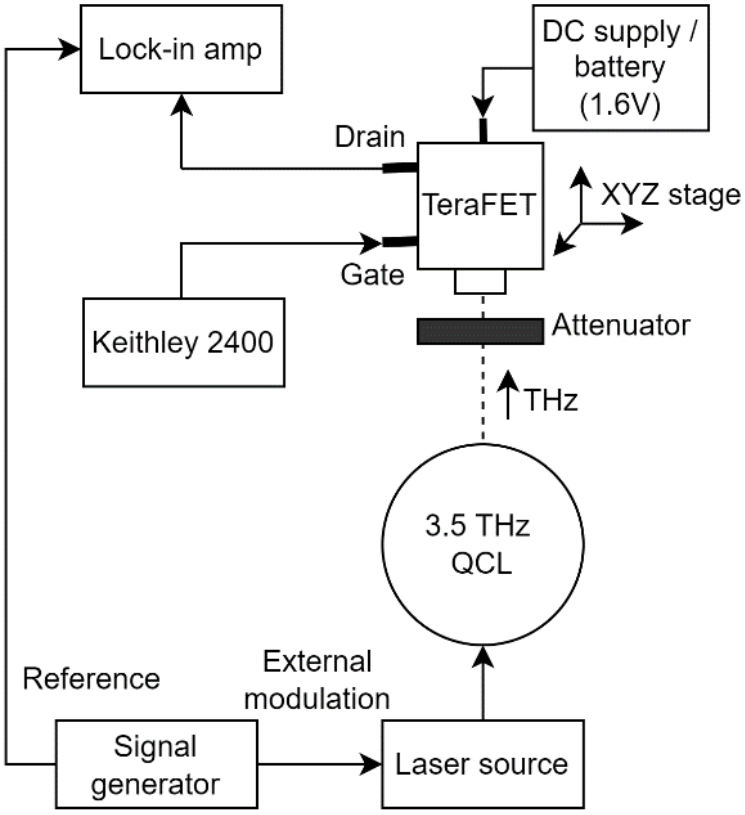

Figure 5.9: Schematic of current modulation setup using TeraFET detector. The Laser source mentioned in the schematic diagram is the Wavelength Electronics QCL1000 LAB current source, used to trigger the QCL.

Figure 5.9 illustrates the schematic representation of the TeraFET, which serves as a detector for detecting THz signals at various modulation frequencies. The QCL utilized in this setup operates through a current modulation technique. The diagram also provides an overview of the electrical connections associated with the TeraFET.

The gate terminal is linked to a Keithley 2400 instrument, which supplies a voltage of 0.55 V. It is important to note that the TeraFET, comprising a collection of transistors, is designed to detect THz signals effectively when the gate voltage exceeds 0.5 V, which is why a gate voltage of 0.55 V has been maintained throughout the experiment.

The drain terminal of the TeraFET is connected to a Lock-in amplifier, which displays the detected THz signal's magnitude, typically measured in millivolts. Attenuators have been strategically placed in front of the detector to safeguard the transistors from potential damage caused by excessive THz signal exposure.

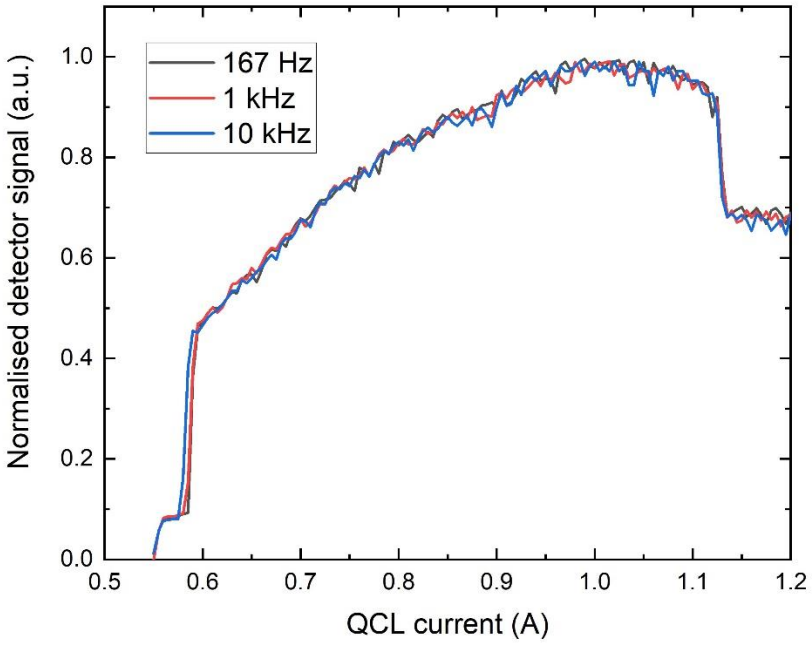

Figure 5.10: Analysis of modulation frequency-dependent LI characteristics utilizing TeraFET detectors.

Figure 5.10 illustrates the LI characteristics of the “Device G” at different square wave modulation frequencies, using a TeraFET detector. The same threshold and shape is seen for each modulation frequency.

The TeraFET detector is shown to acquire signals at higher modulation frequencies, outperforming the bolometer detector. All three modulation frequencies tested—167 Hz, 1 kHz, and 10 kHz - indicate that the responsivity remains unchanged even at higher modulation frequencies.

Moreover, the LI curve at a 10 kHz modulation signal frequency demonstrates that the TeraFET detector can be effectively employed for rapid signal detection and modulation. Thus, time-domain LI measurements are possible using a TeraFET detector.

5.3.4 QCL fast-scan LI characterisation

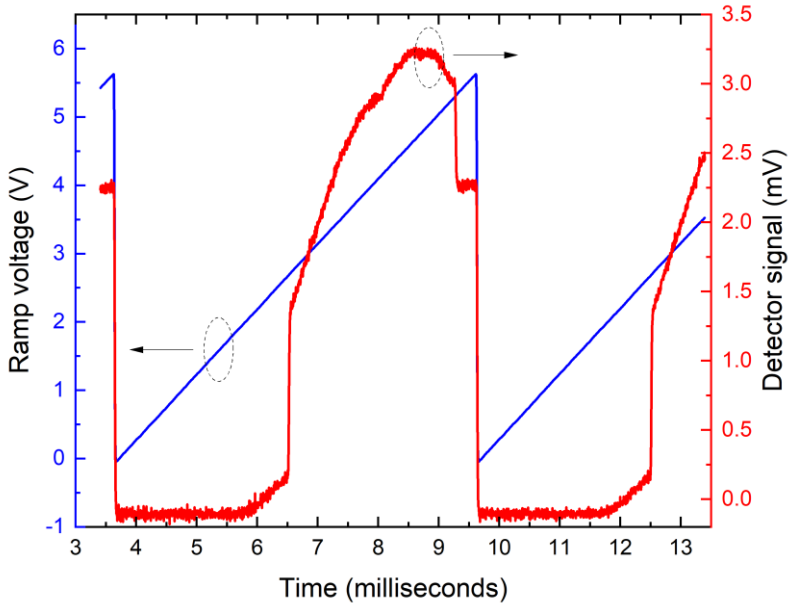

Figure 5.11: Keysight oscilloscope replotted data of screenshot of LI measurement in time domain of “Device G”.

Figure 5.11 show the LI time domain measurements of “Device G”. In the LI measurement setup, a ramp signal was used as a modulation input for the QCL via the Arroyo source. The modulation port of the Arroyo source received the voltage-based

ramp signal through the Keysight signal generator, with the Arroyo laser source set to 0 mA to ensure the absence of a DC signal. This configuration facilitated the generation of a pure ramp signal in terms of current, which was subsequently applied to the QCL. The ramp signal range was chosen from 0 to 5.5 V to align with the LI curve of the QCL, which spans from 0 A to 1.1 A, as shown in Figure 5.8. This was achieved by the modulation port of the Arroyo laser source which has a voltage-to-current conversion rate of 1V to 200 mA.

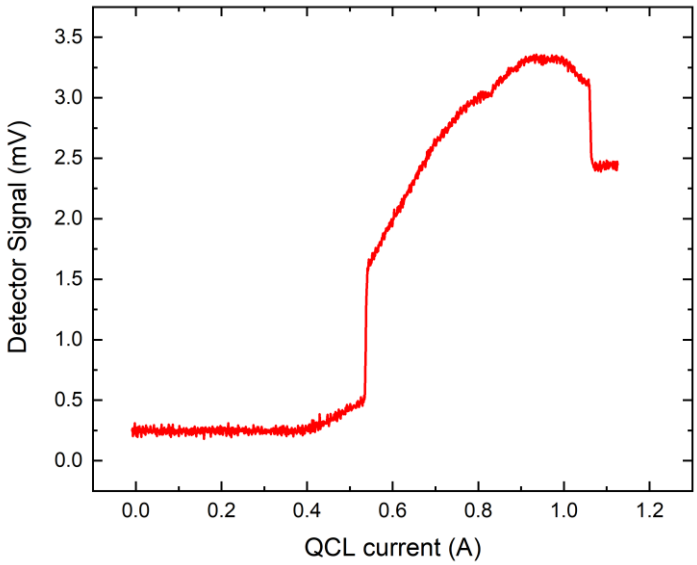

Figure 5.12: Time domain LI measurementof "Device G" – detector signal as a function of ramp current signal.

Figure 5.12 demonstrates a LI measurement of "Device G" conducted in the time domain, using a ramp signal modulation frequency of 10 kHz, which was measured on Keysight oscilloscope. This capability enhances the value of such detectors, as they have potential applications in rapid detection and modulation systems, including satellite communication systems.

5.3.5 Modulation Response

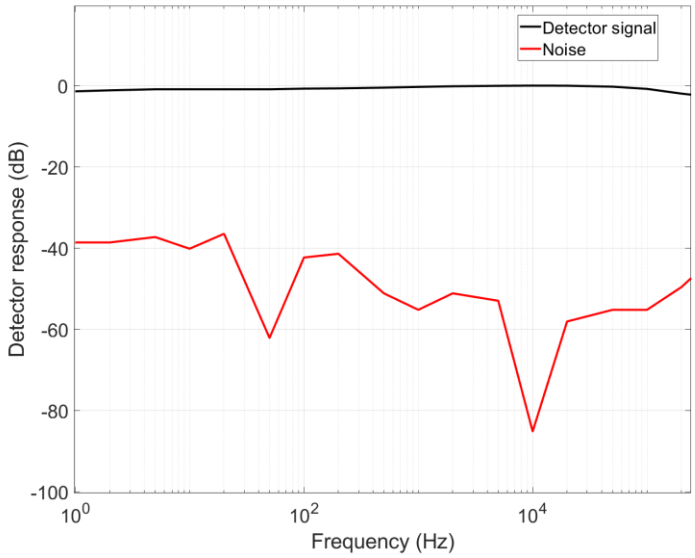

Figure 5.13: Frequency response of TeraFET detector

Figure 5.13 illustrates the response of the TeraFET signals at different modulation frequencies. The graph depicts both the detected signal and the accompanying noise recorded by the TeraFET detector.

TeraFET responsivity demonstrates effective detection when the modulation frequency falls within the 1 Hz to 100 kHz range (3dB bandwidth of 99.99 kHz), a significantly wider range compared to the bolometer (as shown in Figure 5.7). Additionally, the signal strength remains relatively stable within this range, indicating the broad modulation bandwidth of the TeraFET detector.

However, as the modulation frequency exceeds 100 kHz, the detector signal reduces. This drop makes it challenging to detect the QCL THz signal when the modulation frequency surpasses 100 kHz. This limitation arises from the readout electronics within the TeraFET, which impose a bandwidth constraint. Furthermore, Figure 5.13 demonstrates that the optimal modulation frequency for the TeraFET is 10 kHz, as indicated by the lowest noise levels at this frequency, maximizing the SNR.

5.3.6 Patch antenna response

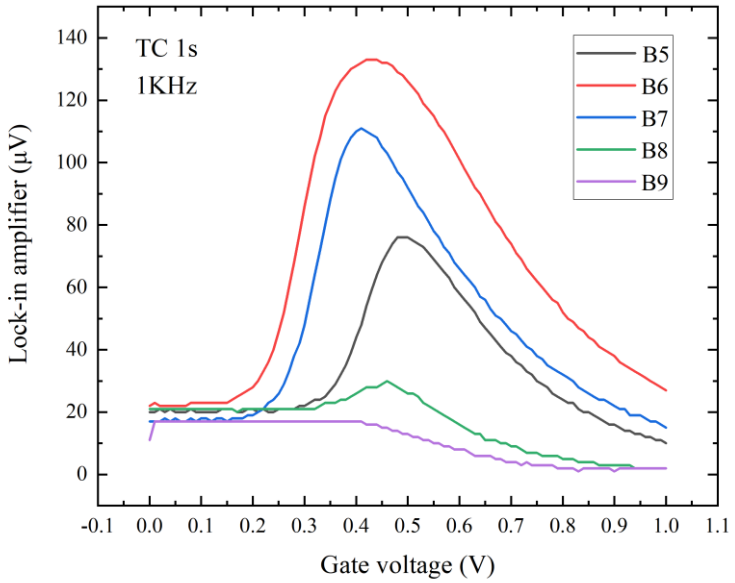

Figure 5.14: Experimental investigation of detector signal response on lock-in amplifier: gate voltage variation from 0 to 1 V for various transistors in TeraFET device

The TeraFET detector comprises multiple Field-Effect Transistors (FETs), each equipped with distinct patch antenna dimensions (Table 5.1). These different antenna sizes give each FET a unique bandwidth, hence enhancing the detector's overall bandwidth.

Figure 5.14 shows the results of a series of measurements conducted to record the detector signal on the lock-in amplifier while manually varying the gate voltage from 0 to 1 V for different transistors within the TeraFET device. These experiments provide insight into how each transistor behaves and performs when activated in the TeraFET. Figure 5.14 illustrates that the B6 transistor exhibits a notably higher recorded detection signal value in comparison to the other transistors. The reason for this difference is that the “Device G” frequency, which was around 3.5 THz, matches well with the B6 transistor antenna response.

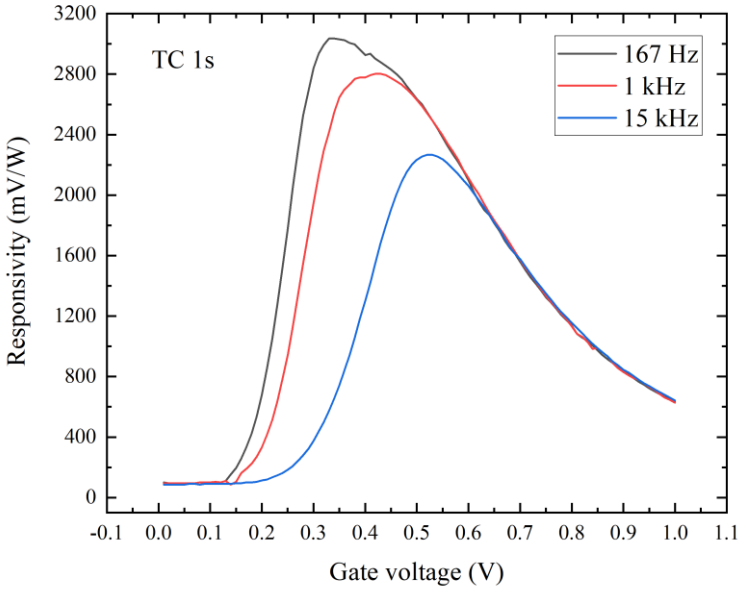

Figure 5.15: TeraFET responsivity vs. gate voltage

Figure 5.15 illustrates the responsivity as a function of gate voltage, at different modulating signal frequencies. It shows in the graph that as the modulating frequency increases, the peak value of the measured responsivity shifts towards the right. This observation demonstrates that for higher modulating frequencies the TeraFET requires a correspondingly higher gate voltage to operate effectively.

As such, a $V_g \geq 0.55\,V$ is required for a flatband modulation response. The responsivity was calculated by the lock-in amplifier detected signal and the pulse power of the "Device G".

$$Responsivity = \frac{Detected\ signal\ (mV)}{QCL\ pulse\ power\ (W)} \tag{5.1}$$

The QCL pulse power was measured using an Ophir power meter and recorded as 3.2 mW. Consequently, the pulse power of the QCL at a 50% duty cycle is determined to be 1.6 mW.

5.4 TeraFET applications

5.4.1 Rapid Spectra Scan

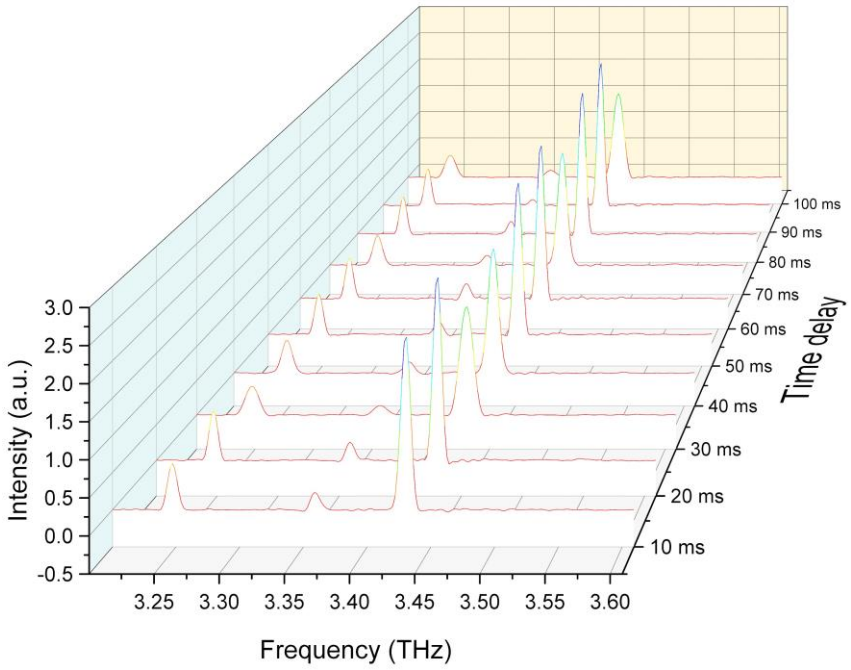

Figure 5.16: Rapid FTIR Scan

Figure 5.16 presents a significant application of the TeraFET in the context of fast THz detection. In this figure, a rapid scan measurement is demonstrated, showing the FTIR spectra of the “Device G” frequency measurements. Each scan was completed in 10 milliseconds, having the QCL current bias of 1 A. A total of 10 scans were performed, taking only 100 milliseconds to plot all 10 scans.

This approach allows for real-time LI curve data measurement in the time-domain on the oscilloscope, as shown in Figure 5.11. Simultaneously, multiple QCL spectra scans can be obtained at different current values by increasing the current using a current modulation scheme with a ramp signal as the modulating signal. This method holds promise for rapid QCL characterisation (e.g. thermal effect in laser).

The potential applications of THz rapid scan technology are primarily found in spectroscopy, especially in investigating the spin dynamics of bulk and surface materials [36]. THz non-linear spectroscopy is also a potential application, where this

technique can be used for the measurement of small and rapid changes in THz absorption [37]. Moreover, the rapid scan method holds a promising approach in the field of fast convolutional neural networks for THz imaging, which achieve high-quality hyperspectral THz images much faster compared to current commercial systems [38].

Unfortunately, attempts to implement this approach were hindered by triggering issues. Specifically, the trigger synchronization problem prevented the proper LI data measurement and the rapid spectra scans. Nevertheless, Figure 5.16 highlights the fast THz signal detection, making it a valuable tool for various THz imaging applications and space research.

5.4.2 Progress towards gas spectroscopy

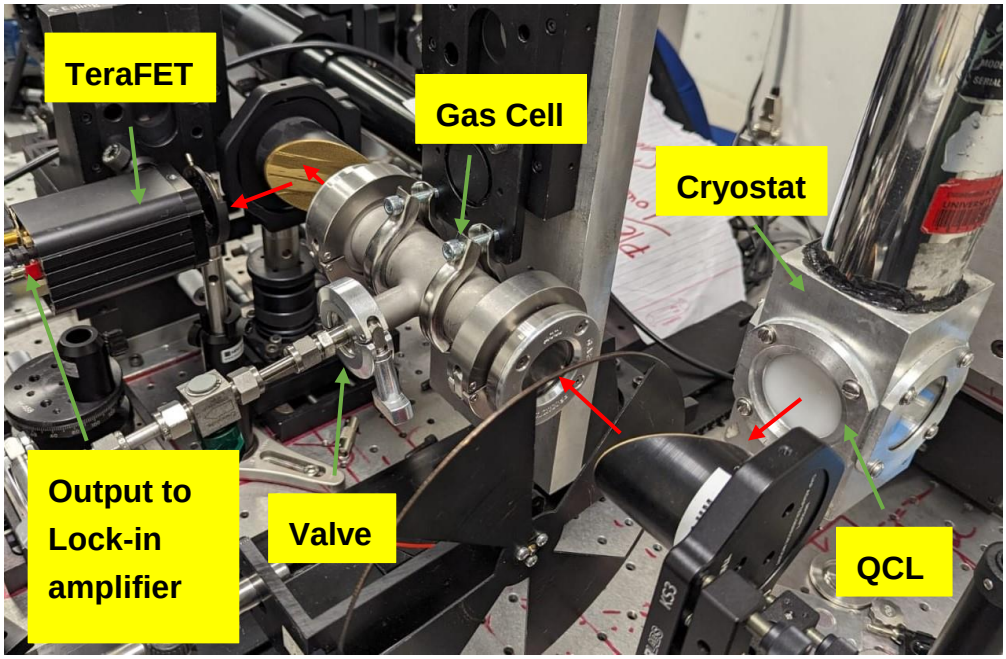

Figure 5.17: THz gas spectroscopy system

It is essential to investigate and demonstrate the suitability of QCLs for detecting the THz spectra of atmospheric gases. The following is a brief illustration of THz gas spectroscopy, where the QCL which is “Device G” serves as the THz source, and the TeraFET functions as the detector. This setup was used to detect the gas line of methanol by passing it through a gas cell, as shown in Figure 5.17. This demonstration

highlights the capability of QCL and TeraFET in detecting specific gas lines such as methanol. This system can be further used for active sensing and gas spectroscopy with atmospheric gases, providing valuable insights into how these gases play a crucial role in climate change.

Additionally, this system could also be used to enable the frequency locking of the THz-QCL using one of the gas lines. Frequency-locked QCLs have wide-ranging applications, including THz imaging and THz communication.

Figure 5.17 illustrates the gas spectroscopy setup used to detect the methanol gas line, while Figure 5.18 (red line) showcase the LI measurement of the "Device G" when the gas cell was under vacuum condition. The device was triggered by an Arroyo laser source, which provided a 10 kHz square signal modulated by a Keysight signal generator. The THz radiation generated by the device was then collimated using a parabolic mirror and directed through the gas cell.

To maintain a vacuum within the gas cell, it was connected to a pump via a valve. A TeraFET detector was then used to detect the THz signal, which was then converted into an electrical signal. This electrical signal was then routed to a lock-in amplifier. To ensure the detection of a pure AC signal, a DC block was introduced at the output of the TeraFET.

The lock-in amplifier recorded the electrical signal readings at various current values while the device operated at a temperature of 50 K, as depicted in Figure 5.16. The observed oscillations in the LI curve are the indicator that an etalon effect is present which is caused by the gas cell.

This effect arises because the windows of the gas cell are oriented perpendicular to the path of the THz signal, which makes it a Fabry-Perot cavity. This orientation causes the THz signal to bounce back and forth inside the gas cell, leading to fluctuations in the LI curve.

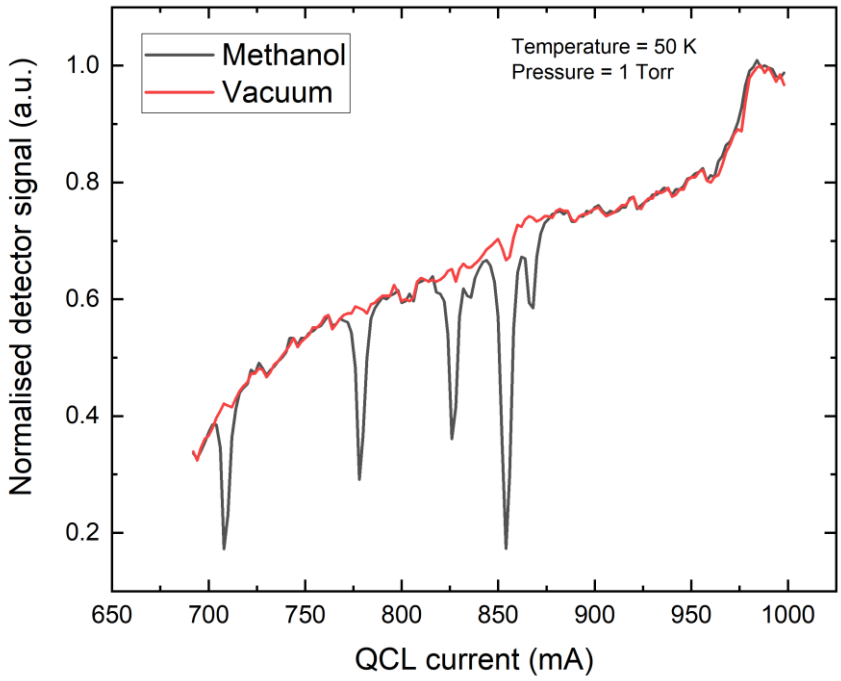

Figure 5.18: LI measurement of "Device G" while gas cell under methanol gas.

Figure 5.18 (black line) provides an illustration of the LI measurement for "Device G" operated within a gas cell filled with methanol gas at a pressure of 1 Torr while maintaining the device temperature at 50 K. The data presented in Figure 5.18 (black line) demonstrates the presence of five prominent gas absorption lines corresponding to methanol gas.

This observation shows that the QCL emission frequency is sensitive to changes in the QCL current bias. As the QCL current bias is varied, the laser frequency undergoes corresponding shifts, eventually aligning with the resonant frequencies associated with the methanol gas absorption lines. Therefore, at specific QCL current values, a sharp drop in QCL output power is observed.

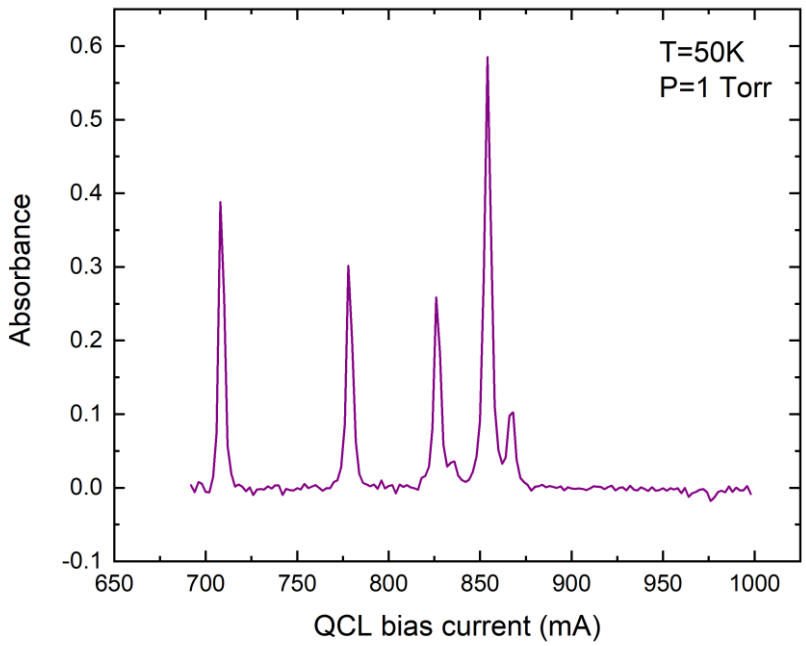

Figure 5.19: Absorbance of Methanol Gas at Specific QCL Current Values

Figure 5.19 shows the absorbance of the methanol gas at specific QCL current values. The Absorbance is calculated in terms of

$$A = log \frac{blank}{sample} \tag{5.2}$$

In equation 5.2, the "blank" is the LI measurement of "Device G" when the gas cell was in a vacuum, and the "sample" is the LI measurement of "Device G" taken when the gas cell was filled with methanol gas at 1 Torr. Keeping device temperature constant at 50 K. The observed absorbance was at five different current values which are ~710mA, ~780mA, ~830mA, ~855mA and, ~870mA. In principle, the data can be compared with catalogued spectral lines and QCL FTIR measurement to determine the line frequencies. However, this is challenging and beyond the scope of this work.

This phenomenon can be attributed to the QCL's capability to precisely target and interact with the methanol gas molecules at their specific absorption frequencies. The resulting sharp decline in QCL power output at these critical QCL current values

underscores the potential utility of this technology for applications involving gas sensing and spectroscopy. Accurate frequency calibration is very challenging because of limited FTIR resolution.

5.5 Conclusions

In this chapter a detailed discussion of terahertz detectors was provided, particularly focusing on the TeraFET detector. Different types of THz detectors such, as bolometers, pyroelectric detectors, photoconductive antennas and heterodyne detection methods were explored.

The TeraFET operation is based on exciting damped plasma oscillations in a two-electron gas (2DEG), present internally in the transistor channel, which allows for rapid THz detection. Its characterizations, including IV characteristics, responsivity, and modulation response, were discussed, demonstrating its performance in comparison to the bolometer.

Furthermore, the TeraFET detector in current modulation schemes and time-domain measurements was explored, demonstrating its potential in rapid scanning and THz gas spectroscopy. This ability sets it apart as a valuable tool in various applications, including satellite communication systems.

Bibliography

[1] C. D. Wilson et al., ‘Luminous infrared galaxies with the submillimeter array: probing the extremes of star formation’, in Science with the Atacama Large Millimeter Array, R. Bachiller and J. Cernicharo, Eds., Dordrecht: Springer Netherlands, 2008, pp. 297–302. doi: 10.1007/978-1-4020-6935-2_52.

[2] M. Chen, Y. Wang, X. Wang, and L. Li, ‘Editorial: Advances in Terahertz Detection and Imaging’, Front. Phys., vol. 10, 2022, Accessed: Sep. 26, 2023.

[3] K. Kawase, Y. Ogawa, H. Minamide, and H. Ito, ‘Terahertz parametric sources and imaging applications’, Semicond. Sci. Technol., vol. 20, no. 7, p. S258, Jun. 2005, doi: 10.1088/0268-1242/20/7/017.

[4] ‘New laser sources benefit terahertz and mid-infrared remote sensing’. Accessed: Sep. 26, 2023.

[5] ‘Hybrid Continuous-Wave Demodulating Multipixel Terahertz Imaging Systems’. Accessed: Sep. 26, 2023.

[6] F. Z. Meng et al., ‘Coherent electro-optical detection of terahertz radiation from an optical parametric oscillator’, Opt. Express, vol. 18, no. 11, pp. 11316–11326, May 2010, doi: 10.1364/OE.18.011316.

[7] ‘Terahertz imaging via electrooptic effect’. Accessed: Sep. 26, 2023. [Online]. Available: https://ieeexplore.ieee.org/document/809019/

[8] N. Oda, ‘Uncooled bolometer-type Terahertz focal plane array and camera for real-time imaging’, Comptes Rendus Phys., vol. 11, no. 7, pp. 496–509, Aug. 2010, doi: 10.1016/j.crhy.2010.05.001.

[9] S. Boppel, A. Lisauskas, and H. G. Roskos, ‘8 - Terahertz array imagers: towards the implementation of terahertz cameras with plasma-wave-based silicon MOSFET detectors’, in Handbook of Terahertz Technology for Imaging, Sensing and Communications, D. Saeedkia, Ed., in Woodhead Publishing Series in Electronic and Optical Materials. , Woodhead Publishing, 2013, pp. 231–271. doi: 10.1533/9780857096494.2.231.

[10] ‘Antenna-Coupled MOSFET Bolometers for Uncooled THz Sensing’. Accessed: Sep. 27, 2023.

[11] M. A. Sumesh et al., ‘Performance-Enhanced Bolometric Terahertz Detectors Based on V2O5 for 15 to 30 THz’, J. Infrared Millim. Terahertz Waves, vol. 38, no. 2, pp. 135–142, Feb. 2017, doi: 10.1007/s10762-016-0326-1.

[12] R. A. Lewis, ‘A review of terahertz detectors’, J. Phys. Appl. Phys., vol. 52, no. 43, p. 433001, Aug. 2019, doi: 10.1088/1361-6463/ab31d5.

[13] M. Hollister, ‘An Introduction to the Thermal Modelling and Characterisation of Semiconductor Bolometers’.

[14] S. A. Kuznetsov, A. G. Paulish, M. Navarro-Cía, and A. V. Arzhannikov, ‘Selective Pyroelectric Detection of Millimetre Waves Using Ultra-Thin

Metasurface Absorbers', Sci. Rep., vol. 6, no. 1, Art. no. 1, Feb. 2016, doi: 10.1038/srep21079.

[15] R. Müller et al., 'Characterization of a Large-Area Pyroelectric Detector from 300 GHz to 30 THz', J. Infrared Millim. Terahertz Waves, vol. 36, no. 7, pp. 654–661, Jul. 2015, doi: 10.1007/s10762-015-0163-7.

[16] D. Seliuta et al., 'Silicon lens-coupled bow-tie InGaAs-based broadband terahertz sensor operating at room temperature', Electron. Lett., vol. 42, no. 14, pp. 825–827, Jul. 2006, doi: 10.1049/el:20061224.

[17] 'Application of Terahertz Pulse Time-Domain Holography for Phase Imaging'. Accessed: Sep. 27, 2023.

[18] 'Photoconductive Terahertz Near-Field Detectors for Operation With 1550-nm Pulsed Fiber Lasers'. Accessed: Sep. 27, 2023.

[19] U. U. Graf, C. E. Honingh, K. Jacobs, and J. Stutzki, 'Terahertz Heterodyne Array Receivers for Astronomy', J. Infrared Millim. Terahertz Waves, vol. 36, no. 10, pp. 896–921, Oct. 2015, doi: 10.1007/s10762-015-0171-7.

[20] I. S. Gregory et al., 'Continuous-wave terahertz system with a 60 dB dynamic range', Appl. Phys. Lett., vol. 86, no. 20, p. 204104, May 2005, doi: 10.1063/1.1935032.

[21] K. J. Siebert et al., 'Continuous-wave all-optoelectronic terahertz imaging', Appl. Phys. Lett., vol. 80, no. 16, pp. 3003–3005, Apr. 2002, doi: 10.1063/1.1469679.

[22] F. Simoens and J. Meilhan, 'Terahertz real-time imaging uncooled array based on antenna- and cavity-coupled bolometers', Philos. Trans. R. Soc. Math. Phys. Eng. Sci., vol. 372, no. 2012, p. 20130111, Mar. 2014, doi: 10.1098/rsta.2013.0111.

[23] R. Müller, W. Bohmeyer, M. Kehrt, K. Lange, C. Monte, and A. Steiger, 'Novel detectors for traceable THz power measurements', J. Infrared Millim. Terahertz Waves, vol. 35, no. 8, pp. 659–670, Aug. 2014, doi: 10.1007/s10762-014-0066-z.

[24] 'Advances in schottky rectifier performance'. Accessed: Sep. 27, 2023.

[25] C. Sydlo, O. Cojocari, D. Schçnherr, T. Goebel, P. Meissner, and H. L. Hartnagel, 'Fast THz detectors based on InGaAs Schottky Diodes', Frequenz, vol. 62, no. 5–6, pp. 107–110, Jun. 2008, doi: 10.1515/FREQ.2008.62.5-6.107.

[26] A. Lisauskas et al., ‘Exploration of Terahertz Imaging with Silicon MOSFETs’, J. Infrared Millim. Terahertz Waves, vol. 35, no. 1, pp. 63–80, Jan. 2014, doi: 10.1007/s10762-013-0047-7.

[27] J. Zdanevičius et al., ‘Camera for High-Speed THz Imaging’, J. Infrared Millim. Terahertz Waves, vol. 36, no. 10, pp. 986–997, Oct. 2015, doi: 10.1007/s10762-015-0169-1.

[28] W. Knap et al., ‘Nonresonant detection of terahertz radiation in field effect transistors’, J. Appl. Phys., vol. 91, no. 11, pp. 9346–9353, May 2002, doi: 10.1063/1.1468257.

[29] W. Knap et al., ‘Plasma wave detection of sub-terahertz and terahertz radiation by silicon field-effect transistors’, Appl. Phys. Lett., vol. 85, no. 4, pp. 675–677, Jul. 2004, doi: 10.1063/1.1775034.

[30] A. Lisauskas, U. Pfeiffer, E. Öjefors, P. H. Bolìvar, D. Glaab, and H. G. Roskos, ‘Rational design of high-responsivity detectors of terahertz radiation based on distributed self-mixing in silicon field-effect transistors’, J. Appl. Phys., vol. 105, no. 11, p. 114511, Jun. 2009, doi: 10.1063/1.3140611.

[31] M. I. Dyakonov, ‘Generation and detection of Terahertz radiation by field effect transistors’, Comptes Rendus Phys., vol. 11, no. 7, pp. 413–420, Aug. 2010, doi: 10.1016/j.crhy.2010.05.003.

[32] E. Javadi, D. B. But, K. Ikamas, J. Zdanevičius, W. Knap, and A. Lisauskas, ‘Sensitivity of Field-Effect Transistor-Based Terahertz Detectors’, Sensors, vol. 21, no. 9, Art. no. 9, Jan. 2021, doi: 10.3390/s21092909.

[33] J. Zdanevičius et al., ‘Field-Effect Transistor Based Detectors for Power Monitoring of THz Quantum Cascade Lasers’, IEEE Trans. Terahertz Sci. Technol., vol. 8, no. 6, pp. 613–621, Nov. 2018, doi: 10.1109/TTHZ.2018.2871360.

[34] A. Satou, V. Ryzhii, and A. Chaplik, ‘Plasma oscillations in two-dimensional electron channel with nonideally conducting side contacts’, J. Appl. Phys., vol. 98, no. 3, p. 034502, Aug. 2005, doi: 10.1063/1.1993756.

[35] M. Dyakonov and M. Shur, ‘Shallow water analogy for a ballistic field effect transistor: New mechanism of plasma wave generation by dc current’, Phys. Rev. Lett., vol. 71, no. 15, pp. 2465–2468, Oct. 1993, doi: 10.1103/PhysRevLett.71.2465.

[36] ‘THz Frequency Rapid Scan – Electron Spin Resonance spectroscopy for spin dynamics investigations of bulk and surface materials (THz-FRaScan-ESR) | THz-FRaScan-ESR Project | Fact Sheet | H2020’, CORDIS | European Commission. Accessed: Feb. 26, 2024. [Online]. Available: https://cordis.europa.eu/project/id/714850

[37] C. Hoberg, P. Balzerowski, and M. Havenith, ‘Integration of a rapid scanning technique into THz time-domain spectrometers for nonlinear THz spectroscopy measurements’, AIP Adv., vol. 9, no. 3, p. 035348, Mar. 2019, doi: 10.1063/1.5080653.

[38] R. I. Stantchev, K. Li, and E. Pickwell-MacPherson, ‘Rapid Imaging of Pulsed Terahertz Radiation with Spatial Light Modulators and Neural Networks’, ACS Photonics, vol. 8, no. 11, pp. 3150–3155, Nov. 2021, doi: 10.1021/acsphotonics.1c00634.

Chapter 6
Conclusions and Future work

6.1 Conclusions

The work presented in this thesis serves as the foundation for the development and integration of THz technology in space research applications. The primary focus of the study was on terahertz quantum cascade lasers exploring various aspects including theory, fabrication, characterization, power locking and their waveguide integration as local oscillators for the KEYSTONE satellite mission. Additionally, the research also emphasized the potential of THz detectors, specifically TeraFET detectors for fast detection and their utilization in THz gas spectroscopy. These findings have significant implications for applications such as atmospheric sensing, Earth observation and the investigation of celestial objects.

In general this doctoral research has made advancements in the field of terahertz technology bringing opportunities, for scientific exploration and laying the foundation for future progress in space research. Additionally, this research project has provided a chance to enhance and expand partnerships between research teams at Leeds, Rutherford Appleton Laboratory (RAL Space), Goethe University Frankfurt and engagement with the UK Space Agency (UKSA) and the European Space Agency (ESA).

The thesis on the present work on ‘Integrated Terahertz Quantum Cascade Laser Systems for Space Research’ has been divided into the following main chapters.

In Chapter 2, QCL theory, their fabrication process and characterisation were explored. This included discussing the design of quantum wells, various QCL structures and waveguide design. The main goal of this chapter was to fabricate QCL

devices lasing roughly at frequencies of 4.7 THz and 3.5 THz, which are “Device A” “Device B” respectively. Initially, a 2.0 THz QCL was not part of the proposed satellite mission. It was later included because of the advantages it offers in atmospheric chemistry within that specific THz frequency range. The focus in Chapter 2 was to make progress in developing QCLs with specification; power output >1 mW, single mode frequency, CW mode operation and lasing above 50K temperature. However, these requirements were not completely fulfilled due to several factors, including challenges with fabricating ridges which limited the QCLs operation to high temperatures and lased in pulse mode only. Another issue arose from background doping during QCL growth which affected the lasing process.

Although, the QCL devices described in Chapter 2 (Device A & Device B) have the potential to meet temperature requirements as per LO need for the KEYSTONE satellite, as demonstrated in Table 6.1. This shows that these devices could be effective in achieving the desired thermal performance.

Chapter 3 focused on the development of power-locking techniques for THz QCLs using “Device C”. The chapter introduced a novel approach using a photonic integrated circuit composed of a racetrack resonator coupled to a QCL ridge. The chapter presented the fabrication process of the QCL-RTR device and discussed the implementation of power-locking systems using PI and FPGA-based PID controllers. The work presented in Chapter 3 holds the potential to significantly enhance the performance of high-resolution spectroscopic systems. This was crucial as the mechanical vibration on the satellite can create fluctuation in the optical output power of the QCL. This could tamper the output amplitude of the front-end of the KEYSTONE receiver. Typically, for satellite-based missions, the optical power should be stable at least for 300 seconds, and specifically for the KEYSTONE satellite, the amplitude fluctuation is limited to 1% of the output power. This was accomplished in Chapter 3 with power-locking for > 600 seconds, and with amplitude fluctuation of 0.12 % of output power, which is desirable for KEYSTONE satellite. Other LO requirements for KEYSTONE were also achieved, including continuous wave operation and temperature performance, as shown in Table 6.1. However, a challenge encountered with “Device C” was its significantly low power, which made is unable to measure the THz power. Thus, the LO requirement for THz power above 10mW

was not achieved. Nonetheless, progress in QCL output power was demonstrated with "Device F", as discussed in the following paragraph. The power-lock method described in this chapter does have a drawback; it has a slow response time because of the speed of the optical chopper (220 Hz). This slower response time can affect the detection speed of THz signals. To overcome this limitation some techniques can be explored, such as the use of current modulation or the use of a DC-coupled detector, like a TeraFET (discussed in Chapter 5). By utilizing current modulation fast response times with frequencies reaching up to 100 kHz can be achieved. This improvement allows for a more efficient power-locking mechanism.

Chapter 4 successfully demonstrated techniques for integrating 2, 3.5 and 4.7 THz QCLs, which are "Device D", "Device E" and "Device F", using waveguide cavities and diagonal feedhorns, and discusses their characterisation. This was a significant step toward developing a practical prototype LO for use in the KEYSTONE satellite mission. However, it is important to note that both the "Device D" and "Device E" did not achieve CW lasing due to two primary reasons. Firstly, while integrating the waveguide block with the QCL, increased thermal resistance is observed, which prevented CW lasing. Another reason might be because of the formation of standing waves within the waveguide due to issues with the waveguide fabrication. The dimensions of the waveguide were on the micrometre scale, which made it harder to fabricate. In fact, in the case of the "Device D", observable harmonics were observed which indicated the presence of standing waves inside the waveguide, resulting in a reduction in optical output power.

However, the LO requirements of waveguide integration, single mode emission, continuous wave operation, electrical power consumption and temperature performance was achieved for "Device F", as shown in Table 6.1. Device F showed excellent performance when used in CW mode, even at temperatures above 50 K and exhibit a single mode frequency. This QCL device has the potential to serve as a LO for the KEYSTONE satellite mission, meeting most of the requirements. One possible reason is that the thermal resistance of "Device F", was at a lower scale ($20\ KW^{-1}$) which made it possible for operating in CW mode and achieved lower electrical power consumption. One more advantage of "Device F", is that it operates in single mode, this was because the QCL was fabricated using Distributed feedback (DFB) grating.

Specific grating parameters were considered including grating pitch and length of grating, which gave a single mode operation.

The chapter 4 also highlights the challenges in generating sufficient power at supra THz frequencies, and explored how QCL-based LO devices can address these challenges. The optical output power of "Device F" was relatively low (~ 40 µW), whereas LOs typically require at least 10 mW of power. Despite this limitation, it still marked progress and holds promise for further enhancements. Increasing the QCL ridge length could potentially boost its optical output power. Additionally achieving a very low surface roughness on the heatsink adapter (which connects the QCL to the cryostat finger) could greatly improve its heat dissipation abilities and overall performance efficiency. This improvement will reduce the electrical power consumption of QCL devices. Specifically, for "Device F", where the electrical power consumption was 1.7 W. However, this could be reduced to 1 W with improved heat dissipation, which is require for KEYSTONE LO. Lastly optimising the coupling between the QCL and waveguide might significantly reduce insertion loss within the cavity.

In chapter 5, various THz detectors were explored, specifically focusing on TeraFET detectors and their applications in detection and modulation. The aim of this chapter was to characterise the TeraFET detector and investigate its capabilities for fast THz modulation and detection. This ability holds potential for a variety of applications, such as achieving rapid spectrum scans and performing THz gas spectroscopy used in atmospheric chemistry. Additionally, the chapter highlights the possibility of achieving rapid power-locking of QCL by using the TeraFET detector. Furthermore, another objective was to demonstrate progress in frequency locking, which involves locking the QCL frequency with the help of a gas line. Such a power and frequency-locking scheme would be highly desirable for LO-based QCL in the KEYSTONE satellite mission, specifically for improving the QCL frequency drift and the linewidth of the QCL, which are required for LO.

One of the challenges faced during this work was aligning the emission of THz radiation from the QCL ("Device G") with the small-sized patch antennas of the TeraFET detector, which have dimensions in the range of a few micrometres. To address this problem, developing an improved version of the TeraFET could be

considered. This upgraded version would include a Winston cone lens which would make it easier to align with the patch antenna and simplify the process.

Table 6.1: Representation of various LO requirement for KEYSTONE, and how many of them are achieved in this thesis.

	Accomplished
	Nearly complete
	In progress

Requirements	Specification	Outcome
Cooling Temperature	< 100 K	Achieved (All devices)
THz Power Requirement	> 10 mW	In progress – increasing the QCL cavity length will improve the THZ power
LO Type	Waveguide Integrated	Achieved (Devices D, E, F)
Emission	Single-Mode	Achieved (Device F)
Operation Mode	Continuous-Wave	Achieved (Devices C, F)
QCL short-term frequency drift	50 ppm/K	Achieved (Devices C, D, E, & F) Typical QCL has a frequency shift in MHz range
QCL amplitude stability	1% of output power	Achieved (Devices C)
QCL integrated linewidth	0.1 MHz	In progress – Typical QCL has a linewidth in kHz range
QCL Power dissipation	1 W	1.7 W for Device F

The QCL frequency drift and the QCL linewidth are the crucial parameters for LO. The QCL frequency drift for LO should be 50 ppm/K, which means if a QCL emitting frequency of 3.5 THz, then the QCL frequency drift will be ~175 MHz. However, typical QCL frequency drift is in order of couple of MHz [1]. Similarly, the linewidth of typical QCL is in the range of kHz [2]. Therefore, the LO requirement regarding QCL frequency drift and QCL linewidth is not a concern. Although, it is challenging to measure the precise linewidth of the QCL as the linewidth of each Fabry–Pérot mode is limited by the resolution of the spectrometer.

Overall, the thesis presents a significant advancement in space research by introducing and integrating THz QCLs as local oscillators for KEYSTONE satellite missions. The use of QCL devices in space research represents progress for several reasons.

Firstly they cover terahertz frequencies filling a gap between microwaves and infrared radiation. These high-power THz QCLs enable researchers to analyse and explore the characteristics of new properties of celestial objects. Moreover, their compact size and low power consumption make them ideal for space applications that prioritize weight, volume and power restrictions. Additionally, QCLs allow the emission of multiple photons through intersubband transitions resulting in enhanced brightness and output power.

This feature is particularly advantageous for space-based observations that require strong data acquisition. The thesis also introduces power-locking techniques for THz QCLs using a photonic integrated circuit - a first-ever power-locking scheme that eliminates the need for external components. Maintaining power output is vital to ensure reliable measurements, this scheme goes hand-in-hand with the demands of satellite applications aiming for compact and lightweight payloads.

The thesis also demonstrates the waveguide integration achieved across the entire operating range of typical QCL devices, from 2.0 to 4.7 THz. It also marks the first QCL integrated with photonic circuit in the waveguide block. Moreover, the thesis demonstrates the first IEEE standard waveguide integrated QCL operating in single mode and in continuous wave mode.

Finally, the thesis presents a method for analysing atmospheric gases using terahertz detectors and QCLs through spectroscopy. This technique enables researchers to examine the composition of the atmosphere by studying the absorption lines of certain gases, which contributes to a better understanding of Earth’s climate, atmospheric chemistry and space weather. Additionally, the thesis discusses the challenges and solutions involved in integrating QCLs into space systems. It explores techniques, like metallic waveguide cavities and diagonal feedhorns that facilitate integration of QCLs into satellite payloads without requiring extra optics.

6.2 Future work

The thesis proposed several possibilities for exploration in terahertz technology and its applications in space science. These opportunities include boosting the output power of QCL to meet the demands of space missions, improving the performance of QCL devices by addressing issues such as background doping and thermal management, and advancing the fabrication of QCL systems at terahertz frequencies.

Progress in the terahertz field also relies on exploring various power-locking schemes. It would be beneficial to focus on enhancing the techniques of photonic integrated circuits to achieve more reliable and fast power stabilisation. Additionally, efforts could be made to enhance the performance of TeraFET detectors. Researchers can also investigate the potential of using power and frequency control with RTR devices and TeraFETs. This combination of dual-locking techniques along with thermal and optical integration could be valuable applications in various industries such as healthcare, communication and space exploration. Furthermore, there is room for improvement in targeting gas emission lines by utilizing QCL grating techniques for enhanced frequency precision.

In addition to space missions like KEYSTONE, future research could explore the potential uses of terahertz technology in space research for remote sensing and the analysis of other astronomical objects. The study could also expand into terahertz gas spectroscopy for atmospheric chemistry and its impact on Earth's climate, examining the detection of additional gases and their consequences.

A key criterion for the use of THz QCL as local oscillators in space applications is that they are radiation tolerant. The total ionizing radiation dose (TID) is highly dependent upon the entire flight path of the satellite and is therefore mission-specific. For missions to study in the polar region of Earth, the radiation belts around such region have a relatively large cumulative dose due to the presence of auroras, which can hinder the QCL performance. The radiation roughness affects both the current density and gain of the QCL [3], [4]. The study shows the main mechanism by which the TID affects the operation of the QCL, is by electrons scattering into the lower energy sub-bands in the same well [3], [4]. However, proper study of QCL with

environmental testing including radiation roughness, and vibration resistance, presents significant challenges. Such studies typically require dedicated research projects focused on addressing these specific concerns and developing effective strategies to ensure the reliability and durability of QCLs under various environmental conditions.

6.3 KEYSTONE satellite roadmap

The KEYSTONE roadmap is on track, with substantial THz technologies achieved for realising the mission payload. Instruments including compact coolers and digital spectrometer systems have also evolved to meet the requirement of integrating on a compact satellite platform. Furthermore, the technical progress described in the thesis significantly contributes to the advancement of the THz mission roadmap. The integration of the complete front-end and back-end of the THz detection system represents a significant step forward for KEYSTONE and aligns with the roadmap trajectory.

Specific developmental areas include:

Breadboard integration and verification (6 months): Testing the QCL-LO within the KEYSTONE breadboard and characterizing optical integration. Furthermore, testing the thermal vacuum and assessing mechanical vibration tolerance, and measuring radiation roughness are necessary aspects.

QCL-LO optimization (6 months): Initially focusing on the development of proper growth and optimising the gain medium of the QCL based on improved active-region designs. Iterations in the QCL grating process are required to target LO frequency with greater precision.

Implementation, testing and integration of Schottky harmonic mixers (36 months): Integration of Schottky diodes mixer into machined waveguide QCL modules is required. Enabling the complete removal of the need for free-space optical coupling and enhancing system mass, volume, and robustness.

Testing of the frequency-lock electronic system (2 months): Enabling stable lock of the full LO system. Characterization of lock duration and stability for compatibility with a KEYSTONE observation cycle.

Integration with power and frequency-locking subsystem (24 months): Dual-loop stabilization facilitates simultaneous locking of power and frequency. A Schottky-diode mixer adjusts QCL bias current to lock emission frequency to a millimeter-wave oscillator, while the racetrack resonator system controls output power.

These combined efforts will help further the progress of terahertz technology and its application in space exploration, enabling innovative scientific investigations in this domain.

Bibliography

[1] L. Tombez, S. Schilt, J. D. Francesco, P. Thomann, and D. Hofstetter, 'Temperature dependence of the frequency noise in a mid-IR DFB quantum cascade laser from cryogenic to room temperature', Opt. Express, vol. 20, no. 7, pp. 6851–6859, Mar. 2012, doi: 10.1364/OE.20.006851.

[2] S. Barbieri et al., 'Heterodyne mixing of two far-infrared quantum cascade lasers by use of a point-contact Schottky diode', Opt. Lett., vol. 29, no. 14, pp. 1632–1634, Jul. 2004, doi: 10.1364/OL.29.001632.

[3] B. Knipfer, S. Xu, J. D. Kirch, D. Botez, and L. J. Mawst, 'Analysis of interface roughness in strained InGaAs/AlInAs quantum cascade laser structures ($\lambda \sim 4.6$ μm) by atom probe tomography', J. Cryst. Growth, vol. 583, p. 126531, Apr. 2022, doi: 10.1016/j.jcrysgro.2022.126531.

[4] J. Cheng et al., 'Dominant Influence of Interface Roughness Scattering on the Performance of GaN Terahertz Quantum Cascade Lasers', Nanoscale Res. Lett., vol. 14, no. 1, p. 206, Jun. 2019, doi: 10.1186/s11671-019-3043-6.

Appendix A

In standard fabrication of SI-SP QCL process, semiconductor wafer which contains quantum cascade laser active region is processed in multiple steps. These active regions were grown in Molecular Beam Epitaxy (MBE) lab at University of Leeds. The process of fabricating a single metal QCL have following four steps.

A.1 QCL Mesa etching process

As shown in Figure A.1, GaAs semiconductor was used, which would be the active region for the QCL prepared in MBE lab. Once the active region has been grown on the wafer, it needs to be processed and fabricated into a functional device. This is typically done in a cleanroom facility to avoid contamination of the wafer.

- Cleaning and Spin coating :-

It is possible for a wafer sample to appear clean but still be contaminated. To remove the contamination like dust particles, the sample was placed in a beaker filled with acetone and then in a beaker filled with isopropyl alcohol (IPA) for approximately 1 minute. When the sample is rinsed properly, N_2 gas was dry blown to dry the wafer. The sample was then placed on the spin coater where few drops of positive photoresist (S1813) was spread on the sample assuring that the photoresist does not stick at the back of the sample with a spinning rate of 5000 rpm for 30 seconds. This process makes the photoresist spread evenly. The sample was then placed on a hotplate at 115 ^{o}C for 1 minute to let the photoresist dry.

- Mask aligning for the edges and developing:-

By using the photo-lithography technique, the photoresist layer on the wafer is patterned and the exposed parts are afterwards removed. To remove the edge bead, the wafer is exposed to UV light through a mask aligner, which selectively exposes the

edge of the photoresist layer. After the exposure, the sample was placed in developer (MF319) for 3 minutes to remove the exposed portions of the photoresist. This was then rinsed with de-ionized (DI) water for 30 seconds and dried with dry blow of N_2 gas.

- Mask aligning for the ridges and developing :-

The sample was again carried for UV exposure in mask aligner where ridges where defined for the laser cavity. Sample was passed through the developing stage for 75 seconds, rinsed by DI water for 30 second and dried by blow of N_2 gas.

- Wet acid bench for etching :-

The etching solution was made by H_2O, H_2O_2 and H_2SO_4 with a proportion of 40:8:1 respectively. The proportion mixed to make etching solution is very important as it decides the etching rate (ideally it should be 1 micron per min). The etching solution was well stirred in a magnetic stirrer and left to cool for 45 minutes to 1 hour. The sample was mounted on a glass slide by the help of layer of photoresist and dipped in the etching solution. After the etching process, the mounted sample on glass slab by photoresist was removed, this was done by acetone and IPA.

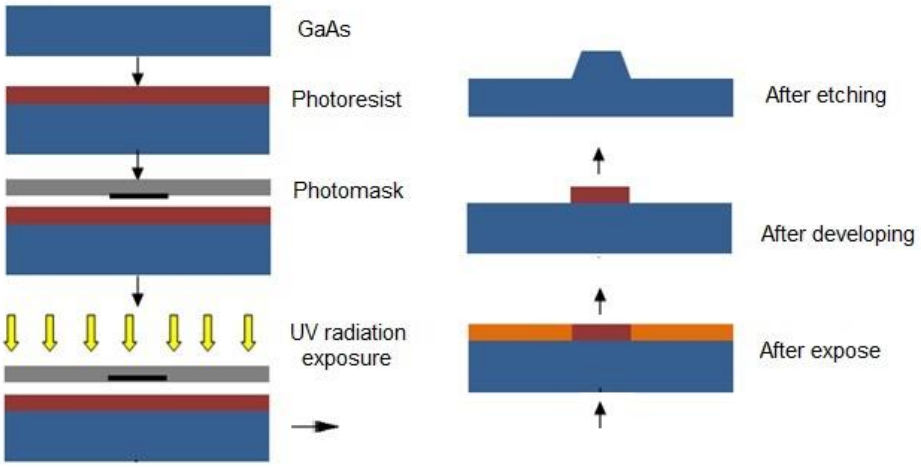

Figure A.1: Fabrication steps of etching QCL ridge

A.2 QCL bottom Ohmic contact

Figure A.2 shows the bottom Ohmic contact process. The etched sample again gone through the cleaning and the spin coating processes which are discussed previously.

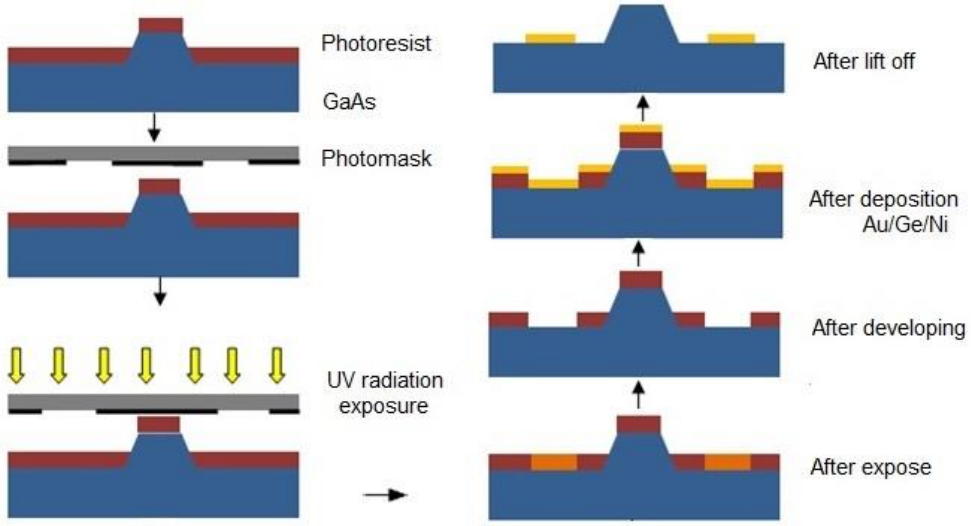

Figure A.2: Fabrication steps of bottom Ohmic contacts of QCL

After the spin coating process the sample was passed through the UV exposure by the mask aligner where the mask for bottom Ohmic contact was used, shown in Figure A.3. The sample with the exposer of UV radiation was placed in the chlorobenzene for 2 minutes. This process is to make the lift-off simpler. Chlorobenzene has a very pungent smell and can cause serious health problem if inhaled, so to avoid it, a beaker with lid was used to carry the process. Then, the sample was dried using N_2 gas. This dried sampled was then passed through the developing process, discussed earlier in section.

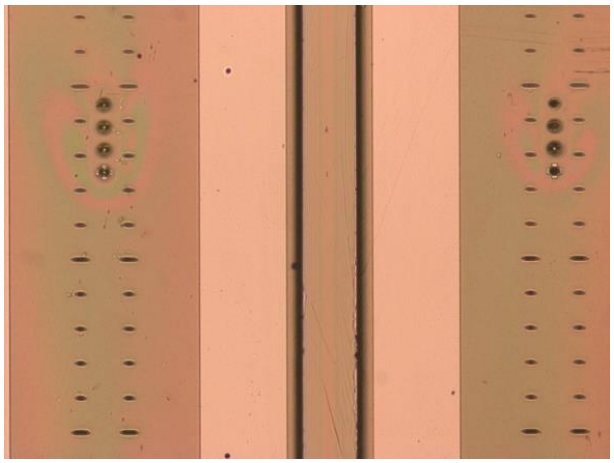

Figure A.3: Photoresist after bottom ohmic contacts

- O_2 plasma asher :-

For complete removal of photoresist and to enure good bonding, oxygen plasma asher is used. After developing process the sample was placed in the plasma ashing for 75 seconds at a power of 25 mW.

- Evaporation :-

The sample was then passed through the evaporator stage where, deposition of a layer of Au/Ge/Ni was carried out. The layer thickness was noted approximately to 200 - 250 nm. The mass of the Au/Ge/Ni should be around 0.5 – 0.6 grams. The sample was then left for 6 hours in acetone for initial lift-off process, shown in Figure A.4. Still some unwanted metal was deposited on the sample which was lifted - off by placing the sample in the acetone and gently agitating on top of it with a brush. Sample was the rinsed again by acetone and IPA and dried with N_2 gas.

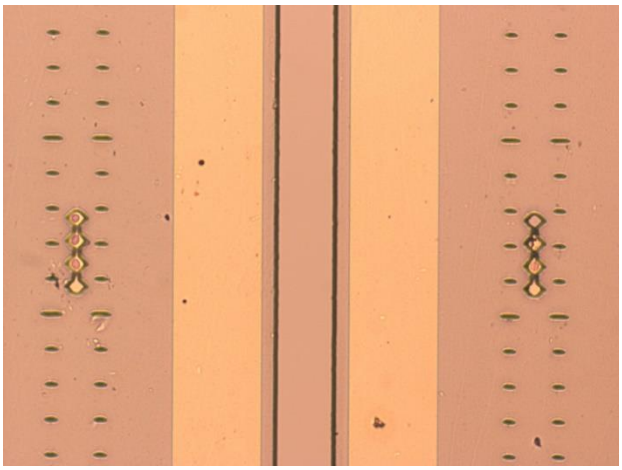

Figure A.4: Bottom Ohmic contacts metallisation

- Annealer (RTA) AS-One :-

The Rapid Thermal Annealer (RTA) is a commonly used in the annealing process. The RTA is like a furnace that can rapidly heat and cool a sample to a certain temperature in this case for 1 minute at 430 ^{o}C. Annealing is done to boost up the free electrons in lower n- GaAs layer, shown in Figure A.5. This modifies the properties of the material, such as its electrical conductivity.

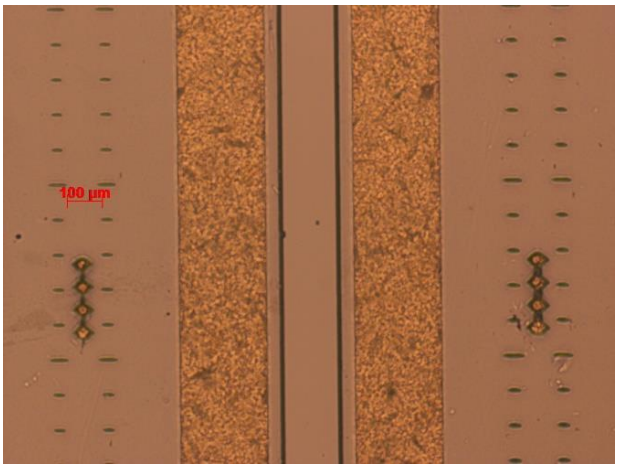

Figure A.5: Annealing after Bottom Ohmic contacts

A.3 QCL Top Ohmic contact

The top Ohmic contact is the electrical contact that is made to the uppermost layer of the sample. Narrow strips of Au/Ge/Ni are used for the top Ohmic contact. These are necessary as it avoids the partial mixing of top contact with the active region and thus, losses can be prevented. The fabrication of the top Ohmic contact was same as the bottom Ohmic contact which is discussed earlier in section, except, the mask used in the top Ohmic contact was different and while performing the evaporation process, the thickness of the Au/Ge/Ni layer was around 100 nm.

As from Figure A.6, the narrow strips fabricated on the top prevents from damaging the n-GaAs layer with impurities. The sample was then passed through the RTA machine for 3 minutes at 270 ^{o}C.

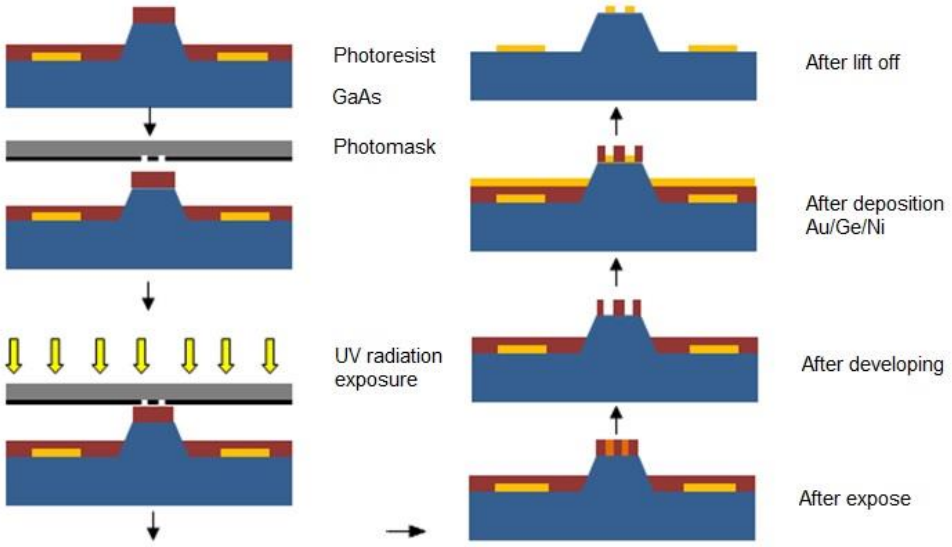

Figure A.6: Fabrication steps of top Ohmic contacts of QCL

A.4 QCL Over-Layer metallisation

The procedure of over-layer metallisation is similar to that of the bottom Ohmic contact, shown in Figure A.7. The only difference was the mask used for the over-

layer metallisation and the deposition layer was of Ti instead of Au/Ge/Ni, which have a thickness of around 20 nm, illustrated in Figure A.8. For the proper confinement of the modes between lower and upper layer, over-layer metallisation is used.

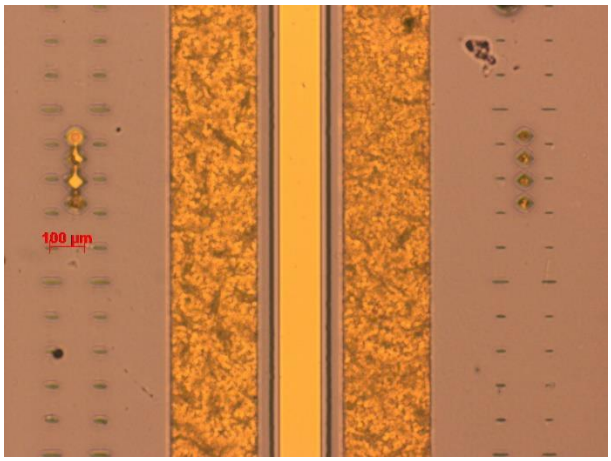

Figure A.7: Over-layer metallisation

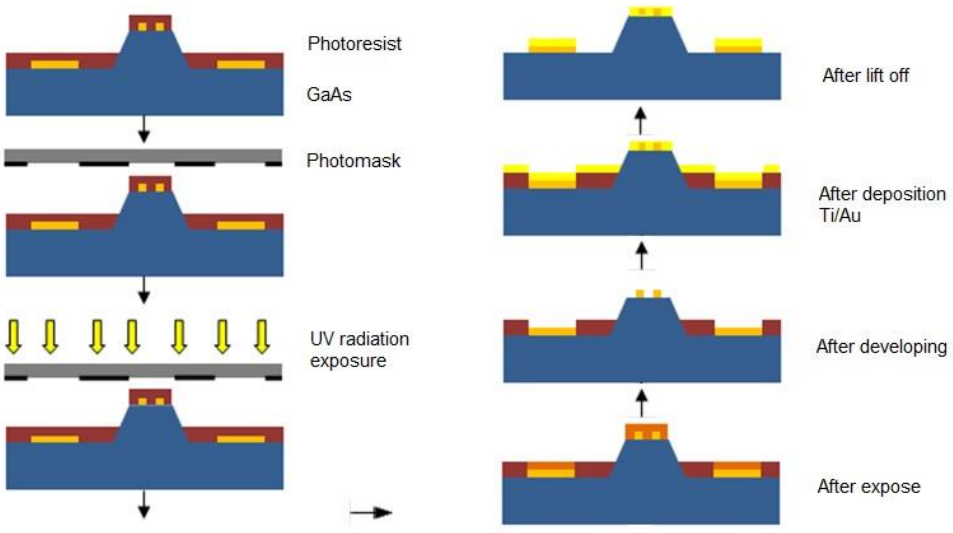

Figure A.8: Fabrication steps of over-layer metallisation of QCL

A.5 Substrate thinning and backside metallisation

The substrate thinning is a key part of QCL fabrication as thinning of substrate improves the heat dissipation. This process should be done before the backside metallisation. In the process of substrate thinning, the sample was mounted on the glass slab by the help of wax.

Firstly, the wax was melted while placing it on hotplate at 60 ^{o}C. Then sample was placed upside down on the glass slab. The sample's backside was positioned facing upward during the thinning process, ensuring that the upper part of the sample was in complete contact with wax. The height was measured as 605 µm. An etching solution was made using H_2O:H_2O_2:H_2SO_4 in 1:8:1 ratio. The solution was stirred and allowed to cool. The sample was dipped in the solution and stirred, the rate of etching was around 20 micron per minute. After substrate thinning, measurements of the sample thickness was carried out. This thickness was found to be the optimum thickness for heat extraction (in this case ~200 µm). Then the wax was removed from the glass slab by placing the glass slab in Trichloroethylene (TCE) for 30 minutes and then rinsed by IPA and dried using N_2 gas. The sample was then passed through the evaporation process where Ti/Au layer of 20-100 nm was deposited at the back of the sample. After the backside metallization, the sample is typically annealed for 3 minutes at 270 ^{o}C to improve the quality and electrical properties of the metal-semiconductor interface.

A.6 Sample cleaving

Sample cleaving is a critical process in QCL fabrication, as it is necessary to separate the individual devices from the larger sample without damaging them. Wafer scriber – S100 was used to separate the ridges. These ridges provide a pre-determined line of weakness, allowing the sample to be broken cleanly along those lines. The sample had three ridges, cleaving the sample gave six QCL out of which the best two were selected for characterization.

A.7 Soldering QCL on the copper block and wire bonding

To mount a QCL on copper block, ceramic pads were attached to the copper block on which indium was melted at 150 ^{o}C using a hotplate. The QCL was placed on the melted indium and then the temperature of the hotplate was reduced to 130 ^{o}C. Alignment of the QCL was done with three manipulators to keep the QCL and the ceramic pads stable. The temperature of the hotplate was gradually increased to get a flat layer of indium and then soon decreased to cool it down.

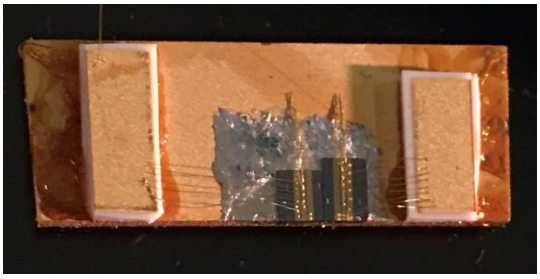

Figure A.9: Top view of copper block after mounting and wire bonding of two QCLs

As shown in Figure A.9, the mounted QCL with the ceramic pads were wire bonded by ball bonder with several gold wires connecting the top and the bottom contacts of the sample to the ceramic pads.

B.1 Terahertz quantum cascade laser devices used in the thesis

This table outlines the QCL devices used in each chapter of the thesis for easy reference and understanding.

Table B.1: Different QCL devices used in thesis

Device name	THz QCL devices	Chapters
Device A	5 THz QCL	Chapter 2
Device B	3 THz QCL	Chapter 2
Device C	3.5 THz RTR - QCL	Chapter 3
Device D	Integrated 3.5 THz RTR – QCL	Chapter 4
Device E	Integrated 4.7 THz QCL	Chapter 4
Device F	Integrated 2.0 THz QCL	Chapter 4
Device G	3.4 THz QCL	Chapter 5